Alma Mater Studiorum – Università di Bologna

DOTTORATO DI RICERCA IN

CHIMICA

Ciclo 33

Settore Concorsuale: 03/B1 - FONDAMENTI DELLE SCIENZE CHIMICHE E SISTEMI INORGANICI

Settore Scientifico Disciplinare: CHIM/03 - CHIMICA GENERALE E INORGANICA

PHOTOCHEMICAL PROCESSES IN MOLECULES AND SEMICONDUCTOR NANOCOMPOSITES: PHOTOACID/PHOTOBASE GENERATORS AND TIO_2/GRAPHENE PHOTOCATALYSTS

Presentata da: Arianna Menichetti

Coordinatore Dottorato

Domenica Tonelli

Supervisore

Marco Montalti

Co-supervisore

Fabrizia Grepioni

Esame finale anno 2021

Abstract

In the last years, the use of light as a reagent has launched a huge variety of new reaction pathways and has consequently led to the development of many new applications. Indeed, photochemical reactions involve excited state species that, having different properties with respect to the ground state, lead to different reactivity. During my PhD, I worked on photochemical reactions. I studied photochemical processes in molecules and in semiconductors, working respectively with photoinitiators such as photoacid and photobase generators and with photocatalysis of semiconductors, such as TiO_2.

In the first part of this work, photoacid and photobase generators have been treated with the aim of controlling and localizing pH variations with light. This potentiality was exploited to obtain controlled precipitation and dissolution of calcium carbonate, which can lead to many new applications. We first focused on the development of a photoprecipitation/photodissolution method for application as a new technique for artwork restoration. Diphenyliodonium hexafluorophosphate was used as a photoacid generator to provoke the dissolution of calcium carbonate. Precise and controlled dissolution of $CaCO_3$ could be achieved using a focused LED at 365 nm. Moreover, the use of Thioxanthone as sensitizer led to a very fast dissolution with irradiation even at 395 nm, thus making the process more efficient and less harmful for the future application. Photoinduced precipitation of calcium carbonate was obtained in solution by using two photobase generators, Sodium tetraphenylborate and Ketoprofen, exploiting the large pH jump of the former and the pH increase coupled with CO_2 generation in the latter. Also in this case, the use of Thioxanthone as a sensitizer boosted the performances of Sodium Tetraphenylborate using a Near-UV light source. Photoinduced crystallization of $CaCO_3$ by Ketoprofen was also implemented in a gel matrix to fix $CaCO_3$ crystals generated by the light stimulus. The possibility to embed $CaCO_3$ crystals in a support will allow to write $CaCO_3$ structures by light with high precision and apply this process to lithography and patterning systems.

In the second part of this work photocatalytic behaviour of TiO_2 in environmental remediation has been described. TiO_2 colloidal nanoparticles were synthesized with an easy method and using different kind of surfactants. Very stable and transparent aqueous dispersions of small (5-7 nm) TiO_2 nanoparticles were obtained, useful for water decontamination. Photocatalytic properties were investigated for water remediation by organic pollutants, using Rhodamine B as a model; a great enhancement of photocatalytic performances has been achieved with respect to commercial TiO_2 aqueous dispersions. Moreover, TiO_2 colloidal nanoparticles are also resistant to several irradiation cycles and thus suitable for a real application. We also modified TiO_2 colloidal nanoparticles with Graphene and MoS_2, obtaining, in some cases, a further enhancement in the

photocatalytic activity, depending on the surfactant used for the nanoparticle synthesis. TiO_2 nanoparticles stabilized by Pluronic F-127 were also modified with polydopamine (PDA). This led to an interesting system in which TiO_2-PDA can be dried and re-dissolved in water without losing their nanoparticle nature. This also led to a stabilization of the nanoparticles at different pH values. Thus, it was also possible to study photocatalytic activity in different pH conditions.

Finally, TiO_2 photocatalytic coatings modified by Graphene were studied for air remediation, after embedment in a cement matrix. In particular, inorganic pollutants decontamination was investigated by using NOx gases as models. Once verified the photocatalytic activity of the new composite, we focused on the aging effects. We evaluated performances with 30 and 60 cycles of irradiation by a solar simulator lamp and with continuous refreshing of the pollutant gases. The photocatalytic activity remained high and stable during all the cycles of irradiation, showing a great resistance that made it suitable for the real application in self-cleaning cementitious surfaces.

Contents

1. Introduction: Photochemical reactions in molecules and semiconductor nanomaterials

1.1. From first empirical evidence to photochemistry principles

Photochemistry is the branch of science that explores light-matter interaction, which has always had a relevant role in many natural processes. The most studied photochemical transformation is surely photosynthesis, but many other examples can be mentioned such as bioluminescent organisms or the visual system of the eye. Despite the presence of many photochemical phenomena in nature, scientists started to observe and be interested in them mainly in the XVIII century. The very first case of observation of a photochemical reaction was in 1565 in which the alchemists observed the darkening of silver chloride, called "horny moon", under the action of sunlight[1]. Nevertheless, only in 1727 the scientist Schultze attributed to the action of light – and not to the sun's heat as previously believed - the darkening of silver salts[2, 3]. The Swedish chemist Scheele, by means of the investigation on Bestuzhev and Schultze discoveries, in 1777 proved that there was a difference in the darkening on silver salts depending on the wavelength of the light: violet rays of the solar spectrum had a more rapid effect with respect to the other rays[3]. In the XIX century, the further development of these studies built the basis of photography (Figure 1).

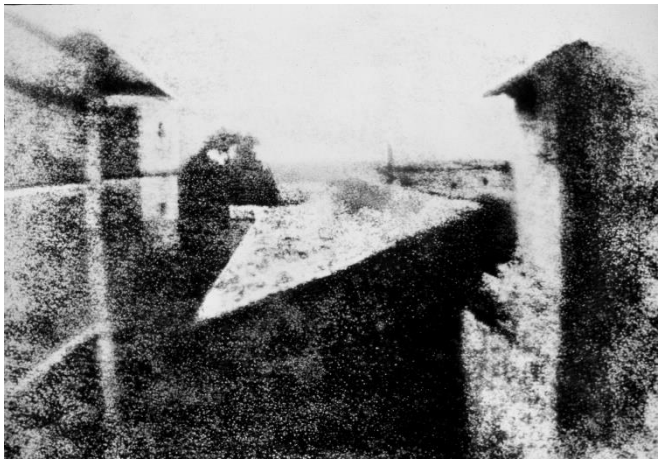

Figure 1: First photography, "Point de vue du Gras", by Joseph Nicéphore Niépce[4]

However, at that time, the observation of such photochemical phenomena was basically empirical, a real conceptualization of light and its interactions with matter was still lacking. Grotthuss in 1817 and Draper in 1841 established the first general principle of photochemistry for which "only the light absorbed can produce a photochemical effect", but only after one century it would have been possible to understand the interaction between the wavelength of the light absorbed by a species and its molecular structure[5]. Photochemical events started to be more deeply explored at the beginning of the XX century. Giacomo Ciamician is one of the scientists considered a pioneer of photochemistry[6]. He had a great impact in the scientific community thanks to his studies on the use of light in the chemical synthesis in plants and on how similar mechanisms could be exploited to obtain solar energy conversion[7]. Moreover, progress in modern physics allowed to give a theoretical explanation of photochemistry. In particular, during the XVII century, the nature of light was described by two main theories: the "corpuscular theory" with which Newton conceived light as an ensemble of very small particles[8], and the "wave theory", in which Huygens defined light as a wave which could propagate in a medium[9]. This theory was clarified in 1860 by Maxwell, which included light waves as part of the spectrum of electromagnetic waves[10]. In this vision, light had the same properties as an electromagnetic wave: a wavelength (λ) inversely proportional to a frequency (ν) by means of a constant speed (c= 2.998 x 10^8 m s^{-1} in vacuum) (Eq.1).

$$\lambda\nu = c \qquad \text{Eq.1}$$

The corpuscular model was developed in 1900 by Planck that described the energetic exchange between matter and electromagnetic field. He postulated that electromagnetic radiation interacted with matter only by means of discrete quantities of energy, "quanta" (called then "photons" in 1926 by Lewis)[11]. According to his theory, each photon has a specific energy (E), which is correlated to the frequency of the electromagnetic field (ν), as described in the Planck's Law (Eq.2).

$$E = h\nu \qquad \text{Eq.2}$$

The Energy and the frequency of the photon are correlated by means of the Planck constant h= 6.63 x 10^{-34} J s. In 1905, Einstein by the interpretation of the photoelectric effect, gave experimental evidence of the corpuscular nature of light[12]. At this point, light was described both as a wave and a particle (wave-particle dualism). This contrast was then strengthened by De Broglie (1925)[13] that introduced the particle-wave dualism, hypothesizing that particle beams

could also behave as waves. Since the first decades of the XX century, these principles have made possible the development of photochemistry and still today they represent the basis of this field. All the studies on nature of light described above allow nowadays the interpretation of any process in which light is involved. Indeed, the first event that characterize any photochemical process is the absorption of a photon (Eq.3).

$$A + h\nu \rightarrow A^* \qquad \text{Eq.3}$$

Equation 3 represents the light absorption process, in which A represents the species at the ground state, $h\nu$ a photon of the appropriate energy to be absorbed by A and A^* the species in an electronically excited state. As molecular orbitals theory explains[14], each electronic configuration of a molecule corresponds to one or more electronic states at different energies and the electronic configuration that characterizes one molecule at room temperature is always the one that corresponds to the electronic state at the lowest energy, called "ground state" (A). The absorption of light of a certain wavelength (UV-Vis range) leads to a change in its electronic configuration, thus the molecule is not in the ground state anymore, but it is in an "excited state" (A^*). The energy and the distribution of the electrons in a molecule determine its properties such as bond length, spatial structure, charge distribution, electron affinity, ionization potential but also the interaction with other molecules and the solvent[15]. Therefore, the change in the electronic configuration leads to a change in all the properties of the molecule and thus the molecule in the excited state must be considered a totally new species, with characteristics that could significatively differ from the molecule at the ground state. Once the excited state is generated, the A^* species can undergo photophysical or photochemical processes (Scheme 1.).

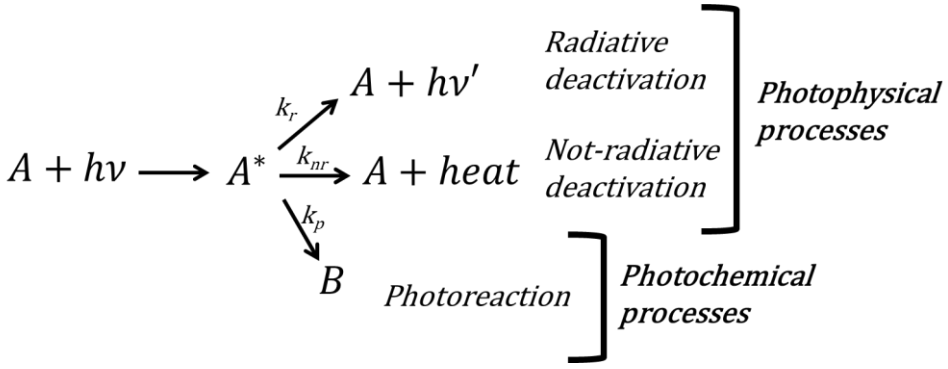

Scheme 1: processes undergone by a molecule after the absorption of light. Each process is characterized by a kinetic constant (k_r for radiative processes, k_{nr} for not-radiative processes and k_p for photochemical reactions)

In particular, the excited molecule can return to the ground state and release energy by emitting light (radiative deactivation) or by producing heat (not-radiative deactivation). This kind of phenomena are called photophysical processes. Otherwise, the excited state can react and transform into another molecule (B) undergoing a photochemical process. Once the excited state is generated, these events always compete and the molecule usually undergo the faster pathway. Each process is described by a kinetic constant named respectively k_r, k_{nr} and k_p for radiative deactivation, not-radiative deactivation, and photoreaction. So far, among photochemists, the photophysics of a molecule is always represented by the Jablonski Diagram (Figure.2), introduced by Alexander Jablonski in 1933[16] and then completed by Lewis and Kasha in 1944[17, 18].

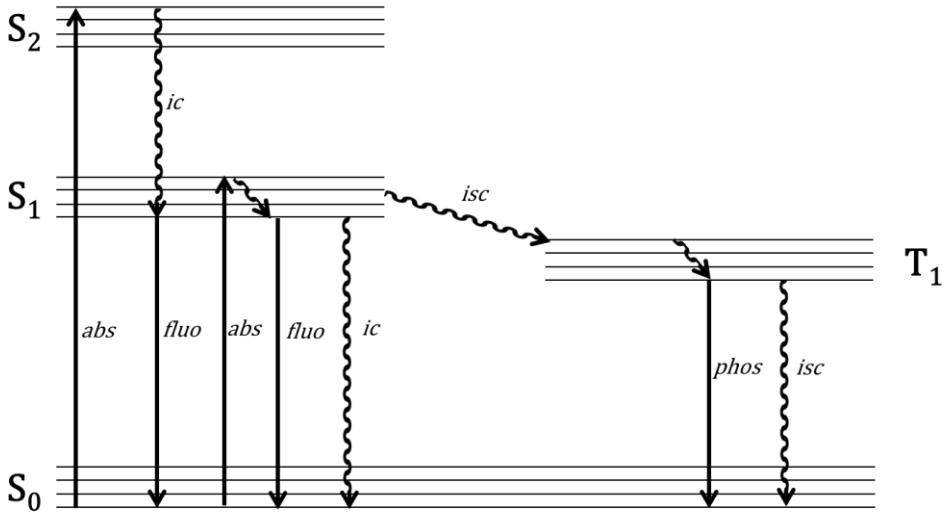

Figure.2: example of Jablonski Diagram

The Jablonski diagram shows the electronic states of a molecule (S_0, S_1...) and in this representation, each electronic state is displayed with its vibrational energy levels. The radiative and not-radiative processes are depicted respectively with straight and wavy arrows. The electronic states involved in photophysical and photochemical processes are usually singlet and triplet states, depending on the spin multiplicities of a certain electronic configuration. According to spin selection rules[19-21], an electronic transition is allowed if it occurs between two states with the same spin multiplicity. As an example, a transition from a singlet state to a single state is spin-allowed, while a transition from a singlet state to a triplet state is spin-forbidden. Not-radiative electronic transitions are divided in internal conversion (ic) or intersystem crossing (isc) that correspond respectively to spin-allowed and spin-forbidden events. The radiative processes are fluorescence (fluo) and phosphorescence (phos): fluorescence occurs when the electronic transition is spin-allowed while phosphorescence when it is spin-forbidden. Thus, internal

conversion (10^{-12}-10^{-6} s) and fluorescence (10^{-9}-10^{-7} s) are always favoured and faster with respect to intersystem crossing (10^{-12}-10^{1} s) and phosphorescence (10^{-6}-10^{-3} s). Not-radiative processes occur also between vibrational levels in the same electronic state and are called vibrational relaxations; they are usually faster than any deactivation process between electronic states (10^{-13}-10^{-12} s)[22].

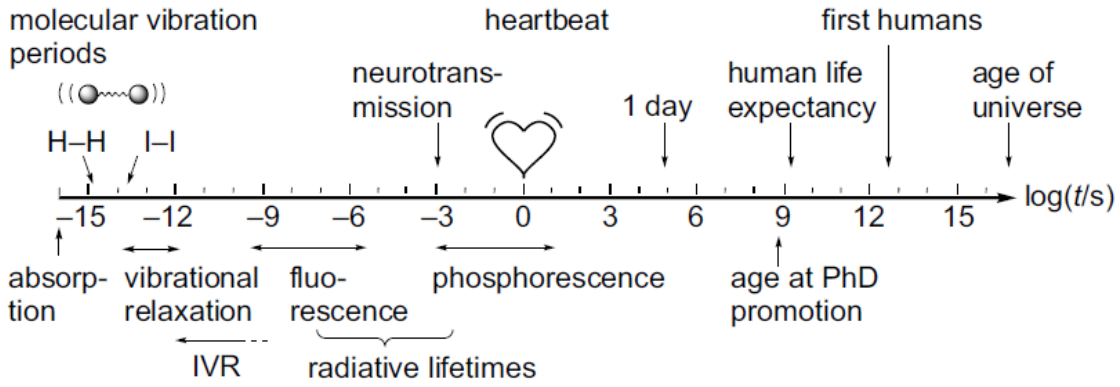

Figure 3: Time scales, reproduced from [22]

If the molecule is in an excited state higher than the first (S_2 in Figure 2) it usually deactivates not-radiatively to S_1 or T_1. Consequently, all the radiative processes start from the first electronic excited state (Kasha's rule[23]). As already mentioned, the pathway that the excited molecule will take depends on the rates of the different photophysical and photochemical processes. Thus, each path has a certain probability which could depend on the intrinsic properties of the molecule and/or the surrounding environment. The main parameters that define photophysical/photochemical events are the lifetime of the excited state (τ), the efficiency (η) and the quantum yield (Φ). The lifetime is the amount of time for which an excited state lives and it depends on how fast the deactivation processes are. Indeed, it is inversely proportional to the sum of the kinetic constants of all the deactivation pathways (Eq.4).

$$\tau = \frac{1}{\Sigma k} \qquad \text{Eq.4}$$

Usually, the lifetime of a fluorescent species is few nanoseconds, while the lifetime of a phosphorescent species is significatively slower, in the order of microseconds. The efficiency of a process is defined as the ratio between the kinetic constant of the process and the sum of all the kinetic constants (Eq.5). It reflects how much a deactivation pathway is favoured with respect to the others.

$$\eta_i = \frac{k_i}{\Sigma k} \qquad \text{Eq.5}$$

Finally, the quantum yield of a process is defined as the ratio between the number of molecules that undergo that process in time ($^{dn(X)}/_{dt}$) and the number of absorbed photons in time (photon flux - $q_{p,as}$)[11].

$$\Phi = \frac{^{dn(X)}/_{dt}}{q_{p,as}} \qquad \text{Eq.6}$$

The event in which, after the absorption of a photon, the excited molecule is just deactivated by a chemical transformation or by returning to the ground state, is called "primary process". That can be the case of a fluorescence from the first excited state S_1. If the excited molecule is first converted in another excited state or an instable species, there will be other events that follow the primary process, called "secondary processes". In a primary process, the quantum yield will coincide with the efficiency, while in a secondary process, it will be the product of the efficiency of all the events[11].

Primary process (i.e. fluorescence) $\Phi_{fluo} = \frac{k_{fluo}}{k_{fluo} + k_{ic} + k_{isc}} = \eta_{fluo}$ Eq.7

Secondary process (i.e. phosphorescence) $\Phi_{phos} = \frac{k_{isc}}{k_{fluo}+k_{ic}+k_{isc}} \cdot \frac{k_{phos}}{k_{phos}+k_{isc}} = \eta_{isc} \cdot \eta_{phos}$ Eq.8

1.2. Photochemistry of molecules

Photophysical pathways, described by the Jablonski Diagram (Figure 2), are fundamental processes that characterize the excited state of a molecule and do not lead to a chemical modification of the original molecule. On the other hand, an excited species can undergo photochemical reactions and modify or not (i.e. photoisomerization) its chemical composition[15]. As mentioned before, the excited state must be considered as a new chemical species with its own properties and reactivity. Furthermore, a photochemical reaction is intrinsically different from a thermal reaction because the excited species are very reactive, thus the reaction occurs with low

or no activation energy and in very high rates, having also to compete with the other deactivation pathways[15].

First, it is important to divide the processes that an excited state can undergo in two main categories. Until now, all the mentioned photophysical and photochemical events involve only the behaviour of the excited molecule and are called "unimolecular processes". However, the excited species (A^*) could interact with another molecule present in the surroundings (B); this kind of events are called "bimolecular processes". Since the reaction undergone by the molecule B is not given by its direct excitation but by the interaction with another excited species, the molecule A is usually called the "sensitizer" of B. Intermolecular interactions of molecules in the excited states in solution are very common and the encounters of the reactant molecules, forming the "encounter complex", are governed by diffusion (Scheme 2).

$$A^* + B \underset{k_{-d}}{\overset{k_d}{\rightleftharpoons}} A^*.B \xrightarrow{k_p} P$$

Encounter complex

Scheme 2: reaction between molecules A and B via the formation of an encounter complex

In scheme x k_d represents the bimolecular rate constant of diffusion, k_{-d} the first-order rate constant for escape from the encounter complex and k_p the first-order rate constant of the product formation in the encounter complex[22]. If we consider that the concentration of the encounter complex ($c_{A^*.B}$) is constant during the whole process (steady-state approximation), we can assume that the rate of product formation depends on the diffusional constant k_d, the reactants concentrations ($c_{A^*} and\ c_B$) and the efficiency of the product formation from the encounter complex[22] (η_p) as showed in Eq. 9,10,11:

$$dc_{A^*.B}/_{dt} = k_d c_{A^*} c_B - \left(k_{-d} + k_p\right) c_{A^*.B} \approx 0 \quad \textit{Steady state approximation} \qquad \text{Eq.9}$$

$$dc_p/_{dt} = k_p c_{A^*.B} \qquad \text{Eq.10}$$

$$dc_p/_{dt} \approx k_d c_{A^*} c_B \frac{k_p}{k_{-d} + k_p} \approx k_d c_{A^*} c_B \eta_p \qquad \text{Eq.11}$$

According to this approximation, when $k_{-d} << k_p$ the process will be "diffusion-controlled" while when $k_{-d} >> k_p$ the process will be "reaction-controlled".

If an excited molecule A^* in solution can interact with another species B, all the possible deactivation pathways of the excited state are in competition also with this new event. This effect

in evident in the fluorescence intensity decrease of the excited species; for this reason, an excited state involved in a bimolecular process is usually "quenched" by the other species. We can thus express the excited state deactivation including the bimolecular process (in which k_q is the quenching kinetic constant), represented by a second order kinetic law (Eq 12) and derive the corresponding lifetime (Eq.13).

$$-{}^{d[A^*]}/_{dt} = (k_r + k_{nr} + k_p + k_q[B])[A^*] \quad \text{Eq.12}$$

$$\tau = \frac{1}{k_r + k_{nr} + k_p + k_q[B]} \quad \text{Eq.13}$$

At this point, we can compare the lifetime in absence (τ_0) and in presence of the "quencher" B (τ) and express their ratio (Eq.14)

$$\frac{\tau_0}{\tau} = 1 + \tau_0 k_q[B] \quad \text{Eq.14}$$

The equation that results (Eq.14) is known as Stern-Volmer equation, in which the term $k_q[B]$ is the Stern-Volmer constant (k_{SV})[24]. This linear equation is very important because allows to calculate the quenching kinetic constant by plotting the ratio of the lifetimes as a function of the quencher concentration.

One of the most common examples of a bimolecular process is Energy transfer, in which the excitation energy of an excited molecule A^* (donor) is transferred to a molecule B (acceptor) (Scheme 3).

$$A^* + B \longrightarrow A + B^*$$

Scheme 3: Energy transfer process

Two types of energy transfer processes can be distinguished: radiative (or trivial) energy transfer and not-radiative energy transfer (Scheme 4):

Radiative (or trivial) energy transfer

$$A^* \longrightarrow A + h\nu$$
$$A + h\nu \longrightarrow B^*$$

Not-radiative energy transfer

$$A^* + B \longrightarrow A^*.B$$
$$A^*.B \xrightarrow{k_{En.T}} A\,.\,B^*$$
$$A\,.\,B^* \longrightarrow A + B^*$$

Scheme 4: Radiative and not-radiative energy transfer

In radiative energy transfer, the molecule B is excited, not by a real sensitization, but by the fluorescence of A. The only requirement of this process to happen is an overlap between the fluorescence spectrum of A and the absorption spectrum of B. However, the most common energy transfer process is the not-radiative one, in which there is a radiationless transition in the encounter complex $A^*.B$. The occurrence and the rate ($k_{En.T}$) of this kind of process have a dependence on the distance between the two molecules involved and are of two types: Förster resonance energy transfer[25] or Dexter (or exchange) energy transfer[26]. Further details on energy transfer mechanism can be found in reference[27]. One of the most important example of energy transfer process is represented by antenna systems in natural photosynthesis. The function of these antenna pigments (among which chlorophyll is the most common) is to gather sunlight and concentrate it to the reaction centre where it is converted into chemical energy; this happens by means of several energy transfer processes (Figure 4)[28].

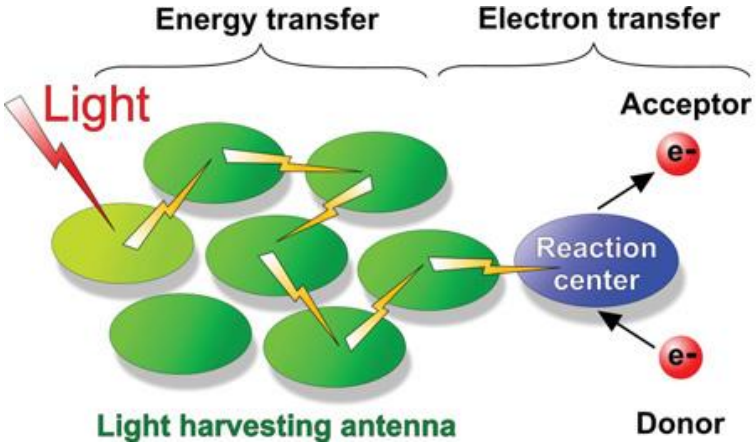

Figure 4: antenna system in photosynthesis: energy transfer processes between pigments deliver the excited state to the reaction center in which electron transfer processes take place. Reproduced from ref[29].

Another very common bimolecular process is Electron Transfer, in which a redox process occurs between the excited molecule and the one in the ground state (Scheme 5):

$$A^* + B \longrightarrow A^*.B$$

Electron transfer (eT)

$$A^*.B \xrightarrow{k_{eT}} A^+.B^- \qquad A^*.B \xrightarrow{k_{eT}} A^-.B^+$$

$$A^+.B^- \longrightarrow A^+ + B^- \qquad A^-.B^+ \longrightarrow A^- + B^+$$

Scheme 5: photoinduced electron transfer processes

Even if two molecules at the ground state would not interact by a redox process, they can have a photoinduced electron transfer. That is because a molecule in the excited state has a lower ionization potential and a higher electronic affinity, resulting in being both a better reductant and a better oxidant than the molecule in the ground state. When a photoinduced electron transfer occurs, a radical-ion pair is first formed, whose energy has to be lower than the one of the excited donor or acceptor[30]. Then two main processes compete: the radical-ion pair can be separated in free radicals or be recombined to regenerate the species at the ground state (back-electron transfer), as is displayed in Scheme 6.

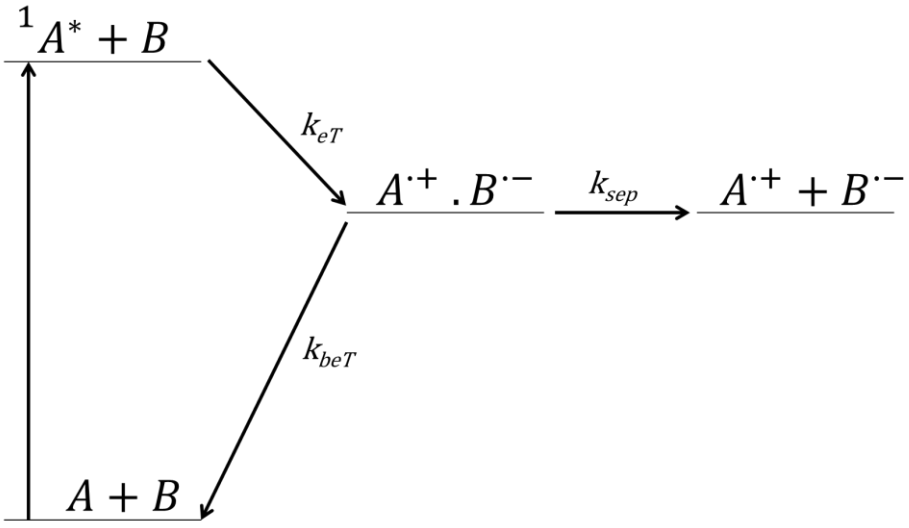

Scheme 6: energy diagram of photoinduced electron transfer[30]. k_{eT}, k_{bet} and k_{sep} are the kinetic constants respectively for electron transfer, back electron transfer and separation of radical ions.

Therefore, the yield of the separation between the photogenerated radical-ion pairs depends also on the rate of the back-electron transfer process. Other processes that can also occur after the

formation of the radical-ion pair are proton transfer or other rearrangements like atom, group transfer or bond formation[31]. Generally, the fate of the radical-ion pair depends on factors like solvent polarity or magnetic field[32, 33]. An interesting example of these kind of processes is represented by proton-coupled electron transfer reactions (PCET), cases in which electron transfer is accompanied by a proton transfer, as it happens in the reduction of $^3C_{60}$ by phenols, in presence of a base(Scheme 7)[34].

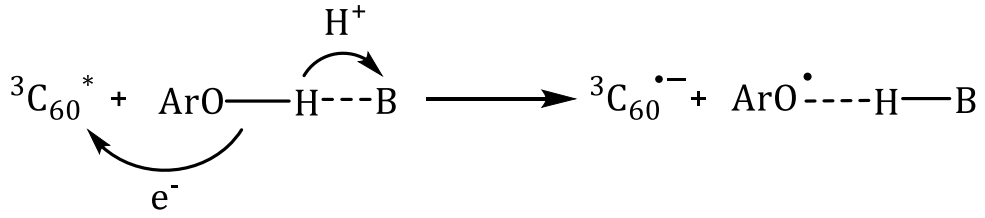

Scheme 7: PCET in the reduction of $^3C_{60}$ by phenols, in presence of a base[34]

This process is an example of a solvent polarity dependent reaction (hydrogen bond is involved) and of an electron transfer favoured by the occurrence of a proton transfer[35]. Coupling of electron and proton transfer mechanisms also rule in reaction centres of photosynthetic organisms[29].

Among the processes that involve excited states, photochemistry of organic molecules is one of the most important classes of photochemical reactions, because it opens to more accessible organic synthesis paths[36]. Indeed, several photochemical pathways are possible for every class of organic molecules. Some examples will be briefly described in the next paragraphs referring to a relevant book in the field: "Photochemistry of organic compounds: from concept to practice"[37].

One of the main photoreactions of alkenes surely are E-Z (or trans-cis) photoisomerizations (Scheme 8).

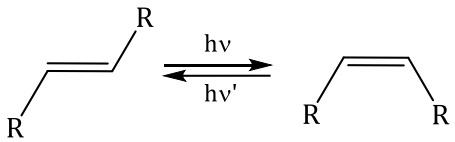

Scheme 8: E-Z (trans-cis) photoisomerization

The 180°C rotation around the C=C bond can be both a thermal and a photochemical reaction. When the thermal reaction occurs a mixture of isomer is produced that depends on the thermodynamic stability of the two isomers (trans is usually the most thermodynamically stable).

When the reaction occurs photochemically the cis→trans and the trans→cis isomerizations are governed by irradiation with the two proper wavelengths (hν and hν' in Figure 8). When the rates of formation of the two isomers are equal, a photostationary state is achieved and the mixture will depend on isomerization quantum yields and extinction molar coefficients of the two isomers. Photoisomerization reaction is very important in nature, since is the main process behind the mechanism of vision[38]. Other processes that involve excited alkenes are eletrocyclic and sigmatropic rearrangements and proton addition or oxidation/reduction (Scheme 9).

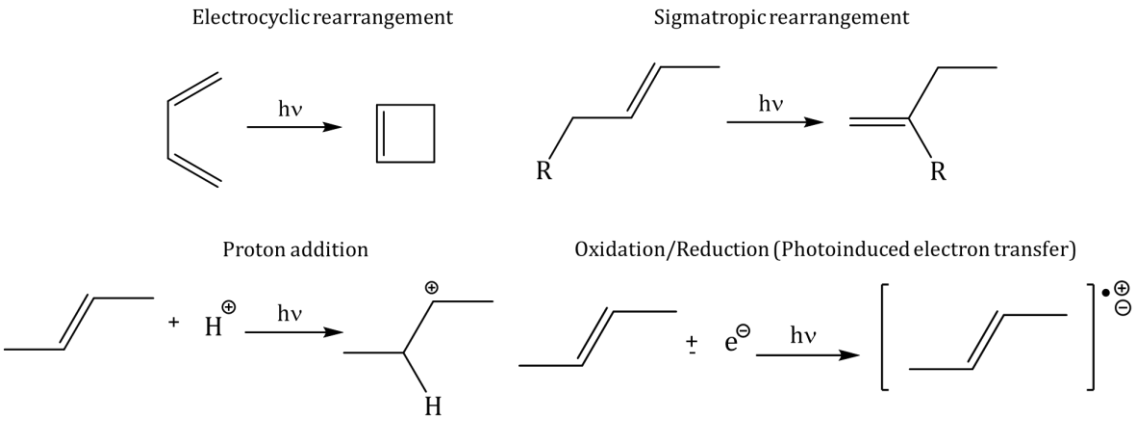

Scheme 9: Other common photoinduced processes of alkenes

Photochemical reactions that involve aromatic compounds are of high interest because of the intrinsic thermodynamic stability of aromatic species in the ground state; thus their light excitation leads to reaction pathways otherwise unexplored. As an example, substituted aromatic compounds, which at the ground state give only electrophilic substitutions, at the excited state give nucleophilic substitution (Scheme 10).

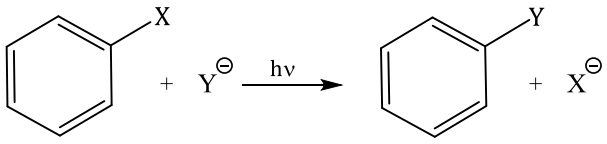

Scheme 10: nucleophilic substitution of aromatic compounds.

This happens because the HOMO of the aromatic structure, which is nucleophile at the ground state, become a half-filled electrophile HOMO (while the half-filled LUMO has a nucleophilic character) at the electronically excited state. There are many mechanisms for photoinduced nucleophile substitution (Scheme 11) such as unimolecular substitution(S_N1Ar^*), nucleophilic

attack(S_N2Ar^*), C-X homolysis and photoinduced electron transfer (PET) to or from (not shown in the figure) the aromatic moiety[15].

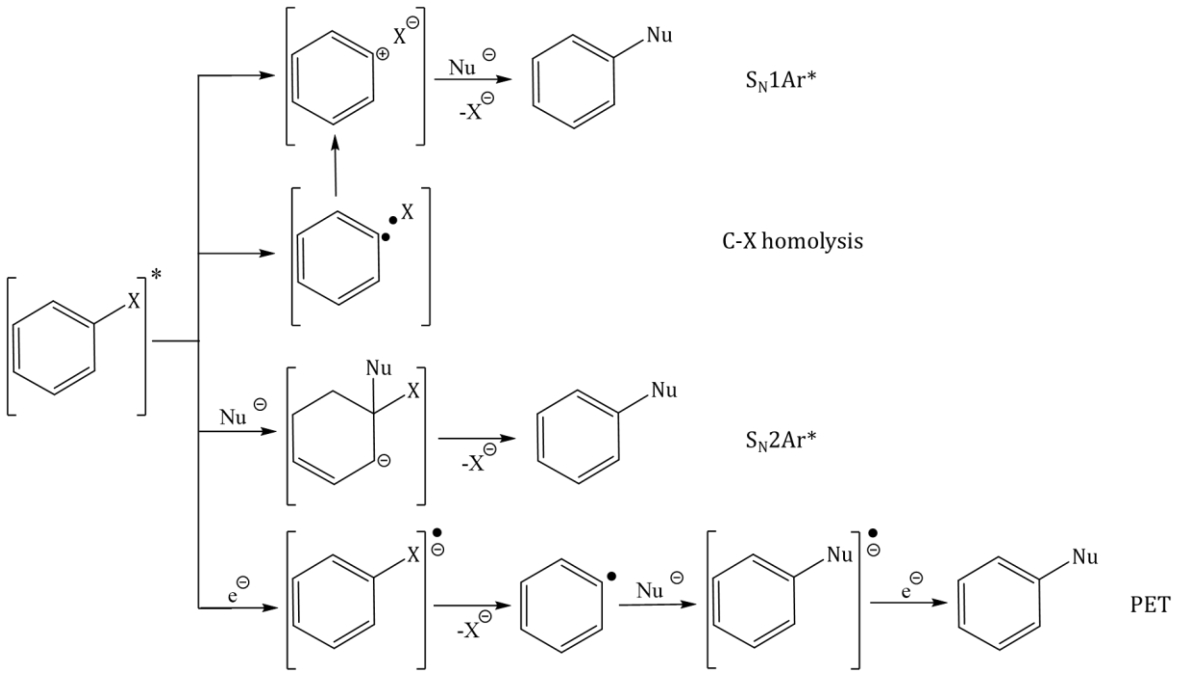

Scheme 11 : Main mechanisms of photoinduced nucleophile substitution in aromatic compounds[39]

Electronically excited aromatic compounds can also give rearrangements; Irradiated benzene, for example, can give rearrangements to benzvalene[40] and Dewar benzene[41], two non-aromatic highly energetic and strained products (Scheme 12).

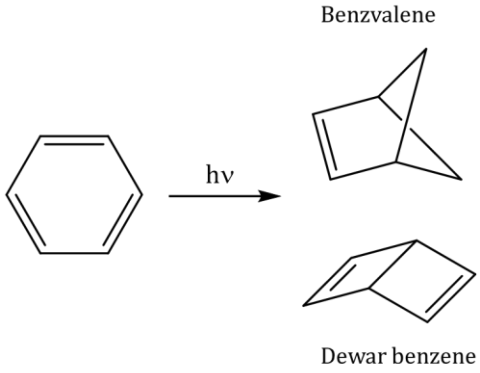

Scheme 12: two rearrangements obtained by excitation of benzene.

Carbonyl compounds are another class of very interesting photoreactive moieties. Ketones and aldehydes usually give a fast intersystem crossing that is particularly efficient in the case of Aryl

ketones, since the triplet state T_1 (π,π^*) is very close in energy to the singlet state S_1 (n,π^*), in accordance to El-Sayed rule[42, 43]. Thus, most of their photochemical reactions take place from the triplet excited state[15]. Among the possible photoinduced processes, the most common are α-cleavage (Norrish type I reaction), intramolecular H transfer (Norrish type II reaction) and photoreductions as intermolecular electron transfer and intermolecular H abstraction (Scheme 13).

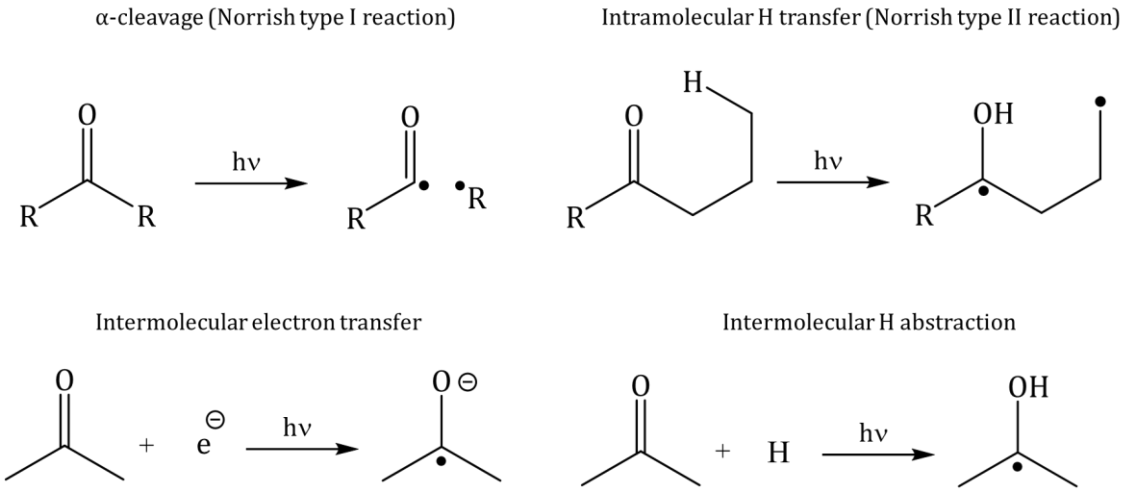

Scheme 13: Some photoreactions of carbonyl compounds

Among carbonyl compounds, carboxylic acids always exhibit a decarboxylation pathway. Acids give homolytic decarboxylation while carboxylic anions give an heterolytic pathway (Scheme 14).

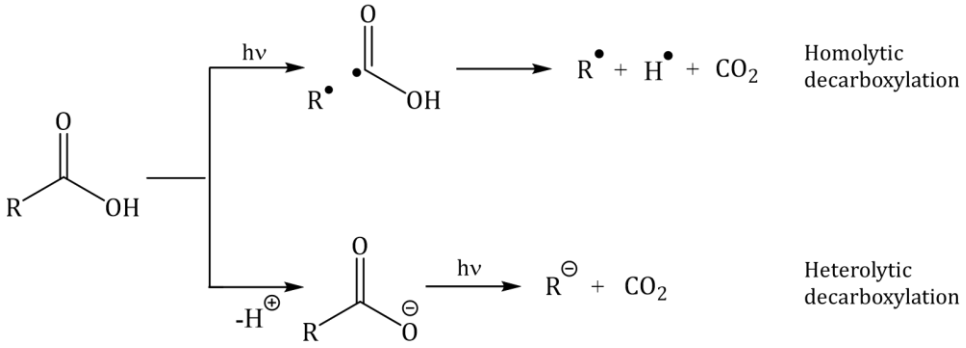

Scheme 14: photodecarboxylation pathways

Halogen molecules (X_2) give photofragmentation with an homolytic mechanism, while halogen containing organic molecules (R-X) can undergo homolytic photofragmentation or, in Aryl halides (Ar-X), direct nucleophilic photosubstitution (Scheme 11), as showed in Scheme 15.

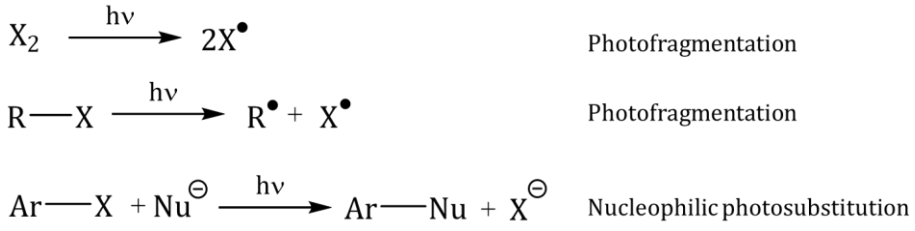

Scheme 15: Halogen photoreactions

In particular, Aryl halides in presence of bromine and iodine substituents give efficient intersystem crossing because of the heavy-atom effect, thus they can undergo homolytic photofragmentation both from singlet and triplet excited states, if their energies are greater than the Ar-X dissociation energy[15]. All this kind of photochemical processes are generally used for organic synthesis, since they often allow to overcome activation barriers that would make some products inaccessible[44] and more commonly for polymerization reactions, since they usually involve radical mechanisms. Photoiniziators for photopolymerization processes often are photoacid or photobase generators, which induce polymerization by generating an acid or a base in the medium[45].

1.3. Photochemistry of semiconductor nanomaterials

A semiconductor can be defined as a solid-state material whose bandgap energy for electronic excitation (E_g) lies between 0 and 4 eV (in metal or semimetal we have E_g=0 eV and in insulator E_g>3 eV)[46]. An important factor that defines semiconductor properties is the Fermi level E_F. It is the energy level that is occupied by an electron with the 50% of probability and its location between the upper level of the valence band and the lower level of the conduction band distinguishes intrinsic and extrinsic semiconductors. In an intrinsic semiconductor, the Fermi level is at the halfway between the valence and the conduction bands. For a doped semiconductor (extrinsic), the Fermi level is located more in proximity of the valence band or the conduction band, depending on the properties of the dopant element (p-type and n-type semiconductors). While the electronic structure of molecules is described by molecular orbitals theory, the one of

solid-state materials is described by band theory. Nevertheless, if we represent a solid as an assembly of many atoms, we can consider the band structure with the same interpretation that describes molecules behaviour. Thus, in solid state, valence band and conduction band are generated by the linear combination of atomic orbitals, as, in molecules, bonding and antibonding molecular orbitals[47]. While in molecules the energy is defined by orbitals, in a larger sized material the discrete character of the energy levels is lost, leading to bands formation (Figure 5).

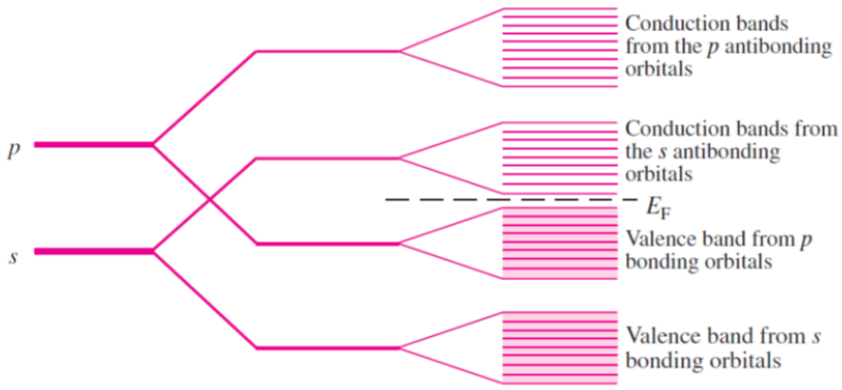

Figure 5: valence and conduction band represented as derived from atomic s and p orbitals. E_F is the Fermi level, reproduced from ref[47]

The most common and investigated semiconductors are inorganic semiconductors, such as silica or titanium dioxide. Nevertheless, in the last years also organic semiconductors have started to be studied thanks to their ease of preparation, properties tunability and lower costs. In particular, organic semiconductors are composed by an assembly of π-conjugated molecules connected by weak bonds such as Van Der Waals or π-stacking interactions[48, 49].

What happens if the size of a material becomes smaller and smaller? When the dimension of a material is in the orders of few nanometers, "quantum confinement effect" occurs. In semiconductor nanocrystals, usually called quantum dots (QDs), quantum confinement effect takes place when the size of the material is comparable or smaller than the length scale of the electronic motion in the bulk semiconductor, called the Bohr radius[50]. In this situation, the electron is confined, meaning that its mobility is limited by the size of the material. This leads to a quantization of the energy levels, which are not continuous as they were in the bulk; we can consider the nanomaterial electronic structure at the halfway between a molecule and a bulk material (Figure 6).

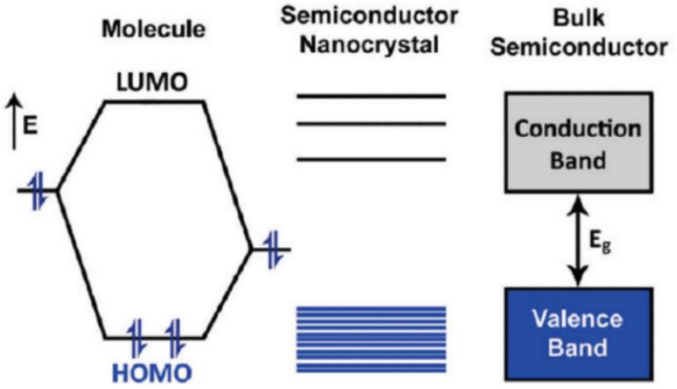

Figure 6: electronic energy states in a molecule, a semiconductor nanocrystal and a bulk semiconductor. Blue color denotes electronic occupation at the ground state. Reproduced from ref [51]

Furthermore, the stronger is the confinement, the larger is the separation between the energy levels[52]. In particular, the smaller is the size, the higher is the bandgap. Therefore, nanosized materials have optical and other chemical and physical properties that are different with respect to the bulk and that can be tuned by size changes. Preparation methods of semiconductor nanoparticles range from top-down to bottom-up approaches. Most common top-down methods are laser-ablation condensation, lithographic techniques[52] and deposition from the vapor phase such as molecular beam epitaxy (MBE) and metal-organic chemical vapor deposition (MOCVD)[53]. Bottom-up methods are usually based on the control of nucleation and growth of the particles in solution[53] by means of stabilizing agents; the most common strategies are sol and sol-gel processes and micelle assisted synthesis[50].

When a semiconductor absorbs light of the appropriate energy ($\geq E_g$), an electron is promoted to the conduction band, leaving a hole in the valence band. A bound electron-hole pair is thus generated, called “exciton”, and its fate defines semiconductor properties.

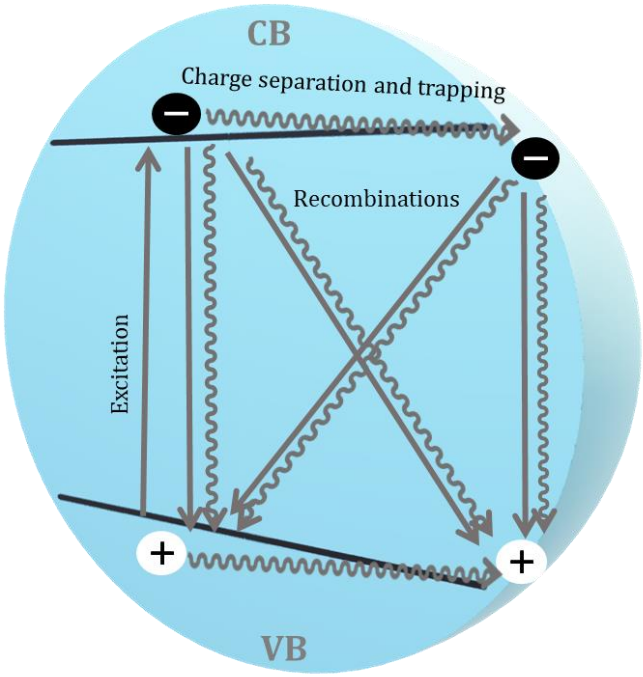

Scheme 16: primary processes of the electron and the hole after the exciton generation in a semiconductor.

Once the exciton is formed, one of the main processes that occur is the electron-hole recombination, which can be radiative or not radiative (respectively continuous and wavy lines in Scheme 16). In particular, for indirect semiconductors (transitions with change in momentum) radiative recombination are not favoured with respect to direct semiconductors (momentum-conserving transitions) because in the formers electronic momentum conservation occurs via a phonon interaction that consists of a quantum of lattice vibration[54]. As already mentioned, one of the most important features of nanomaterials are optical properties tuning. Indeed, quantum dots are widely used because of their broad absorption and their intense and narrow fluorescence that can be easily tuned with size and kind of material used[55] (Figure 7).

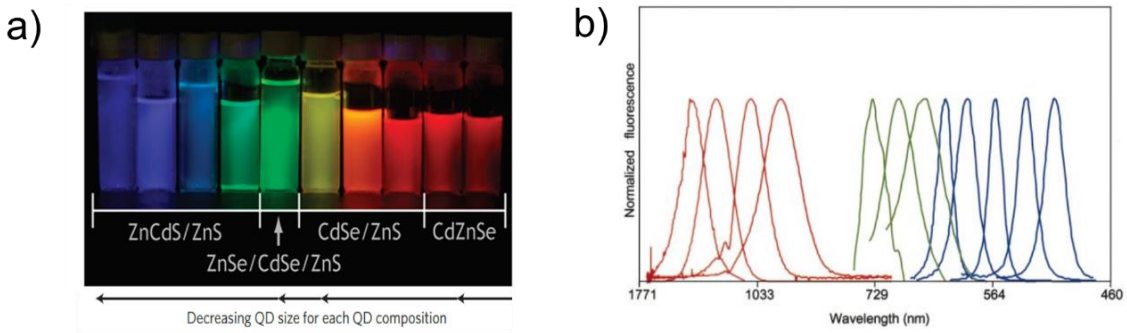

Figure 7: a) luminescent quantum dots of different size and composition (adapted from ref[56] and [57]) b) emission spectra of CdSe (blue series), InP (green series) and InAs (red series) at different sizes (adapted from ref[58]).

Their optical properties, coupled with their higher photostability, make them very convenient bioimaging markers with respect to organic dyes[59, 60]. In bioimaging field silica nanoparticles are surely the most investigated because of their low toxicity[61].

Besides charge recombination (usually highly favoured), another possible path of the electron-hole pair generated inside the semiconductor nanomaterial is charge separation and trapping. Defects in crystal lattices and unsaturated bonds on the surface act as trapping sites[51, 62]. Indeed, the electron/hole which migrates in the semiconductor can be stabilized and thus localized, "trapped" in these sites. However, this phenomenon leads to a decrease both in charge mobility and charge recombination properties[62]. Charge trapped states can also give recombination, which occasionally results in a bathochromic-shifted emission[63, 64]. If the presence of unsaturated bonds in the surface of a semiconductor could be a disadvantage for the reasons mentioned above, it is one of the main features of semiconductor photocatalysis: surface defects and dangling bonds are the active sites of a photocatalytic process. For this reason, photocatalysis is one of the main applications of nano-sized materials because they are mainly defined by their surface properties with respect to bulk properties, due to the high surface/volume ratio. Furthermore, with small size, surface tension increases, rising the photocatalytic reactivity[65]. Since a semiconductor is activated when a charge separation occurs, semiconductor-mediated photocatalytic mechanisms mostly involve redox processes. In particular, we can distinguish two kind of mechanisms: direct and indirect semiconductor photocatalysis[66], displayed in Figure 8.

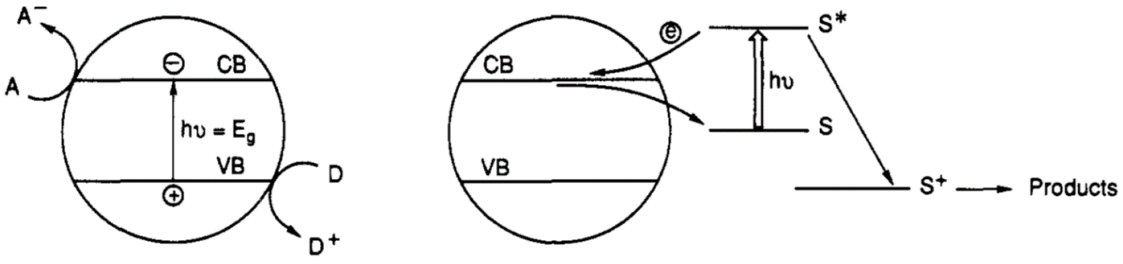

Figure 8: processes of charge transfer occurring at reactive semiconductor surfaces. Direct (left) and indirect (right) mechanisms. Reproduced from ref[67]

In direct semiconductor photocatalysis, the semiconductor is activated by direct bandgap excitation. Then, donors D and acceptors A are respectively oxidized and reduced by the charges trapped on the surface. Usually electron transfer efficiency is higher if the species A and D are adsorbed on the semiconductor surface but redox processes involving not adsorbed species have also been observed[66]. Indirect semiconductor photocatalysis instead consists of an electron transfer from and excited molecule adsorbed on the surface to the conduction band of the semiconductor. Since semiconductor photocatalysis is based on electron transfer processes, the

main issue to obtain a good photocatalytic efficiency is the minimization of charge recombination[68]. In order to avoid that, semiconductor-based systems are usually designed to increase as much as possible charge separation and mobility. This purpose can be achieved by reducing trapping sites along the charge pathway[69], as mentioned above, and by means of the combination of different materials such as the engineering of organic-inorganic hybrids[70], bulk heterojunctions[71] and modification by 2D materials, such as graphene, transition metal dichalcogenides and many others[72] (Figure 9).

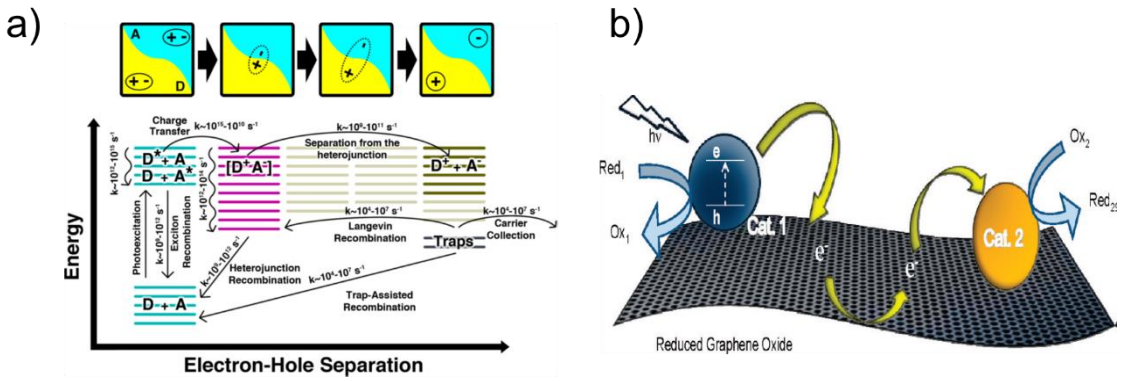

Figure 9: a)charge separation/recombination mechanisms in a photoexcited organic D/A material, reproduced from ref[73]b) selective catalysis at different size mediated by reduced graphene oxide, reproduced from ref[74].

The most studied photocatalytic semiconductor is Titanium dioxide (TiO_2), which, among its several applications, is the most employed photocatalyst in environmental purification[75, 76].

1.4. Bibliography

1. Dubusc, M; Soulie, A., Réactions photochimiques et anciens procédés de photographie. *Bulletin De L'Union Des Physiciens*, **1989**, *83* (718), 1299-1320
2. Popov, I. V., Aerial Photography and a Study of Inland Waters. U.S. Joint Publications Research Service, **1963.**
3. Gernsheim, H., A Concise History of Photography. Dover Publications, **1986**.
4. BnF -Les essentiels de la litterature. http://classes.bnf.fr/essentiels/grand/ess_2280.htm.
5. Noyes, W.A., Le rapport entre la spectroscopie et les réactions initiée par la lumière. BnF Gallica, **1937**.
6. Balzani, V., La fotochimica: un fenomeno naturale vecchio come il mondo, una scienza per il futuro. **1995**.
7. Ciamician, G., The photochemistry of the future. *Science* **1912,** *36* (926), 385-394.
8. Newton, I., A Letter of Mr. Isaac Newton, Professor of the Mathematicks in the University of Cambridge; Containing His New Theory about Light and Colors: Sent by the Author to the Publisher from Cambridge, Febr. 6. 1671/72; In Order to be Communicated to the R. Society, *Philosophical Transactions*, **1671,** *6* (69-80), 3075-3087.
9. Huygens, C., *Traité de la lumière*. **1690**.
10. Maxwell, J. C., VIII. A dynamical theory of the electromagnetic field. *Philosophical Transactions of the Royal Society of London* **1865,** *155* (0), 459-512.
11. Juris, A.; Moggi, L.; Gandolfi, M. T., Manuale del fotochimico. Tecniche e metodologie. Bononia University Press, **2006**.
12. Einstein, A., Über einen die Erzeugung und Verwandlung des Lichtes betreffenden heuristischen Gesichtspunkt. *Annalen der Physik* **1905,** *322* (6), 132-148.
13. De Broglie, L., Recherches sur la théorie des Quanta. *Annales de Physique* **1925,** *10* (3), 22-128.
14. Harris D.C.; Bertolucci M.D., Symmetry and Spectroscopy. Dover publications, **1978**.
15. Balzani, V.; Ceroni, P.; Juris, A., Photochemistry and Photophysics: concepts, research, applications. Wiley, **2014**.
16. Jablonski, A., Efficiency of Anti-Stokes Fluorescence in Dyes. *Nature* **1933,** *131* (3319), 839-840.
17. Lewis, G. N.; Kasha, M., Phosphorescence and the triplet state. *Journal of the American Chemical Society* **1944,** *66*, 2100-2116.

18. Kasha, M., Fifthy years of the Jablonski diagram. *Acta Physica Polonica*, **1987**, 471, 662-670.

19. Kuzmany, H., Symmetry and selection rules. In Solid state spectroscopy, Springer, Ed. **2009**, 149-168.

20. Myers Kelley, A., Electronic Spectroscopy. In Condensed-Phase Molecular Spectroscopy and Photophysics, Wiley, Ed. **2012**; 139-162.

21. Andrews, D. L., Molecular Photophysics and Spectroscopy. Morgan & Claypool Publishers **2014**.

22. A Crash Course in Photophysics and a Classification of Primary Photoreactions. In Photochemistry of Organic Compounds, Wiley, Ed. **2009**; 25-72.

23. Kasha, M., Characterization of electronic transitions in complex molecules. *Discussions of the Faraday Society* **1950,** (9), 14-19.

24. Balzani, V.; Moggi, L.; Manfrin, M. F.; Bolletta, F.; Laurence, G. S., Quenching and sensitization processes of coordination compounds, *Coordination Chemistry Reviews*, **1975,** *15* (4), 321-433.

25. Förster, T., Transfer Mechanisms of Electronic Excitation Energy, *Radiation research supplement*, **1960,** *2*, 326.

26. Dexter, D.L., A Theory of Sensitized Luminescence in Solids. *Journal of Chemical Physics* **1953,** *21*, 836.

27. Andrews, D. L., Resonance Energy Transfer. In Photonics: Scientific Foundations, Technology and Applications, Volume IV, John Wiley & Sons, I., Ed. **2015**, 101-128.

28. Blankenship, R.E., Antenna complexes and energy transfer processes In Molecular Mechanisms of Photosynthesis, 2nd Edition, Wiley-Blackwell, Ed. **2014**, 59-84.

29. Blankenship, R.E., The basic principles of photosynthetic energy storage. In Molecular Mechanisms of Photosynthesis, 2nd Edition, Wiley-Blackwell, Ed. **2014**, 1-9.

30. Gould, I. R.; Ege, D.; Moser, J. E.; Farid, S., Efficiencies of photoinduced electron-transfer reactions: role of the Marcus inverted region in return electron transfer within geminate radical-ion pairs. *Journal of the American Chemical Society* **1990,** *112* (11), 4290-4301.

31. Roth, H. D., Return electron transfer in radical ion pairs of triplet multiplicity. *Pure and Applied Chemistry* **2005,** *77* (6), 1075-1085.

32. Steiner, U. E.; Ulrich, T., Magnetic field effects in chemical kinetics and related phenomena. *Chemical Reviews* **1989,** *89* (1), 51-147.

33. Photochemical Reaction Mechanisms and Reaction Intermediates. In Photochemistry of Organic Compounds, Wiley, Ed. **2009**; pp 183-226.

34. Concepcion, J. J.; Brennaman, M. K.; Deyton, J. R.; Lebedeva, N. V.; Forbes, M. D. E.; Papanikolas, J. M.; Meyer, T. J., Excited-State Quenching by Proton-Coupled Electron Transfer. *Journal of the American Chemical Society* **2007,** *129* (22), 6968-6969.

35. Biczók, L.; Gupta, N.; Linschitz, H., Coupled Electron-Proton Transfer in Interactions of Triplet C60with Hydrogen-Bonded Phenols: Effects of Solvation, Deuteration, and Redox Potentials. *Journal of the American Chemical Society* **1997,** *119* (51), 12601-12609.

36. Albini, A.; Germani, L., Photochemical Methods. In *Handbook of Synthetic Photochemistry*, KGaA, W. V. V. G. C., Ed. **2009**, 1-24.

37. Klán, P.; Wirz, J., Photochemistry of organic compounds: from concept to practice. **2009**.

38. Shichida, Y.; Yoshizawa, T., Photochemical Aspect of Rhodopsin. In CRC Handbook of Organic Photochemistry and Photobiology, LLC, C. P., Ed. **2004**, 1–13.

39. Chemistry of Excited Molecules. In Photochemistry of Organic Compounds, Wiley, Ed. **2009**, 227-453.

40. Wilzbach, K. E.; Ritscher, J. S.; Kaplan, L., Benzvalene, the Tricyclic Valence Isomer of Benzene. *Journal of the American Chemical Society* **1967,** *89* (4), 1031-1032.

41. Bryce-Smith, D.; Gilbert, A.; Robinson, D. A., Direct Transformation of the Second Excited Singlet State of Benzene into Dewar-Benzene. *Angewandte Chemie International Edition in English* **1971,** *10* (10), 745-746.

42. El-Sayed, M. A., Triplet state. Its radiative and nonradiative properties. *Accounts of Chemical Research* **1968,** *1* (1), 8-16.

43. Baba, M., Intersystem Crossing in the1nπ* and1ππ* States. *The Journal of Physical Chemistry A* **2011,** *115* (34), 9514-9519.

44. Oelgemöller, M., Solar Photochemical Synthesis: From the Beginnings of Organic Photochemistry to the Solar Manufacturing of Commodity Chemicals. *Chemical Reviews* **2016,** *116* (17), 9664-9682.

45. Zivic, N.; Kuroishi, P. K.; Dumur, F.; Gigmes, D.; Dove, A. P.; Sardon, H., Recent Advances and Challenges in the Design of Organic Photoacid and Photobase Generators for Polymerizations. *Angewandte Chemie-International Edition* **2019,** *58* (31), 10410-10422.

46. Yu, P., Cardona, M., Introduction. In Fundamentals of Semiconductors, Springer, B., Heidelberg, Ed. **2010**.

47. Yu, P., Cardona, M., Electronic Band Structures. In Fundamentals of Semiconductors, Springer, B., Heidelberg, Ed. **2010**.

48. Clarke, T. M.; Durrant, J. R., Charge Photogeneration in Organic Solar Cells. *Chemical Reviews* **2010,** *110* (11), 6736-6767.

49. Ostroverkhova, O., Organic Optoelectronic Materials: Mechanisms and Applications. *Chemical Reviews* **2016,** *116* (22), 13279-13412.

50. Burda, C.; Chen, X.; Narayanan, R.; El-Sayed, M. A., Chemistry and Properties of Nanocrystals of Different Shapes. *Chemical Reviews* **2005,** *105* (4), 1025-1102.

51. Smith, A. M.; Nie, S., Semiconductor Nanocrystals: Structure, Properties, and Band Gap Engineering. *Accounts of Chemical Research* **2010,** *43* (2), 190-200.

52. El-Sayed, M. A., Small Is Different: Shape-, Size-, and Composition-Dependent Properties of Some Colloidal Semiconductor Nanocrystals. *Accounts of Chemical Research* **2004,** *37* (5), 326-333.

53. Nozik, A. J.; Beard, M. C.; Luther, J. M.; Law, M.; Ellingson, R. J.; Johnson, J. C., Semiconductor Quantum Dots and Quantum Dot Arrays and Applications of Multiple Exciton Generation to Third-Generation Photovoltaic Solar Cells. *Chemical Reviews* **2010,** *110* (11), 6873-6890.

54. Pankove, J. I., Optical Processes in Semiconductors. Prentice-Hall **1975**.

55. Medintz, I. L.; Uyeda, H. T.; Goldman, E. R.; Mattoussi, H., Quantum dot bioconjugates for imaging, labelling and sensing. *Nature Materials* **2005,** *4* (6), 435-446.

56. Shirasaki, Y.; Supran, G. J.; Bawendi, M. G.; Bulović, V., Emergence of colloidal quantum-dot light-emitting technologies. *Nature Photonics* **2013,** *7* (1), 13-23.

57. Anikeeva, P. O.; Halpert, J. E.; Bawendi, M. G.; Bulović, V., Quantum Dot Light-Emitting Devices with Electroluminescence Tunable over the Entire Visible Spectrum. *Nano Letters* **2009,** *9* (7), 2532-2536.

58. Bruchez Jr, M., Semiconductor Nanocrystals as Fluorescent Biological Labels. *Science* **1998,** *281* (5385), 2013-2016.

59. Kim, J. Y.; Voznyy, O.; Zhitomirsky, D.; Sargent, E. H., 25th Anniversary Article: Colloidal Quantum Dot Materials and Devices: A Quarter-Century of Advances. *Advanced Materials,* **2013,** *25* (36), 4986-5010.

60. Montalti, M.; Cantelli, A.; Battistelli, G., Nanodiamonds and silicon quantum dots: ultrastable and biocompatible luminescent nanoprobes for long-term bioimaging. *Chemical Society Reviews* **2015,** *44* (14), 4853-4921.

61. Bonacchi, S.; Genovese, D.; Juris, R.; Montalti, M.; Prodi, L.; Rampazzo, E.; Zaccheroni, N., Luminescent Silica Nanoparticles: Extending the Frontiers of Brightness. *Angewandte Chemie*, **2011,** *50* (18), 4056-4066.

62. Cordones, A. A.; Leone, S. R., Mechanisms for charge trapping in single semiconductor nanocrystals probed by fluorescence blinking. *Chemical Society Reviews* **2013,** *42* (8), 3209.

63. Landes, C.; Burda, C.; Braun, M.; El-Sayed, M. A., Photoluminescence of CdSe Nanoparticles in the Presence of a Hole Acceptor: n-Butylamine. *The Journal of Physical Chemistry B* **2001,** *105* (15), 2981-2986.

64. Underwood, D. F.; Kippeny, T.; Rosenthal, S. J., Ultrafast Carrier Dynamics in CdSe Nanocrystals Determined by Femtosecond Fluorescence Upconversion Spectroscopy. *The Journal of Physical Chemistry B* **2001,** *105* (2), 436-443.

65. Narayanan, R.; El-Sayed, M. A., Effect of Colloidal Catalysis on the Nanoparticle Size Distribution: Dendrimer−Pd vs PVP−Pd Nanoparticles Catalyzing the Suzuki Coupling Reaction†. *The Journal of Physical Chemistry B* **2004,** *108* (25), 8572-8580.

66. Kisch, H., Semiconductor Photocatalysis-Mechanistic and Synthetic Aspects. *Angewandte Chemie International Edition* **2013,** *52* (3), 812-847.

67. Kamat, P. V., Photochemistry on nonreactive and reactive (semiconductor) surfaces. *Chemical Reviews* **1993,** *93* (1), 267-300.

68. Chatterjee, D.; Dasgupta, S., Visible light induced photocatalytic degradation of organic pollutants. *Journal of Photochemistry and Photobiology C: Photochemistry Reviews* **2005,** *6* (2-3), 186-205.

69. Nie, W.; Tsai, H.; Asadpour, R.; Blancon, J. C.; Neukirch, A. J.; Gupta, G.; Crochet, J. J.; Chhowalla, M.; Tretiak, S.; Alam, M. A.; Wang, H. L.; Mohite, A. D., High-efficiency solution-processed perovskite solar cells with millimeter-scale grains. *Science* **2015,** *347* (6221), 522-525.

70. Manser, J. S.; Kamat, P. V., Band filling with free charge carriers in organometal halide perovskites. *Nature Photonics* **2014,** *8* (9), 737-743.

71. Kim, J. Y.; Lee, K.; Coates, N. E.; Moses, D.; Nguyen, T. Q.; Dante, M.; Heeger, A. J., Efficient Tandem Polymer Solar Cells Fabricated by All-Solution Processing. *Science* **2007,** *317* (5835), 222-225.

72. Chaves, A.; Azadani, J. G.; Alsalman, H.; Da Costa, D. R.; Frisenda, R.; Chaves, A. J.; Song, S. H.; Kim, Y. D.; He, D.; Zhou, J.; Castellanos-Gomez, A.; Peeters, F. M.; Liu, Z.; Hinkle, C. L.; Oh, S.-H.; Ye, P. D.; Koester, S. J.; Lee, Y. H.; Avouris, P.; Wang, X.; Low, T., Bandgap engineering of two-dimensional semiconductor materials. *npj 2D Materials and Applications* **2020,** *4* (1).

73. Savoie, B. M.; Jackson, N. E.; Chen, L. X.; Marks, T. J.; Ratner, M. A., Mesoscopic Features of Charge Generation in Organic Semiconductors. *Accounts of Chemical Research* **2014,** *47* (11), 3385-3394.

74. Lightcap, I. V.; Kosel, T. H.; Kamat, P. V., Anchoring Semiconductor and Metal Nanoparticles on a Two-Dimensional Catalyst Mat. Storing and Shuttling Electrons with Reduced Graphene Oxide. *Nano Letters* **2010,** *10* (2), 577-583.

75. Hoffmann, M. R.; Martin, S. T.; Choi, W. Y.; Bahnemann, D. W., Environmental applications of semiconductor photocatalysis. *Chemical Reviews* **1995,** *95* (1), 69-96.

76. Schneider, J.; Matsuoka, M.; Takeuchi, M.; Zhang, J.; Horiuchi, Y.; Anpo, M.; Bahnemann, D. W., Understanding TiO2Photocatalysis: Mechanisms and Materials. *Chemical Reviews* **2014,** *114* (19), 9919-9986.

2. Photoinduced dissolution and photoinduced precipitation of calcium carbonate

2.1. Introduction

Among photoactive molecules and, more specifically, among photoinitiators that, by means of their photo-induced transformation, trigger other chemical reactions, photoacid and photobase are assuming more and more interest from researchers, with a view to many new applications. A photoacid or photobase is a molecule whose excited state, populated with a light stimulus, has respectively a more acidic or a more alkaline pH with respect to the ground state[1, 2]. This kind of molecules, usually responsible of proton transfer processes[3], have a pH change that disappears in the time of deactivation of the excited state (10^{-9}-10^{-6} s) unless the occurrence of a reversible or irreversible photoreaction[4]. A photoacid/photobase that undergoes an irreversible process before its excited state deactivation is called photoacid/photobase generator (PAG/PBG)[5]. So far, many categories of molecules with PAG and PBG properties has been studied. Among photoacid generators, two main groups can be identified: ionic and non-ionic PAG[5]. Among ionic PAG, onium salts (diarylhalonium salts, aryldiazonium salts, triarylsulfonium salts), are the most common ones because of their thermal stability[6]. The photolysis mechanism occurring in onium salts leads to the generation of Brønsted acid in diaryhalonium (Scheme 1-a) and triarylsulfonium salts[7, 8] and of Lewis acid in aryldiazonium salts[9]. Among non-ionic photoacid generators, the most common are arylsulfonate esters and in particular 2-nitrobenzil esters[10] (Scheme 1-b), imidosulfonate and iminosulfonate esters[11].

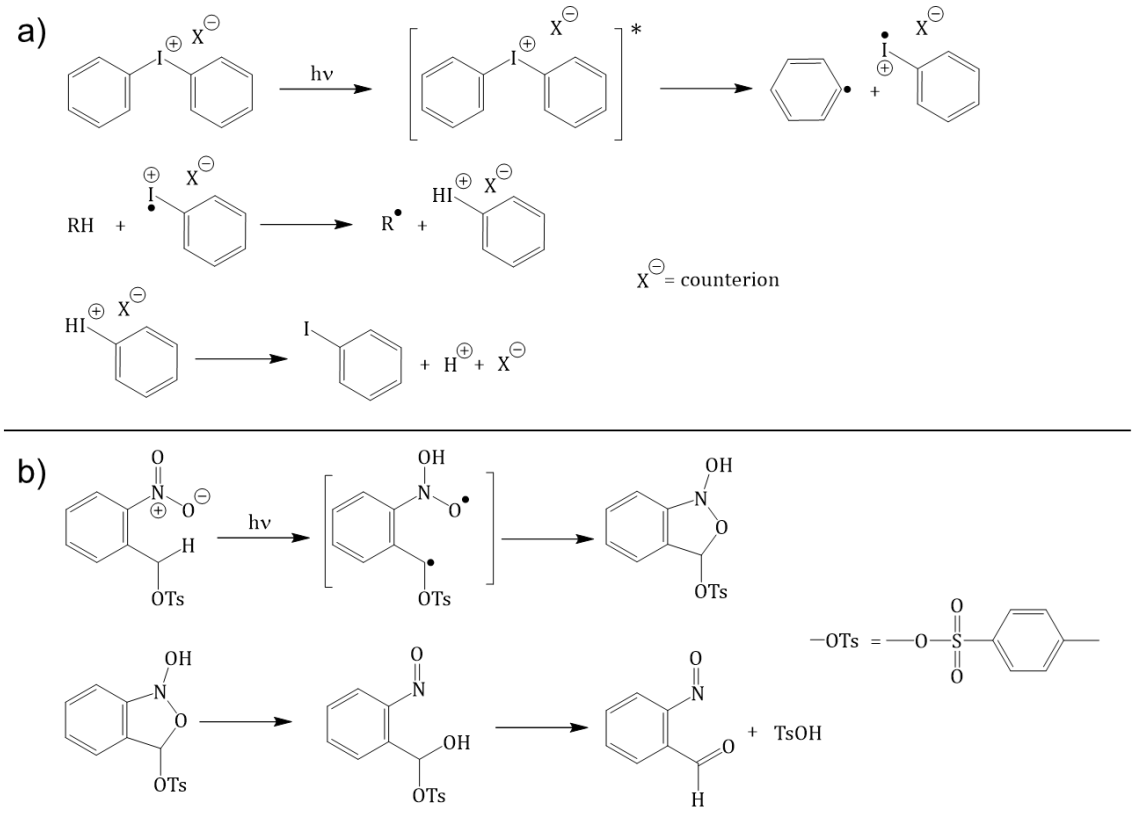

Scheme 1: Photolysis mechanisms of a Daryliodonium salt[7] (a) and of 2-nitrobenzil tosylate[6, 10] (b) as examples respectively of ionic and non-ionic PAG

Photobase generators are less common than photoacid generators but they are anyhow interesting, because they can have advantages with respect to PAGs in application that, for example, involve the use of metal substrates that could undergo corrosion with a too acidic pH[12]. Even in the field of photobase generators, ionic and non-ionic ones can be distinguished. Quaternary ammonium salts[13] and carbamates[14] are respectively the most common ionic and non-ionic ones (Scheme 2).

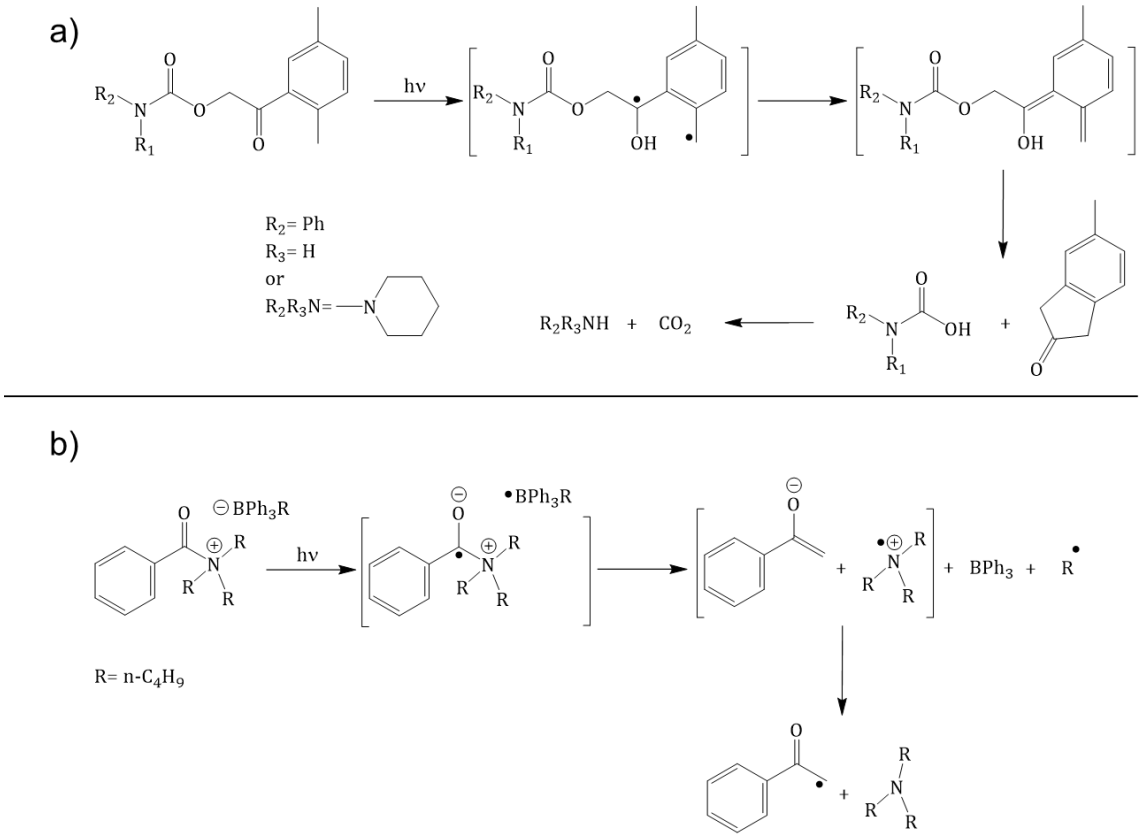

Scheme 2: a) photolysis of a carbamate as a non-ionic PBG. Carbamates reaction can generate either a secondary or a tertiary amine[12, 14]. b) photolysis of a quaternary ammonium salt with a borate anion. Based on the counterion, the mechanism can change[12].

In addition to these molecules, another common non-ionic PBG is Ketoprofen, a drug with a benzophenone chromophore that undergo photodecarboxylation[15] and another ionic PBG is Tetraphenylborate ion that is usually used in organocatalysis[6]. Nowadays, both photobase and photoacid generators have been widely developed and one of the main aim of this field is to make these species, which are generally excited by UV light, activated also with Near-UV or Visible light, in order to enlarge the application spectrum, have low cost equipment (i.e. LEDs) and more selectivity in the irradiation process[12]. Based on these considerations, PAG and PBG groups can be linked to chromophores or coupled with sensitizers.

Photoacid generators and photobase generators have been investigated for several years and are part of many applications. Figure 1 shows the main PAG and PBG coupled with their applications.

Table 1. Photoacid Generator

Type	Generated acid	Solubility in common organic solvents	Thermal stability	Application
Ionic				
Diaryldiazonium salt	Lewis acid	Good	Poor	Photoinitiator (UV curing material)
Diaryliodonium salt	Brönsted acid	Poor	Good	
Triarylsulfonium salt	Brönsted acid	Poor	Good	Catalyst for polymer reaction (Photoresist)
Non-ionic				
2-Nitrobenzyl ester of sulfonic acid			Depend on structure	Catalyst for polymer reaction (Photoresist)
Imino sulfonate	Sulfonic acid	Good		
N-Sulfonyloxyimide				
Aromatic sulfone				

Table 2. Photobase Generator

Type	Generated base	Solubility in common organic solvent	Thermal stability	Application
Ionic				
Cobalt amine complex	Ammonia	Poor	Good	
	Alkyl amine			Catalyst for polymer reaction and curing (Photoresist and UV curing material)
Non-ionic				
Carbamate	Alkylamine		Depend on structure	
O-Acyloxime	Aralkyl amine	Good		
Formanilide	Aromatic amine			

Figure 1: main PAGs (Table 1) and PBGs (Table 2), their properties and applications, reproduced from [9].

Figure 1 shows the main applications for which photoacid and photobase generators have been developed and studied, such as catalysts for polymer synthesis, crosslinking and degradation and photoinitiators for UV curing. One of the main fields in which these kinds of reactions are involved is surely photolithography. The photogenerated acid or base usually triggers a change of the polymer solubility or a cross-linking reaction between the polymer chains[14]. Moreover, they have also been used for other purposes, such as changing the assembly of molecules and nanoparticles[16, 17].

During my PhD, these molecules were studied with another aim: controlling the precipitation/crystallization and the dissolution of materials with the pH variations induced by light.

The possibility to localize precipitation/dissolution of materials with a remote, non-invasive stimulus such as light can be a real improvement in many applications in advanced Materials Science such as micropatterning and bone and teeth restoration (if phosphate behaviour can be controlled). Furthermore, a deeper understanding of chemical composition of the growth units building the crystals and the process of crystallization can be very relevant both for biological mineralization and mineral synthesis. So far, our specific purpose has been to control the crystallization and the dissolution of Calcium Carbonate ($CaCO_3$), because it is one of the most

important inorganic chemical products, with many implications in biological, environmental, industrial, and technological processes. Furthermore, $CaCO_3$ can be used as a model system because the process of crystallization and dissolution are strongly influenced by pH variations. In this work, the precipitation and dissolution of calcium carbonate has been treated in the optics of artworks restoration.

Cultural Heritage is to the basics of our society as it defines the identity of a civilization by telling its history. Furthermore, tourists interest on cultural experiences is continuously increasing[18]. Therefore, the preservation of cultural heritage is fundamental from political, sociological, anthropological and economical points of view[19]. Artworks are constantly subjected to deterioration that is mainly due to instability of the materials, water soluble salts, humidity and temperature conditions, atmospheric pollutants and biological action[20]. Since an artwork can be affected by a lot of factors, which also depend on its original components, prediction and contrast of their impact is always challenging. So far, many methods have been developed for restoration that usually involves two steps: cleaning and consolidation[19]. The cleaning process aims to remove, by means of solvents, unwanted layers from the surface of artworks that are usually dust, grease and natural and synthetic products used in conservation practice[21]. The main drawbacks related to the use of solvents are non-selectivity, thus the risk of dissolving also part of the original artwork, and toxicity[21]. The consolidation is performed to avoid or slow down further degradation of the artwork. Resins, especially acrylic polymers and silicones[22], are usually employed as strengthen agents or water repellents[23]. Nevertheless, this kind of techniques often induce a permanent modification of the artwork and polymers are themselves subject to degradation by external agents, occasionally leading to yellowing of the surface[24]. Fresco is one of the most ancient artwork techniques, widely developed already by Roman civilization[25]. This mural painting is mainly obtained by lime and sand. A first plaster (*arriccio*), which is the richest in sand, is laid on the wall, followed by a finer plaster with an equal amount of lime and sand (*intonaco*) and the paint layer, in which the pigments are usually mixed with limewater and fixed on the surface by carbonation[26, 27]. Since mural paintings are always more subjected to weather phenomena as humidity and temperature changes, restoration of fresco is always very demanding. In this work, a new restoration technique based on light-controlled cleaning and deposition of calcium carbonate on a surface is presented, using respectively photoacid and photobase generators. Indeed, using photoactive molecules in the order of millimolar concentrations, it is possible to create a variation of two units of pH[28]. This change in pH is large enough to provoke the precipitation or dissolution of calcium carbonate phases[29].

Calcium carbonate precipitation/dissolution on fresco surfaces can be highly controlled and localized by this light-induced method. Moreover, the use of solvents that lead to unwanted modifications of the artwork or are toxic for the restorer can be avoided. In this new approach,

we have developed an easy and safe protocol of restoration of frescoes that is based on the precise modification of $CaCO_3$, which is the main component of these kind of artworks.

The photoinduced precipitation/dissolution process has been first studied in solution for artworks restoration. Then, the crystallization process was also fixed in a matrix: this allows a deep study of crystallization process and a future application in micropatterning.

2.2. Photodissolution of Calcium Carbonate by means of a Photoacid generator

2.2.1. Materials

Irradiation sources

- LED (2.2 mmx2.2 mm light emitting surface) purchased by LED engine. The irradiation wavelength is 365 nm with a radiant flux of 3.3 W (Forward current 700 mA) at 25°C. The LED has a viewing angle (the off-axis angle from the centreline where the radiometric power is the 50% of the peak value) of 110°.
- LED (3.2 mm ø) purchased by Mouser Electronics is used. The irradiation wavelength is 365 nm with a radiant flux of 1320 mW (Forward current 700 mA) at 25°C. The LED has a viewing angle (the off-axis angle from the centreline where the radiometric power is the 50% of the peak value) of 70°.
- LED (6.4 mm ø) purchased by Mouser Electronics. The irradiation wavelength is 395 nm with a radiant flux of 3 W (Forward current 700 mA) at 25°C. The LED has a viewing angle (the off-axis angle from the centreline where the radiometric power is the 50% of the peak value) of 45°.
- Spectrofluorimeter Horiba Fluoromax 4 was used for irradiation in the study of sensitization of Diphenyliodonium hexafluorophosphate by Thioxanthene-9-one.

Photodissolution tests in solution

Diphenyliodonium hexafluorophosphate (DIP) purchased by Sigma Aldrich was used as a photoacid generator. DIP was dissolved in a water/ethanol mixture 1:1 to obtain DIP concentrations of 0.02M. Then $CaCO_3$ powder (Sigma Aldrich) was placed in the solution to have a concentration of 0.005 M. This concentration was chosen in order to avoid $CaCO_3$ dissolution at the beginning of the test, considering that $CaCO_3$ solubility at pH 8 in water is almost 0.001 M[30]. Irradiation was performed on 4mL vials (Ø 15mmx45mm) filled respectively with 3 mL of DPI solution 0.02M in H_2O/EtOH 1:1. 1.5 mg of $CaCO_3$ were added to have a $CaCO_3$ concentration of 0.005 M. The LED (3.3W) was placed horizontally, at 3 cm from the vial. This distance corresponds to an irradiance of 36700 $W \cdot m^{-2}$ on a light spot with 1,1 cm of diameter, measured considering an angular displacement of 20°. The irradiation was performed for two hours.

Characterization of DIP and organic byproducts

Absorption spectroscopy

Absorption spectra were performed by means of a UV-Vis spectrophotometer (Perkin Elmer Lambda 650) on DIP in water/ethanol mixture before and after LED irradiation for two hours.

Mass spectrometry

Electronic impact mass spectrometry (GC-MS) was performed on DIP 20 mM solution after irradiation.

PH measurements

PH measurements were performed by means of a pH-meter, monitoring the pH of DIP 20mM solution in water/ethanol 1:1 mixture during the irradiation and in dark.

Photodissolution tests on a $CaCO_3$ spot (water/ethanol mixture)

1µL of $CaCO_3$ crystals (calcite) aqueous dispersion was placed on a glass slide and left drying for 1 hour. Then, 10 µL of DIP solution 40 mM in water/ethanol 1:1 was placed on the dried spot. The glass slide was placed under the LED at 365 nm (distance of 2 cm) and irradiated for 40 minutes. This distance corresponds to an irradiance of 80487 $W \cdot m^{-2}$ on a light spot with 0.7 cm of diameter, measured considering an angular displacement of 20°. The test was monitored with a camera collecting frames each 15 seconds.

Photodissolution tests on a $CaCO_3$ spot (water/ethylene glycol mixture)

2µL of $CaCO_3$ 2 mg/mL aqueous dispersion was placed on a glass slide and left drying for 1 hour. Then, 10 µL of DIP solution 40 mM in water/ethylene glycol 40:60 was placed on the dried spot. The glass slide was placed under the LED (1320 mW) at 365 nm (distance of 2 cm) and irradiated for 15 minutes. This distance corresponds to an irradiance of 32200 $W \cdot m^{-2}$ on a light spot of 0.7 cm of diameter, measured considering an angular displacement of 20°. After irradiation, the DIP solution was washed with MilliQ water.

Study of sensitization of Diphenyliodonium hexafluorophosphate (DIP) by Thioxanthene-9-one in solution.

Diphenyliodonium hexafluorophosphate (DIP) purchased by Sigma Aldrich was used as a photoacid generator and Thioxanthene-9-one, purchased by Baker Chemicals, was used as sensitizer. DIP 0.5 mM and Thioxanthene-9-one 0.5 mM were dissolved in a water/ethanol mixture 1:1 and irradiated in quartz cuvette by means of a spectrofluorimeter (Horiba Fluoromax-4) at a wavelength of 385 nm. As a reference, DIP 0.5 mM in ethanol was also irradiated with the spectrofluorimeter at 280 nm.

Absorption spectroscopy

Absorption spectra were performed by means of a UV-Vis spectrophotometer (Perkin Elmer Lambda 650) on DIP 0.5 mM in water/ethanol 1:1 before and after irradiation at 280 nm and DIP 0.5 mM and Thioxanthene-9-one 0.5 mM before and after irradiation at 385 nm.

Mass spectrometry

Electronic impact mass spectrometry (GC-MS) was performed on DIP 20 mM and Thioxanthene-9-one 0.5 mM solution in water/ethanol 1:1 after an irradiation.

PH measurements

PH measurements were performed by means of a pH-meter, monitoring the pH variation of DIP 0.5mM solution during irradiation at 280 nm and DIP 0.5 mM and Thioxanthene-9-one 0.5 mM during irradiation at 385 nm. In both the tests, the pH was monitored every minute for the first three measurements and then every 5 minutes and ten minutes based on the rate of the pH variation, until pH stabilization.

Photodissolution tests on a $CaCO_3$ spot for Diphenyliodonium hexafluorophosphate (DIP) sensitized by Thioxanthene-9-one.

10µL of calcite crystals 2 mg/mL aqueous dispersion sonicated for 10 minutes was placed on a glass slide and left drying for 2-3 hours. Then, 10 µL of DIP solution 20 mM and Thioxanthene-9-one 0,5 mM in water:ethanol:ethylene glycol 1:1:2 were placed on the dried spot. The $CaCO_3$ spot was irradiated by a fluorescence microscope adapted for irradiation. In particular, the bottom of the glass slide, in which the $CaCO_3$ and the solution were placed, was irradiated by a 365 nm/395 nm LED (3.3W) focused by the microscope lens. After 5 minutes of irradiation, the top solution was washed with MilliQ water.

Localized irradiation setup

The irradiation was performed in a fluorescence microscope (Olympus IX71) (Figure 1). The LED source was placed in correspondence to the light source of the fluorescence microscope and no filter in excitation was set up. Irradiation was performed with a 10x objective. Images were collected with a camera during irradiation every minute. In particular, the irradiation was stopped every minute and the image was collected in backscattering by illuminating one side of the sample with a tungsten lamp, to see the calcite crystals, not clearly observable with the microscope transmission or fluorescence mode.

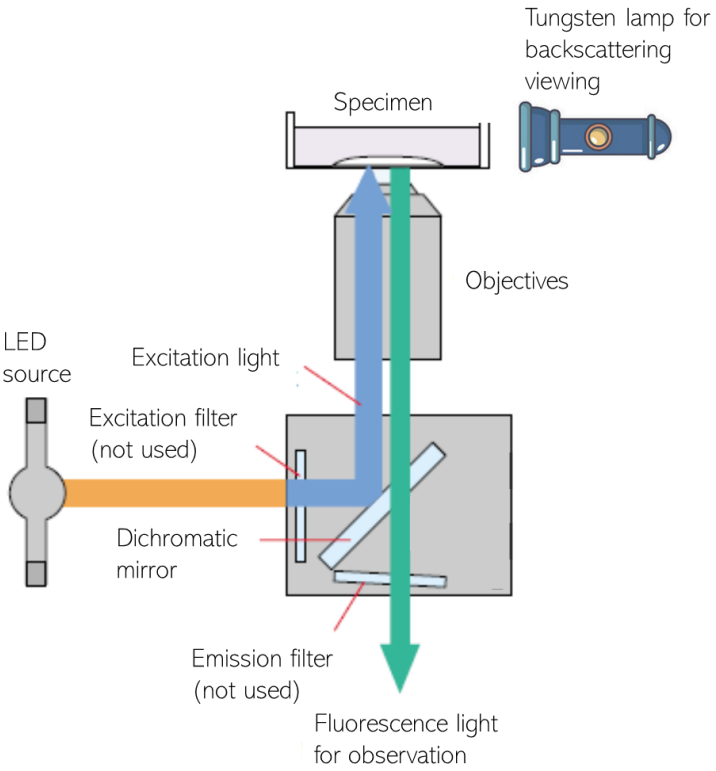

Figure 1: Irradiation setup in the fluorescence microscope (readapted from Olympus IX71 manual). Irradiation source at 365 nm

The irradiation sources were the LED (3.3 W) at 365 nm and the LED (3W) at 395 nm. The LED-focal plane distance in the fluorescence microscope is 25 cm and the irradiated area of the spot has a diameter of 0.2 mm. The irradiance in these conditions is 1.05×10^{8} W m^{-2}.
The LED-focal plane distance in the fluorescence microscope is 25 cm and the irradiated area of the spot has a diameter of 0.4 mm. The irradiance in these conditions is 2.3×10^{7} W m^{-2}.

2.2.2. Results

A diarylhalonium salt was used for the photodissolution of calcium carbonate: diphenyliodonium hexafluorophosphate (DIP). As mentioned in the introduction (2.1), Diaryliodonium salts generate Bronsted acids under UV light irradiation and the possible mechanisms of their direct photolysis have been widely investigated[31]: a radical process has been considered as the main pathway[32-34].

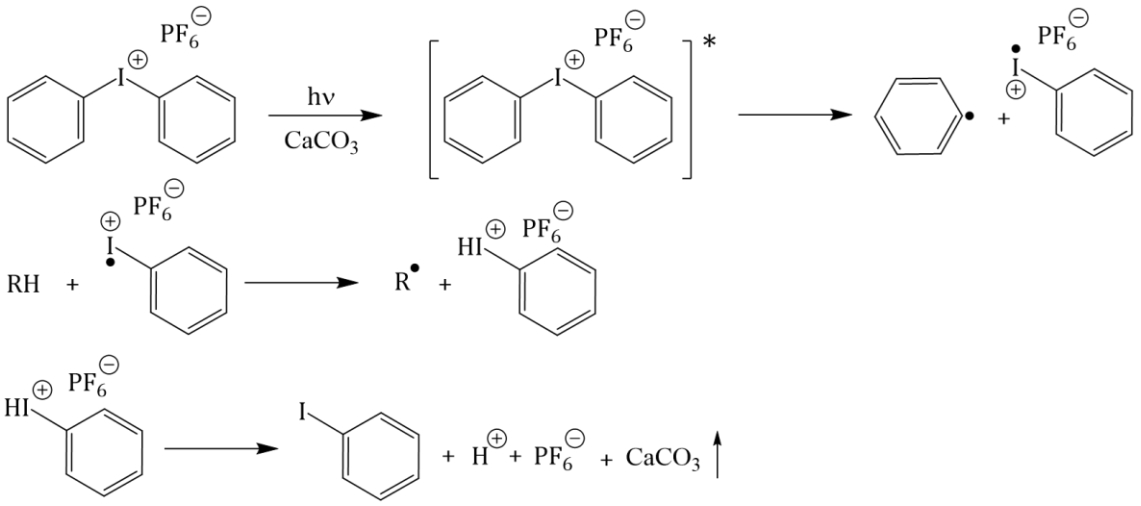

Scheme 1: Photodecomposition mechanism of DIP

Scheme 1 shows the radical pathway given by direct photolysis of diphenyliodonium hexafluorophosphate. The reaction generates Iodobenzene as the main byproduct and the decrease in pH would induce $CaCO_3$ dissolution.

First, DIP solution with calcium carbonate was irradiated by a 365 nm LED, entirely in solution, to understand the reaction mechanism and the best conditions in which the dissolution of calcium carbonate could be achieved. Since DIP byproducts are not soluble in pure water, a water/ethanol 1:1 mixture was chosen as the solvent. Calcium carbonate 0.005M solutions were used for the test. DIP concentration 0.02 M and LED distance 3cm were chosen as the best conditions. Test was performed irradiating 3 mL of the DIP solution in presence of $CaCO_3$ for two hours. $CaCO_3$ dissolution was observed after 1 hour and 30 minutes. Based on this test setup, characterization of the photoacid generator by absorption spectroscopy (Figure 2) and mass spectrometry (Figure 3) and study of pH variation (Figure 4) during the process were performed.

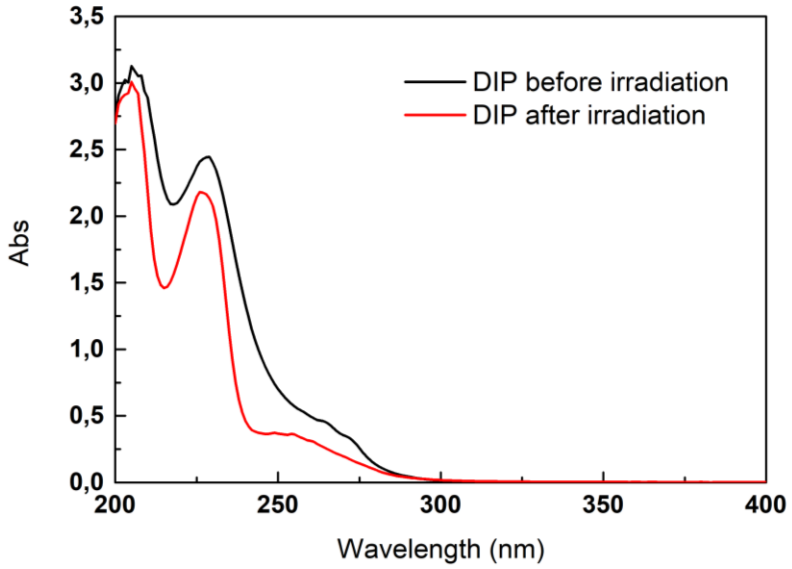

Figure 2: Absorption spectra of DIP in water/ethanol 1:1 before (black) and after (red) an irradiation of two hours. Spectra were collected after a 100-fold dilution of DIP solution (final concentration 0.2 mM).

Figure 2 shows absorption spectra of DIP before and after irradiation in a water/ethanol mixture. The first aspect to notice is that the DIP absorption spectrum tail ends at 300 nm and almost no absorbance is observed at 365 nm. Thus, using a shorter wavelength to irradiate the system would surely lead to a more efficient DIP activation. However, we decided to use a 365 nm source for irradiation and increase the DIP concentration to have a higher performance because using a shorter wavelength could lead to a lot of disadvantages. First, sources that work below the Near-UV wavelength range are always very expensive. Moreover, they have a significative unsafety for the operator, considering that the person who is going to use this kind of system for artwork restoration may not be used to work with powerful and dangerous lamps. In addition, our eye cannot perceive UV light, while it would be better to be able to clearly see the area hit by the light, to improve precision. Finally, since in frescoes surface a lot of pigments can be mixed with the calcium carbonate layer, using a UV source could also lead to an alteration of the colours of the fresco.

Absorption spectra of the solution before and after irradiation, reported in Figure 2, do not show relevant differences in intensity but in spectral shape. In particular, both the spectra show the typical shape of Iodobenzen[35], which represents both the DIP chromophore and the main organic byproduct generated after irradiation. However, the differences in the spectra shape can suggest a modification in the interactions which Iodobenzene moiety undergoes. This can be associated to the photoinduced process, after which the Iodobenzene and benzene moieties are detached. The process is then definitely confirmed by GC-Mass spectrometry, reported in Figure 3.

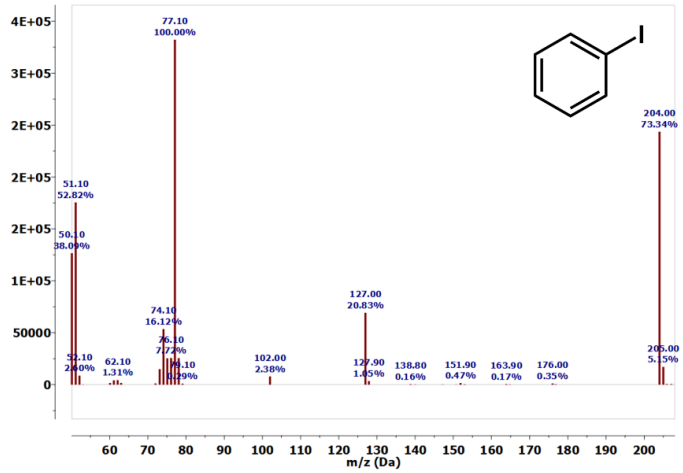

Figure 3: mass spectrum (GC-MS) of DIP solution irradiated for two hours. Mass spectrum representing Iodobenzen, corresponding to retention time 6.18, is reported.

Figure 3 shows mass spectrum of Iodobenzene, corresponding to retention time of 6.18 min; this confirms the mechanism reported in Scheme 1 for the photodegradation of Diphenyliodonium hexafluorophosphate. GC-MS also detected another peak at 14.9 min of retention time. This corresponds to unreacted DIP. This can be expected because of the less efficient reaction given by the too high irradiation wavelength.

PH variation was monitored during DIP 0.02M light irradiation and compared to pH variation of the sample in dark (Figure 4), in order to monitor the jump in pH which could be achieved by light irradiation in the test conditions.

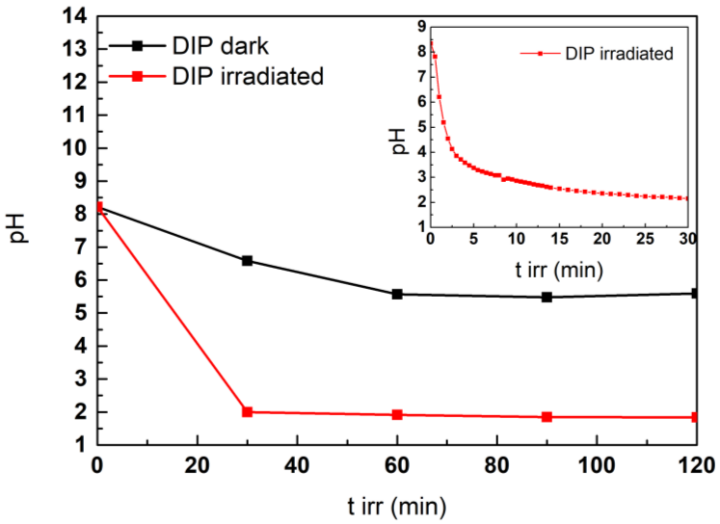

Figure 4: pH variation in DIP solution kept in dark (black) and irradiated (red) for two hours, measuring the pH each 30 minutes. Inset: pH variation of irradiated DIP in the first 30 minutes measuring the pH every 30 seconds for the first 14 minutes and then every minute.

Figure 4 shows that there is a relevant pH variation during the irradiation at 365 nm, compared to DIP in dark. A pH variation in dark is anyway observed: the initial pH is almost 8, but it starts almost immediately to decrease until a value of 5.5-6 after one hour, which is then maintained. PH value in dark was also measured after one day and is stable at 5.5-6. Despite the decrease of pH in dark, the final pH is not acidic enough to induce the dissolution of calcite in the conditions in which the tests are performed. Calcium carbonate dissolution is favoured at pH<4[36], so it is necessary to achieve a lower pH value in the medium in order to efficiently dissolve $CaCO_3$. In the irradiated sample a very relevant decrease in pH is observed, until a value of almost 2, which induces the dissolution of calcite. Inset the more detailed decrease of pH in the first 30 minutes is reported. A very fast decrease in pH until a value of almost 4 is observed in the first 2.5 minutes, then the pH jump become slower and the pH value of 2.1 is obtained only after 30 minutes of irradiation. This trend is in accordance to tests in solution, in which the $CaCO_3$ complete dissolution can be achieved only after one hour and 30 minutes. This is quite a long time for the final application, that can be explained by the lack of overlap between the light source and the absorption spectrum (Figure 2). Indeed, after having performed tests in solution to just investigate the $CaCO_3$ dissolution mechanism, it was necessary to test the system with a setup closer to the final application, and thus also reducing the time of irradiation. In artworks restoration, the aim is to clean a surface, thus it is necessary to have a deposition of $CaCO_3$, on which a low quantity of the PAG solution must be dropped. Thus, photodissolution tests were performed on a $CaCO_3$ spot made of calcite crystals deposited on a glass slide surface. A water/ethanol 1:1 solution of DIP 0.04 M was used, instead of DIP 0.02 M used in the tests in solution, to further fasten the process. For the same reason, the LED was placed at 2cm from the sample, instead of 3. With this setup, the dissolution of calcium carbonate crystals can be achieved in 40 minutes (Figure 5).

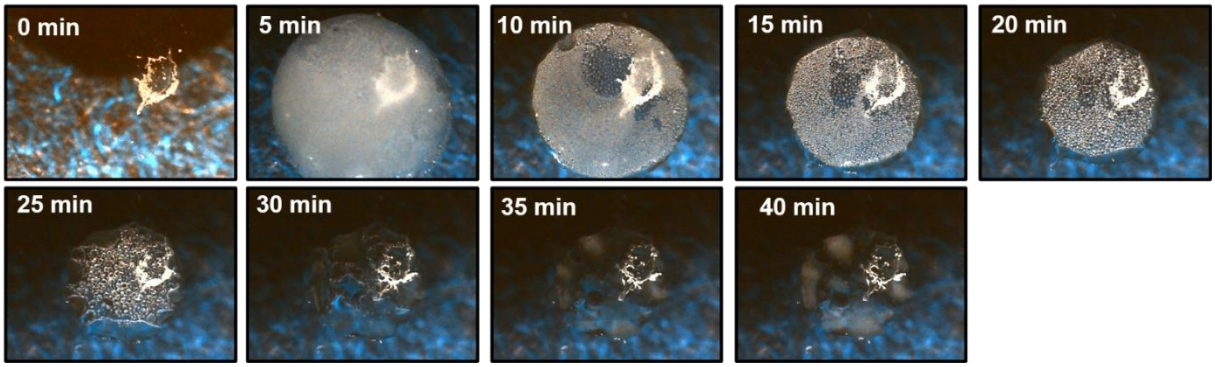

Figure 5: frames collected every 5 minutes during the irradiation process of a calcite crystal with the DIP 0.04M solution on top. After 40 minutes almost all the crystal is dissolved.

As Figure 5 shows, DIP starts to react in the first minutes of irradiation, in which the little drops of organic byproduct start already to appear. Nevertheless, the $CaCO_3$ dissolution starts after 15 minutes and become more evident after 30 minutes.

As mentioned, the concomitant evaporation of the drop leads to the precipitation of the organic byproduct, which is a light brown oil. It can be easily removed afterwards by means of ethanol, but it still represents a problem because evaporation starts immediately and could have an influence on the $CaCO_3$ dissolution process. Furthermore, it is necessary to put at least 10 µL of DIP 0.04 M on a 1µL drop of calcium carbonate dispersion or 5 µL of DIP 0.04 M on a 0.5µL drop of calcium carbonate dispersion in order to avoid DIP precipitation prior to irradiation. DIP precipitation prior to irradiation is observed also by increasing DIP concentration in solution. The scarce control on the evaporation of DIP is a relevant issue, since in this situation the process does not occur with the highest efficiency and it is not reproducible because it depends on many factors, such as temperature. In order to avoid solvent evaporation and precipitation of DIP or its organic byproducts during the irradiation process (Figure 5), a water/ethylene glycol 40:60 solution was used, instead of a water/ethanol 1:1 mixture. Furthermore, a more focused LED, which allows a better localization of the irradiated area, was placed at 2 cm from the sample. In these conditions, complete $CaCO_3$ dissolution is achieved in 15 minutes of irradiation, considerably fastening the whole process. Then, the system can be efficiently washed with MilliQ water and no traces of DIP solution or $CaCO_3$ spot remain on the glass slide (Figure 6).

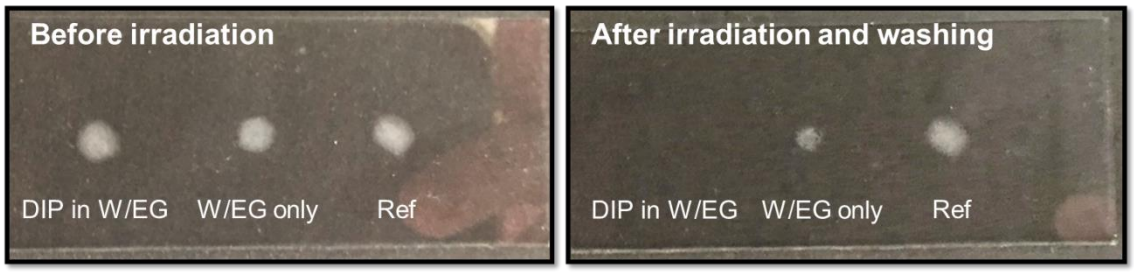

Figure 6: spots deposited on a glass slide before and after irradiation and washing. "DIP" and "W/EG" spots are covered respectively with 10µL of DIP 0.04M solution in water/ethylene glycol 40:60 and with 10 µL of water/ethylene glycol 40:60. "Ref" spots aren't covered with any solution during the irradiation and aren't washed after irradiation.

As Figure 6 shows, the $CaCO_3$ spot covered with the DIP solution, called "DIP", completely dissolves after 15 minutes of irradiation and washing. The "W/EG" spot, covered with water/ethylene glycol and washed after irradiation, does not disappear completely, but it is just partially removed by water washing. The comparison between "DIP" and "W/EG" sample confirms that the $CaCO_3$ removal after the irradiation of the photoacid generator is due to $CaCO_3$ dissolution and not to water washing. The process of dissolution of calcium carbonate has also been observed

with optical microscopy, during a 20-minute irradiation (Figure 7). The longer experiment time is due to the microscope setup, in which the LED is not placed perpendicularly on the spot.

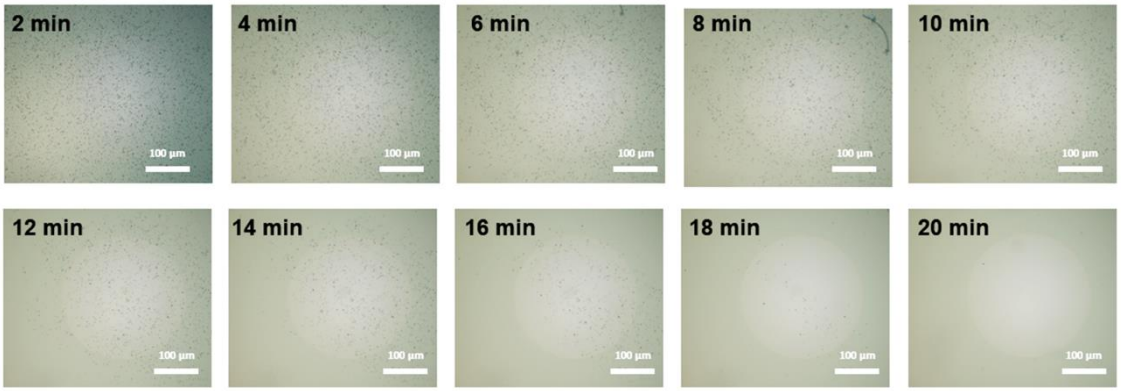

Figure 7: images of calcium carbonate spot with DIP solution on top, during a 20-minute irradiation.

In Figure 7 the process of calcium carbonate dissolution is evident. After 20 minutes of irradiation, calcium carbonate is completely dissolved, thanks to the photo-induced pH drop.

Even if the process has been considerably fastened and the setup optimized, it is still too time consuming for a real application because the potential efficiency of the photoacid is not totally exploited. For the reasons explained above, going to lower irradiation wavelengths would not be an improvement, but it would lead to new drawbacks. Another way to overcome this problem is to activate the photoacid by means of a photosensitizer which absorb in the wavelength range of interest, thus almost above 350 nm.

Thioxanthene-9-one (Thioxanthone) was used as sensitizer because it has an absorption band with a maximum at almost 380 nm, and thus in the range of interest. Furthermore, Thioxanthone is known to give an electron transfer from its triplet state to onium salts[37-39].

Sensitization process of DIP by Thioxanthone was evaluated in a water/ethanol 1:1 mixture. First, as a reference, a DIP solution was irradiated at 280 nm. Then, the solution of DIP and Thioxanthone was irradiated at the wavelength corresponding to the absorption maximum of Thioxanthone, 385 nm. Absorption spectra of the two systems were collected before and after the whole irradiation process (Figure 8).

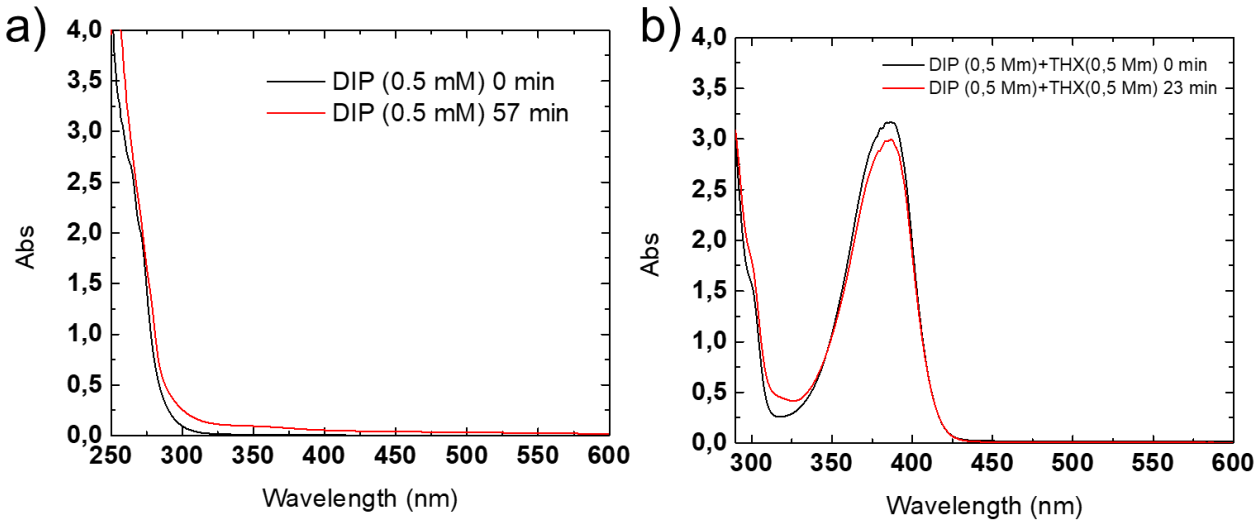

Figure 8: a) Absorption spectra of DIP 0.5 mM in water/ethanol 1:1 before (black) and after (red) irradiation at 280 nm. b) Absorption spectra of DIP 0.5 mM and Thioxanthen-9-one 0.5 mM in water/ethanol 1:1 before (black) and after (red) irradiation at 385 nm.

As Figure 8 shows, the absorption peak of Thioxanthone goes from almost 350 nm to 410 nm and the absorbance is very high between 360 and 400 nm; these characteristics make it a very suitable sensitizer for irradiation between 365 and 395 nm, thus in the near-visible/visible range.
pH was also monitored during the irradiation process, to compare the pH decrease caused by direct excitation of DIP and by sensitization of DIP by thioxanthone (Figure 9).

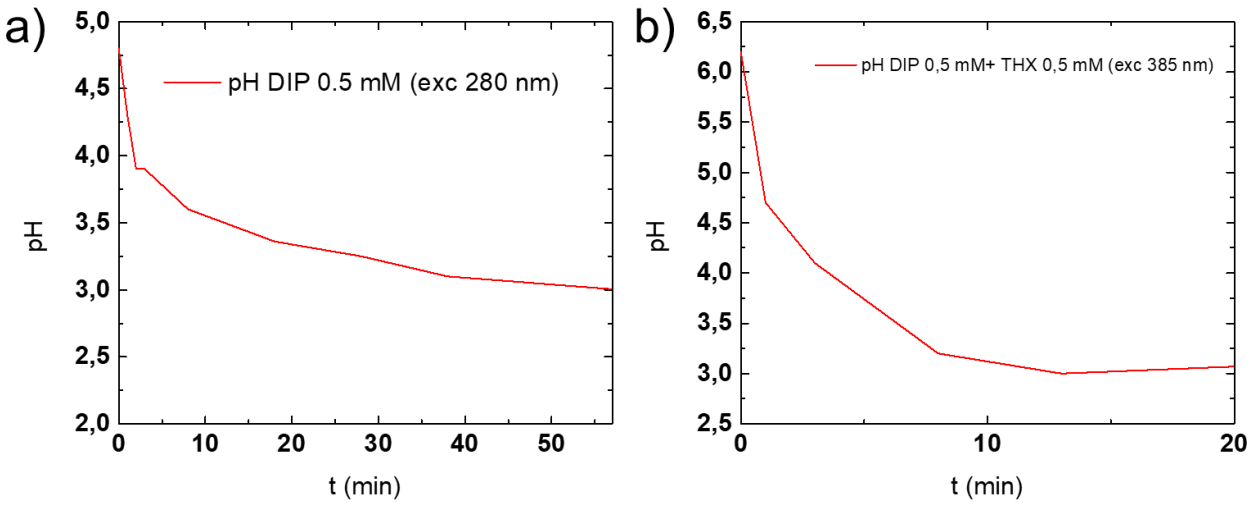

Figure 9: a) pH trend of DIP 0.5 mM during irradiation at 280 nm. b) pH trend of DIP 0.5 mM and Thioxanthone (THX) 0.5 mM during irradiation at 385 nm.

Figure 9 shows a huge difference in the behaviour of direct excitation and sensitization of DIP. In the former (left), pH value of 3 is reached after almost one hour, while in the latter (right) after only 20 minutes. It is important to notice that in DIP solution pH decrease is slower and the final pH value is higher with respect to the one that is usually seen in previous $CaCO_3$ dissolution tests. That is because here the DIP concentration is 0.5 mM, while in the $CaCO_3$ dissolution test it is 20 mM. In this measurement, performed in a 1 cm cuvette, it is important not to work at too high concentration to avoid inner filter effect. In tests performed on $CaCO_3$ spot, inner filter effect is negligible because one drop of solution (almost 1 mm thickness) is irradiated. DIP degradation in these conditions is further confirmed by mass spectrometry (GC-MS) that detects the presence of Iodobenzene in the mixture after irradiation (Figure 10).

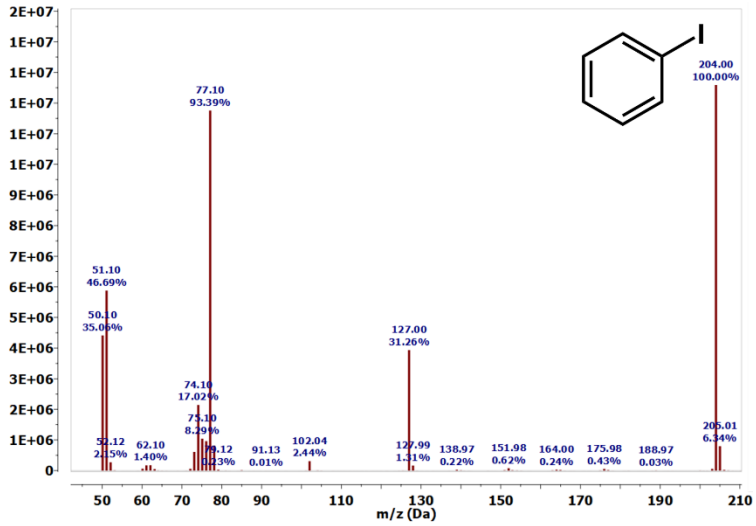

Figure 10: mass spectrum (GC-MS) of irradiated DIP 20 mM and Thioxanthone 0.5 mM solution. Mass spectrum represents Iodobenzene, and corresponds to retention time 5.9 min.

Mass spectrum collected after irradiation shows Iodobenzene, corresponding to a retention time of 5.9 min. No peak referring to unreacted DIP is noticed this time. As already mentioned, the sensitization mechanism between Thioxanthone and onium salts usually is an electron transfer from Thioxanthone to the onium salt, thus we can hypothesize the same kind of mechanism between Thixanthone and DIP. Nevertheless, further investigation on the photosensitization mechanism need to be performed.

After the evaluation of DIP sensitization by Thioxanthone and of the huge contribute to solution acidification, tests were performed on $CaCO_3$ spot. A water/ethylene glycol/ethanol solution of DIP and Thioxanthene-2-one was used; ethanol is also present to allow thioxanthone solubility. The $CaCO_3$ spot on the glass slide was irradiated by LED at 365 nm and 395 nm. Since localization

is very important to allow precise control of the $CaCO_3$ dissolution, this time the LED was further focused. This has been possible using a fluorescence microscope for the process, focusing the LED by means of the microscope and objective lens (Figure 1). This setup also allowed to follow the process by a camera. After irradiation, the system can be efficiently washed with MilliQ water and no traces of DIP solution or $CaCO_3$ spot remains on the glass slide (Figure 11).

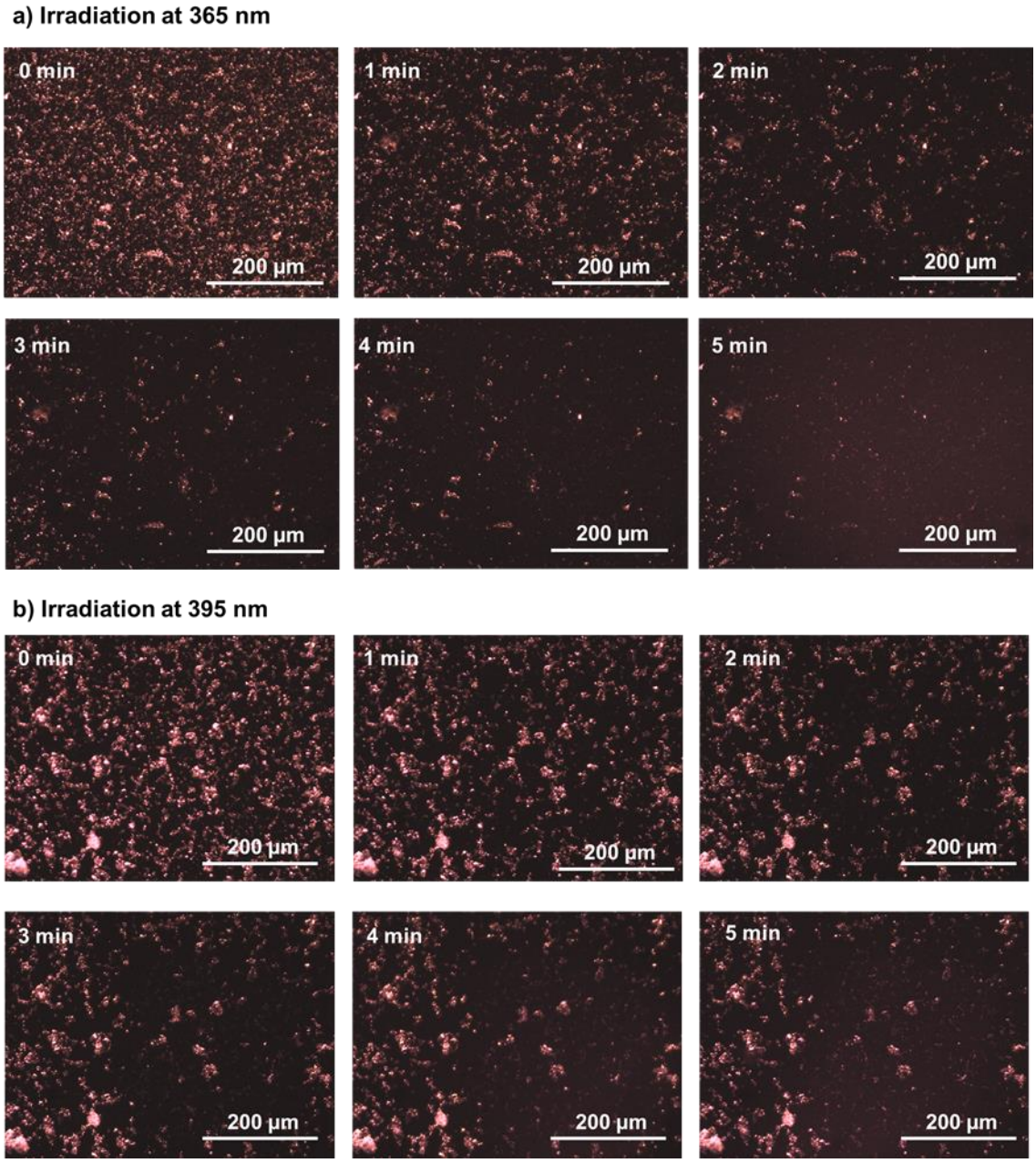

Figure 11: Irradiation at 365 nm (a) and at 395 nm (b): images collected by the camera every minute during irradiation of a $CaCO_3$ spot with DIP and Tioxanthen-9-one solution on top.

The presence of the sensitizer and the irradiation conditions gave very promising results: $CaCO_3$ is almost completely dissolved after 5 minutes of illumination and the dissolution occurs in a defined spot of 1mm of diameter (Figure 12).

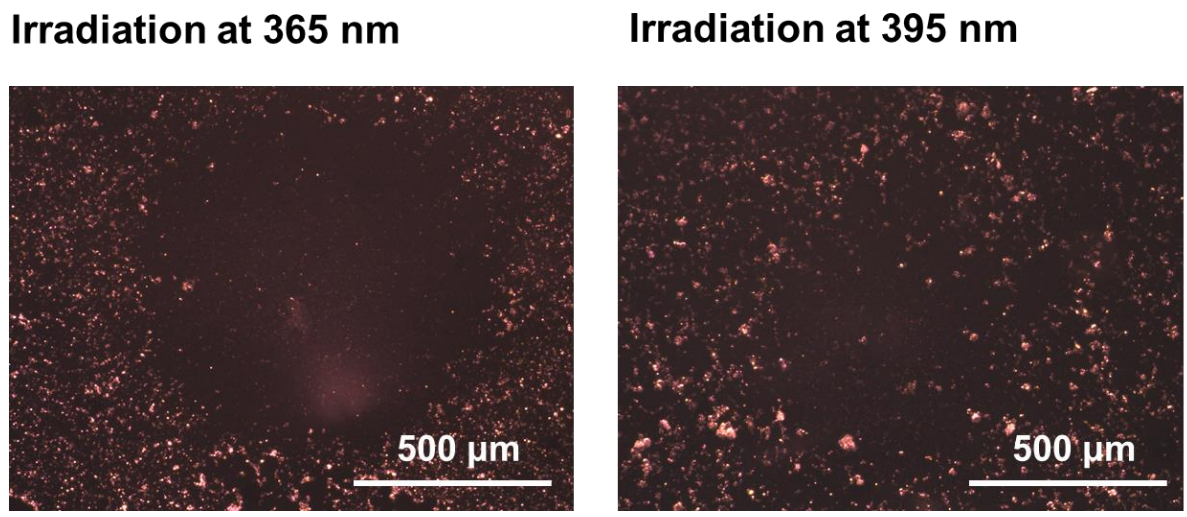

Figure 12: image of the spot generated by 5 minutes of irradiation at 365 nm and at 395 nm

This happens for both the wavelengths 365 nm and 395 nm, allowing the possibility to tune the irradiation not only to the UVA region but also to the visible wavelength range with a high efficiency. Indeed, without the sensitizer, the light-induced dissolution process would last 15 minutes with a 365 nm source and would not occur at all with a 395 nm source.

Finally, tests have also been performed exactly reproducing a final application setup. A 365 nm LED torch was used to irradiate a calcite layer deposited on a glass slide and a lens was used to better focus the light in almost 5 mm of diameter. The calcite layer was irradiated for 5 minutes in these conditions and, after washing with MilliQ water to remove the active solution, a defined spot of dissolved calcite is clearly observed corresponding to the illuminated area (Figure 13).

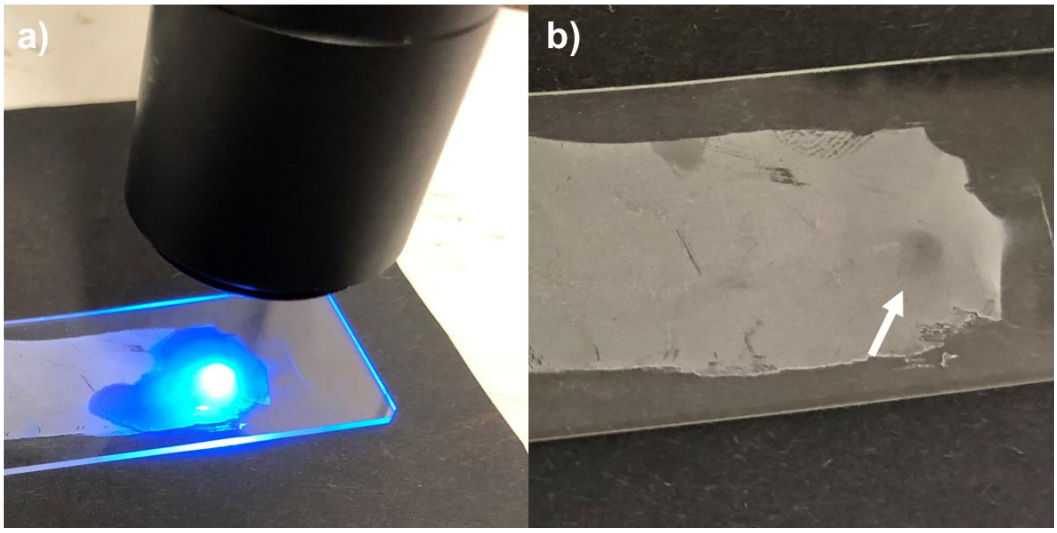

Figure 13: a) irradiation of a calcite layer deposited on glass surface with DIP + Thioxanthone solution on top, by a 365 nm LED torch. b) Calcite layer after an irradiation of 5 minutes and washing with MilliQ water.

The setup reported in Figure 13 represents a model for photoinduced precise $CaCO_3$ dissolution for frescoes restoration. With this method the operator can easily move from one area to another, based on the necessity of cleaning. Furthermore, the use of a phosphorescent sensitizer allows to clearly see the area that is going to dissolve and thus have an even more precision in the cleaning process.

2.2.3. Conclusions

A new method was developed for a precise and not invasive artworks and in particular frescoes restoration. Frescoes are usually very delicate artworks often subjected to unwanted modifications by external agents, thus a restoration method that does not alter frescoes condition with other materials would be very advantageous. Since the main component of these artworks is calcium carbonate, a cleaning method based on its localized dissolution has been developed. A photoacid generator (Diphenyl iodonium hexafluorophosphate) has been used to induce a pH decrease by light, in order to promote $CaCO_3$ dissolution. In this cleaning method, no polymers or resins are involved, but only the main component of the fresco. Furthermore, also the use of organic solvents is avoided since the process is undergone in water-based solution. For these reasons, side effects that could damage the artwork are limited and the active solution can also be easily cleaned by water after the treatment. The use of a localized light source allows to have a very high precision in the restoration process. The technique was further improved by photosensitized activation of the photoacid generator by thioxanthone. Having a sensitizer gave great enhancement to the process rate, leading to an even more real applicability of the method,

also adding the advantages of a real time monitoring of the process, thanks to Thioxanthone phosphorescence, and to safer conditions for the operator, thanks to a less harmful illumination. Beyond the artwork restoration application, using a photoacid to control the dissolution of calcium carbonate can have many other applications (i.e. lithography) and it is a phenomenon that surely needs deeper investigation, also in order to make it applicable to other kinds of materials and using other kinds of photoactive molecules.

2.3. Photoprecipitation of Calcium Carbonate by means of a Photobase generator

2.3.1. Materials

Irradiation sources

- LED (2.2 mmx2.2 mm light emitting surface) purchased by LED engine. The irradiation wavelength is 365 nm with a radiant flux of 3.3 W (Forward current 700 mA) at 25°C. The LED has a viewing angle (the off-axis angle from the centreline where the radiometric power is the 50% of the peak value) of 110°.
- LED (6.4 mm ø) purchased by Mouser Electronics. The irradiation wavelength is 395 nm with a radiant flux of 3 W (Forward current 700 mA) at 25°C. The LED has a viewing angle (the off-axis angle from the centreline where the radiometric power is the 50% of the peak value) of 45°.
- Spectrofluorimeter Horiba Fluoromax 4 was used for irradiation in the study of sensitization of Diphenyliodonium hexafluorophosphate by Thioxanthene-9-one.

Characterization of Ketoprofen and organic byproducts

Absorption spectroscopy

Absorption spectra were performed by means of a UV-Vis spectrophotometer (Perkin Elmer Lambda 650) on Ketoprofen 0.2 mM in water/ethanol mixture before and after LED irradiation for two hours.

Mass spectrometry

Electronic impact mass spectrometry (GC-MS) was performed on Ketoprofen 6 mM solution in water/ethanol 1:1 mixture after 1 hour of irradiation.

PH measurements

PH measurements were performed by means of a pH-meter, monitoring the pH of Ketoprofen 6 mM solution in water/ethanol 1:1 mixture during the irradiation

Photoprecipitation tests in solution (Ketoprofen)

Ketoprofen purchased by Sigma Aldrich was used as a photobase generator. Ketoprofen (concentrations from 2 to 20 mM) and $CaCl_2$ (concentrations from 0.2 M to 1 M) were dissolved in a water/ethanol mixture 1:1. The pH was adjusted by the addition of NH_3. Irradiation was performed on 4mL vials (Ø 15mmx45mm) filled with 3 mL of the solution. The LED was placed

horizontally, at 3 cm from the vial. This distance corresponds to an irradiance of 36700 $W \cdot m^{-2}$ on a light spot with 1,1 cm of diameter, measured considering an angular displacement of 20°. The irradiation was performed for one hour. Images at the optical microscope were obtained on a water/ethanol solution of Ketoprofen 10 mM and $CaCl_2$ 20 mM, irradiating with the LED at 365 nm for 5 minutes. Crystals were observed at the optical microscope (Olympus IX71) in back scattering mode, illuminating by a Tungsten lamp.

Characterization of Sodium tetraphenylborate, Thioxanthone and organic byproducts

Absorption spectroscopy

Absorption spectra were performed by means of a UV-Vis spectrophotometer (Perkin Elmer Lambda 650) on Sodium Tetraphenyl borate 0.5 mM and Sodium Tetraphenyl borate 0.5 mM with Thioxanthone 0.5 mM in water/ethanol mixture before and after LED irradiation for two hours.

Mass spectrometry

Electronic impact mass spectrometry (GC-MS) was performed on Sodium tetraphenylborate 2 mM solution in water/ethanol 1:1 mixture after 1 hour of irradiation.

PH measurements

PH measurements were performed by means of a pH-meter, monitoring the pH of TPB (0,5 mM) and TPB with Thioxanthone 0,5 mM solution in water/ethanol 1:1 mixture during the irradiation

Photoprecipitation tests in solution (Sodium tetraphenylborate and Thoxanthone)

TPB dissolved in water/ethanol 1:1 with a concentration of 2 mM and THX solution was prepared in Ethanol with a concentration of 1 mM. A water/ethanol solution 1:1 of $CaCl_2$ 0.05 M was prepared in HCl 0.005M (pH almost 2,5). Then, $NaHCO_3$ was added to have a final concentration of 0.005M (at higher concentration precipitation in dark was observed). Then, TPB and the THX were added to the solution to have a TBP concentration of 2 mM and a THX concentration of 0.05 mM; the pH was adjusted to 7.8 with NaOH. The irradiation of 2 mL of the solution in a glass vial was performed by the 365 nm LED for 5 minutes, at a distance of 3 cm.

Observation at optical microscope

The observation after irradiation of crystals in Ketoprofen and Tetraphenylborate samples was performed in a fluorescence optical microscope (Olympus IX71). The images were collected in backscattering by illuminating one side of the sample with a tungsten lamp, to see the calcite crystals, not clearly observable with the microscope transmission mode.

2.3.2. Results

Photobase generators studied for photoinduced precipitation of Calcium Carbonate have been Ketoprofen and Tetraphenylborate ion (TPB). These two molecules have demonstrated to be both capable to promote the $CaCO_3$ precipitation, even if by means of two different mechanisms: TPB exploits the pH increase while in Ketoprofen the main contribution is given by the decarboxylation process.

Photoinduced precipitation of Calcium Carbonate by Photo generation of CO_2 with Ketoprofen

Ketoprofen is a nonsteroidal anti-inflammatory drug that has been widely investigated for its photosensitivity and thus its potential toxicity[40]. Indeed, ketoprofen carboxylate undergoes a photodecarboxylation and simultaneously also behaves as a photobase generator, under UV light irradiation. Even if Ketoprofen is a benzophenone derivative, the photodegradation mechanism of the carboxylate follows a very fast decarboxylation pathway from the triplet state (lifetime 250 ps), differently from the benzophenone-like behaviour that usually has a long-lived triplet state[41]. The decarboxylation pathway leads also to an increase in pH, thus, in presence of calcium chloride, these two elements favour calcium carbonate precipitation, according to the mechanism reported in Scheme 1.

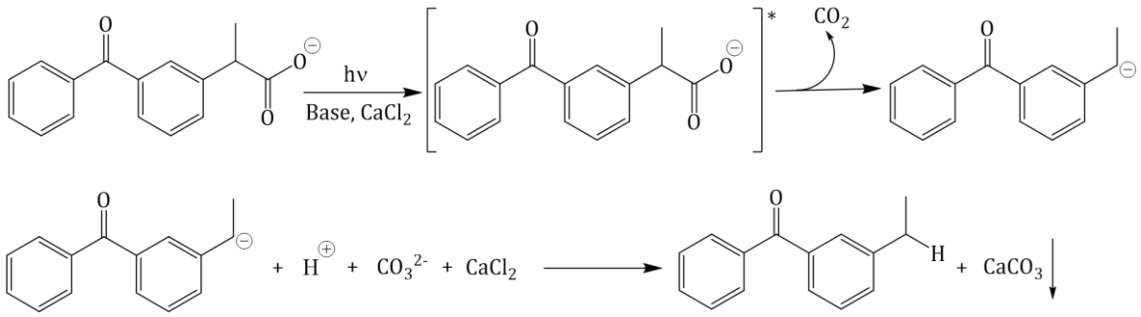

Scheme 1: mechanism of ketoprofen carboxylate degradation in presence of calcium chloride: $CaCO_3$ photoinduced precipitation

As Scheme 1 shows, in principle ketoprofen should act both as a photobase generator and a photo-CO_2 generator in the process of $CaCO_3$ precipitation. However, the photodecarboxylation pathway is favoured for Ketoprofen carboxylate, and, in the range of Ketoprofen concentration used (2 mM-20 mM), the pH value in which it can be almost completely deprotonated is around 9.5-10.5. This

means that, since a more efficient photoprecipitation reaction would happen in an already alkaline environment, the factor that mainly boosts $CaCO_3$ precipitation is the CO_2 generation, rather than the pH increase effect.

First, Ketoprofen behaviour was studied by irradiating it in solution (water/ethanol mixture 1:1, in water only ketoprofen byproducts would precipitate) at alkaline pH, with a LED at 365 nm. The solution was characterized by absorption spectroscopy (Figure 1) and mass spectrometry (Figure 2).

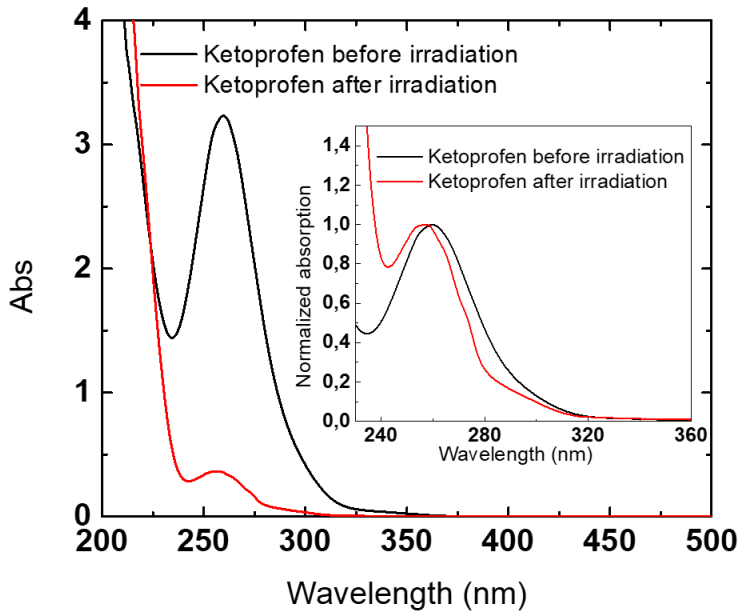

Figure 1: Absorption spectra of Ketoprofen in water/ethanol 1:1, al alkaline pH, before (black) and after (red) an irradiation of 40 minutes. Spectra were collected after a 100-fold dilution of Ketoprofen solution (final concentration 0.2 mM).

Figure 1 shows absorption peak of Ketoprofen before and after irradiation. In particular, even if the irradiation occurs at 365 nm, in correspondence to the tail of Ketoprofen absorption band, it can be clearly seen that a modification of the intensity of the peak occurs during irradiation. A relevant decrease in the absorption intensity of Ketoprofen is noticed, meaning that ketoprofen modification occurred. Furthermore, a less intense peak is present in the absorption spectrum of Ketoprofen after irradiation. Since this peak is slightly hypsochromically shifted with respect to Ketoprofen absorbance (Figure 1- inset), it cannot be attributed only to unreacted ketoprofen but also to ketoprofen byproduct, 3-ethylbenzophenone. Indeed, 3-ethylbenzophenone has an absorption maximum at 254 nm[42], thus we can hypothesize that the absorption peak of Ketoprofen after irradiation can be attributed to the sum of unreacted ketoprofen and 3-ethylbenzophenone, responsible of the increase in pH.

The photolysis process of ketoprofen is further confirmed by GC chromatography mass spectrometry (Figure 2), in which only a peak is observed, corresponding to 3-ethylbenzophenone, the main byproduct of ketoprofen photoinduced decarboxylation, which characterizes its photobase behaviour (Scheme 1).

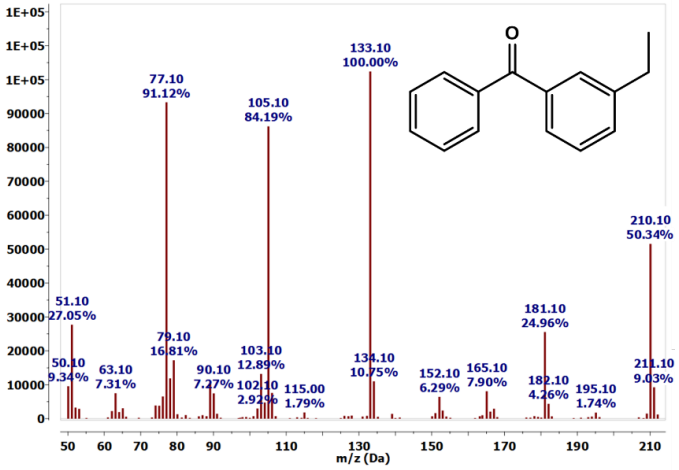

Figure 2: mass spectrum of Ketoprofen solution irradiated for 40 minutes. Peak with retention time at 16.43 min represents 3-ethylbenzophenone.

pH variation was monitored during an irradiation of 40 minutes of Ketoprofen solution in water/ethanol 1:1 mixture starting not in an alkaline environment but from pH 7.5, in order to better evaluate the pH jump associated to Ketoprofen photolysis (Figure 3).

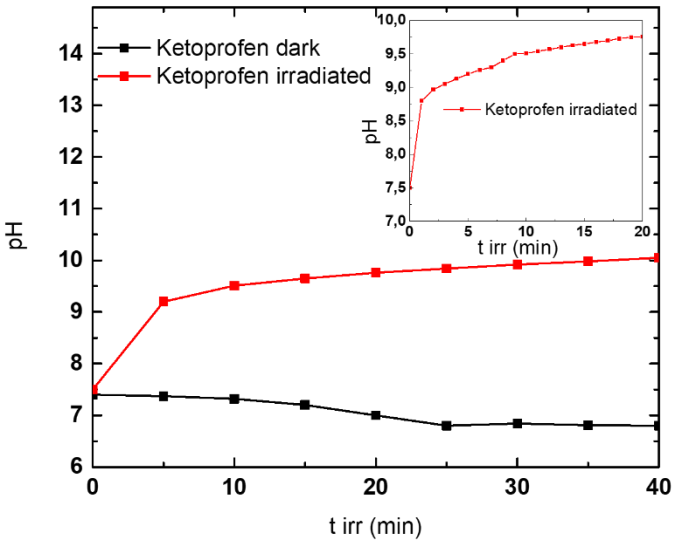

Figure 3: pH variation in Ketoprofen solution at pH 7.5 kept in dark (black) and irradiated (red) for 40 minutes, measuring the pH each 5 minutes. Inset: pH variation of irradiated Ketoprofen in the first 20 minutes measuring the pH every minute.

As Figure 3 shows, there is a significative effect of Ketoprofen degradation process on the jump of pH, which goes from 7.5 to almost 10 after 40 minutes of irradiation. Figure 3 shows also (inset) that there is a very fast jump of almost 1 point of pH in the first minute and then the increase in pH is slower, for this reason at least 40 minutes are necessary to reach a sufficiently alkaline pH value for $CaCO_3$ precipitation. As shown in Figure 3, even at neutral pH, the photodecarboxylation process occurs and pH increases. Nevertheless, even if Ketoprofen acts as a photobase generator, the contribution of the generation of CO_2 on the pH cannot be neglected. The pH trend in Figure 3 has been obtained by irradiating the ketoprofen solution in an open vial, to verify the pH variation mainly associated to the hydrogen abstraction by the 3-ethyl benzophenone moiety rather than to the generation of CO_2. However, the presence of CO_2 is essential to obtain an efficient $CaCO_3$ precipitation, thus it is necessary to have it in solution. In order to estimate its effect on the overall pH, monitoring was performed also irradiating ketoprofen solution in a closed vial, opening it only to measure pH (Figure 4).

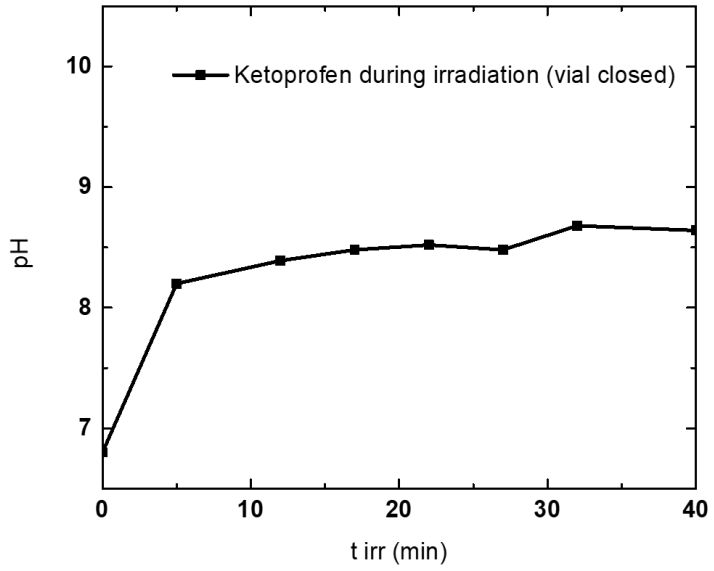

Figure 4: pH jump during irradiation of Ketoprofen solution in water/ethanol 1:1 in a closed vial

As expected, in the closed vial and thus in presence of more photogenerated CO_2, the pH increase is less pronounced and after 40 minutes of irradiation, starting from pH almost 7, pH increases only until almost 8.5, a value that could not lead to $CaCO_3$ precipitation in these conditions.
Photoprecipitation tests starting from neutral pH were performed by irradiating for 40 minutes a Ketoprofen 6 mM and $CaCl_2$ 1 M solution in water/ethanol 1:1, starting from a pH of 7-7.5 (Figure 5).

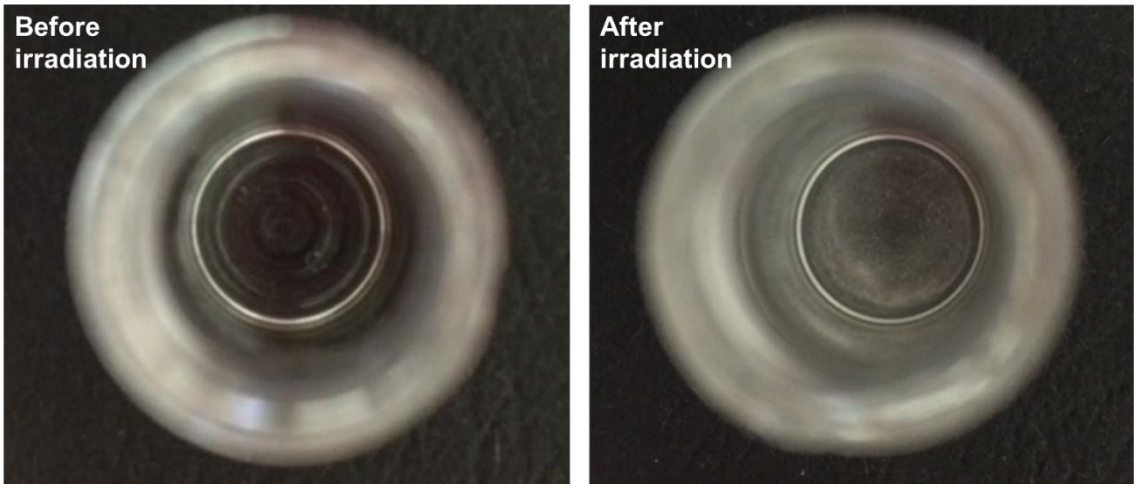

Figure 5: Ketoprofen 6 mM and $CaCl_2$ 0.1 M in water/ethanol mixture starting from pH 7.3 before (left) and after (right) an irradiation of 40 minutes.

Figure 5 shows the bottom of the vials before and after irradiation. Some precipitate can be noticed at the bottom of the vial but in a very little quantity. Ketoprofen and $CaCl_2$ concentrations have also been tuned but the precipitation was not efficient enough. This outcome can be due to several events that happen once the irradiation begins. The base and CO_2 generation initially boosts the formation of CO_3^{2-} ion, which also decreases the quantity of CO_2 in solution, maintaining the pH sufficiently high to induce some precipitation. However, when $CaCO_3$ precipitation occurs, it gives another contribution to pH decrease, that, coupled with further CO_2 formation during irradiation, stops $CaCO_3$ precipitation. Indeed, the pH value measured after the irradiation of Ketoprofen and $CaCl_2$ is 6, a value even lower than the initial one (7.5). For this reason and for the higher reactivity of de-protonated Ketoprofen, the best condition in which the photoinduced precipitation of $CaCO_3$ can occur is in alkaline environment.

Photoinduced precipitation of calcium carbonate was obtained by irradiating a water/ethanol solution of Ketoprofen for 30-40 minutes, depending on the experimental conditions (LED-sample distance and Ketoprofen concentration), in presence of $CaCl_2$. The system was irradiated at several $CaCl_2$ concentrations ranging from 0.1M to 1 M and at several pH values ranging from 10.5 to 11.5 and photoinduced precipitation of $CaCO_3$ always occurs (Figure 6).

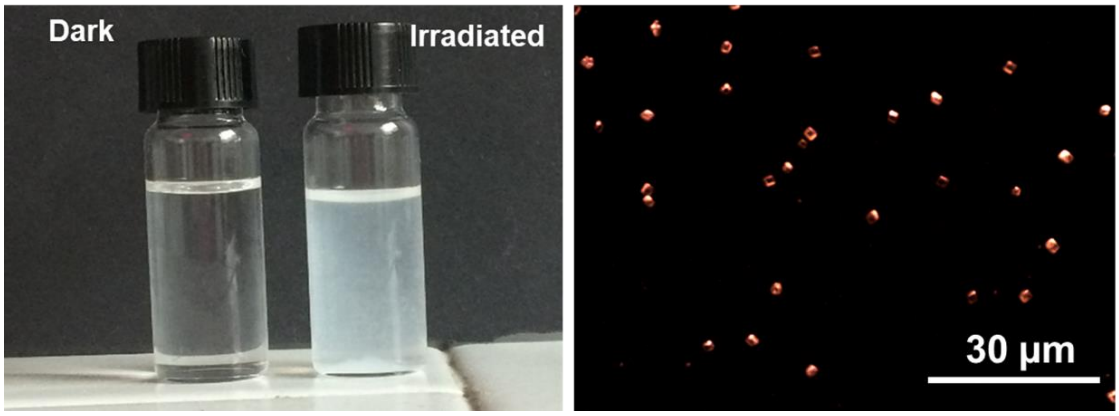

Figure 6: Ketoprofen and $CaCl_2$ in water/ethanol left in dark and irradiated at 365 nm for 30 minutes (left) at pH 11.5. Right- irradiated solution of Ketoprofen and $CaCl_2$ observed at the optical microscope.

Figure 6 (right) shows calcite crystals forming after irradiation of Ketoprofen and $CaCl_2$ solution. In general, as $CaCl_2$ concentration and pH increase, photoinduced precipitation is more efficient. Nevertheless, precipitation in dark also starts to occur. Tuning these parameters, it is possible to find the most performing photoprecipitation conditions and avoid the precipitation in dark.

Photoinduced precipitation of Calcium Carbonate by Sodium Tetraphenyl Borate (TPB) as a Photobase generator

Sodium tetraphenyl borate is a photobase generator which is used in organic synthesis, photocatalysis and transition metal chemistry[43]. In particular, it undergoes photolysis under UV light that leads to the abstraction of a proton. Therefore, here the $CaCO_3$ precipitation is just caused by the increase in pH. The photodegradation mechanism[44] is reported in Scheme 2.

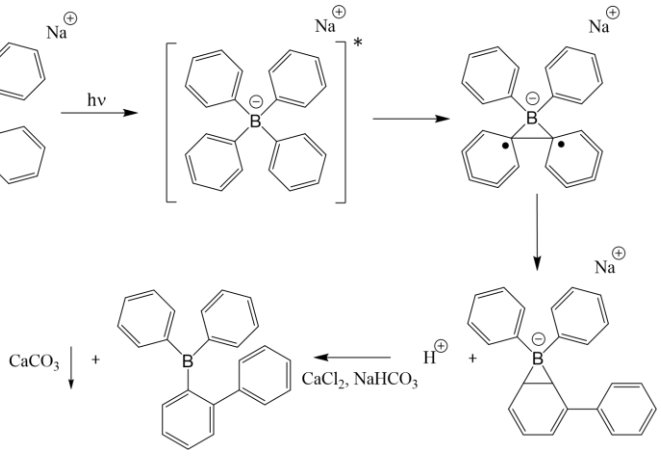

Scheme 2: Photoinduced precipitation of calcium carbonate by means of sodium tetraphenylborate.

Sodium Tetraphenylborate (TPB) is usually activated irradiating with 254 nm sources. Since TPB has not any absorbance in the Near-UV and especially at the irradiation wavelength used already to activate ketoprofen (365 nm), sensitization by means of Thioxanthone was performed. Indeed, Thioxanthone is often used as a sensitizer for TPB and sensitization mechanism is an electron transfer from TPB to Thioxanthone[45]. Sensitization process of TPB by Thioxanthone was evaluated in a water/ethanol 1:1 mixture. First, as a reference, a TPB solution was irradiated at 280 nm. Then, the solution of TPB and Thioxanthone was irradiated at the wavelength corresponding to the absorption maximum of Thioxanthone, 385 nm. Absorption spectra of the two systems were collected before and after the whole irradiation process (Figure 7).

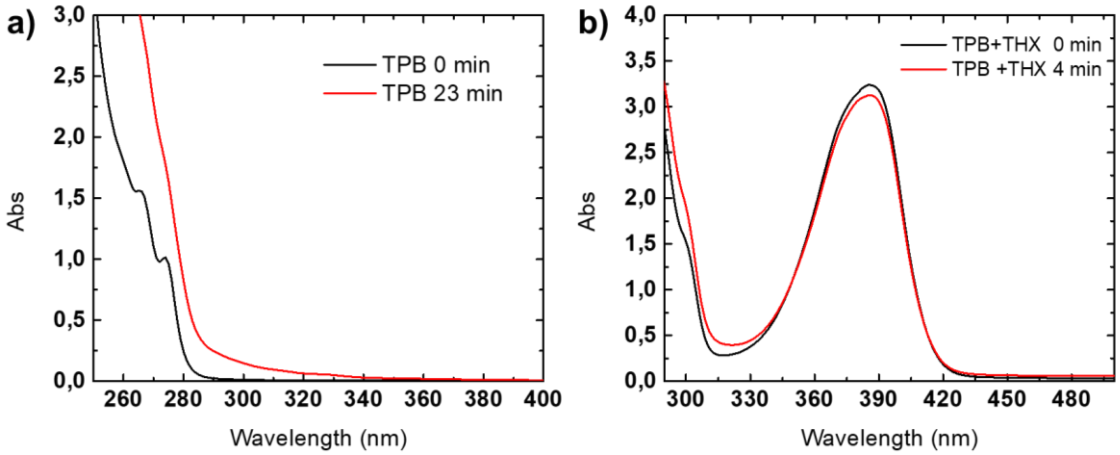

Figure 7: a) Absorption spectra of DIP 0.5 mM in water/ethanol 1:1 before (black) and after (red) irradiation at 280 nm. b) Absorption spectra of DIP 0.5 mM and Thioxanthen-9-one 0.5 mM in water/ethanol 1:1 before (black) and after (red) irradiation at 385 nm.

As Figure 7 shows, the absorption peak of Thioxanthone goes from almost 350 nm to 410 nm and the absorbance is very high between 360 and 400 nm; these characteristics make it a very suitable sensitizer for irradiation between 365 and 395 nm, thus in the near-visible/visible range.
pH was also monitored during the irradiation process, to compare the pH decrease caused by direct excitation of TPB and by sensitization of TPB by thioxanthone (Figure 8).

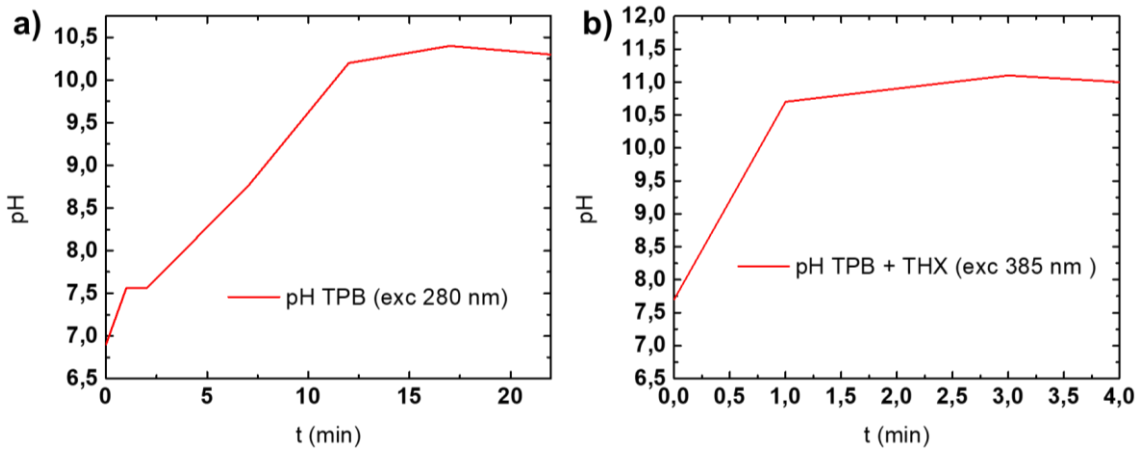

Figure 8: a) pH trend of TPB 0.5 mM during irradiation at 280 nm. b) pH trend of TPB 0.5 mM and Thioxanthone (THX) 0.5 mM during irradiation at 385 nm.

As Figure 8 shows, sensitization significatively improves pH increase rate. Indeed, in TPB and Thioxanthone mixture, a pH value of almost 11 is reached after just 4 minutes, time scale which is highly suitable for the final application in artwork restoration. The process was also confirmed by GC-MS spectrometry (Figure 9), in which both in the irradiated TPB and TPB with Thioxanthone solutions a Biphenyl is detected, which is one of the main byproducts of TPB photodegradation.

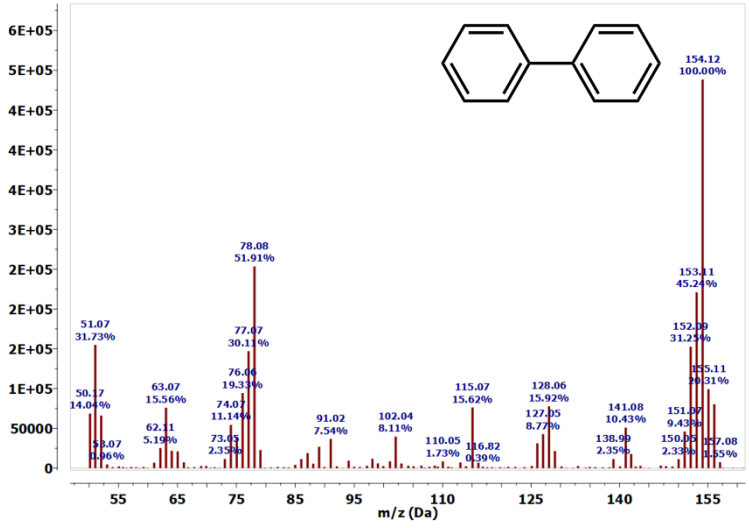

Figure 9: Mass spectrometry (GC-MS) of Biphenyl, reported in both irradiated TPB and TPB+Thioxanthone solutions, in correspondence of a retention time of almost 11.5 minutes.

After having verified the sensitized photodegradation process, tests for calcium carbonate precipitation starting from neutral pH were performed. Since the photoinduced degradation of TPB leads just to an increase in pH, a CO_3^{2-} is also needed in the solution. Indeed, trials were first

performed by just considering reaction of atmospheric CO_2, but it was not possible to obtain any significative precipitation. Thus, $NaHCO_3$, coupled with $CaCl_2$ were the sources respectively of CO_3^{2-} and Ca^{2+} ions. The solution was then irradiated, starting from pH almost 7.5-8 for 5 minutes. After irradiation, a turbidity in the solution was noticed that corresponds to $CaCO_3$ precipitation (Figure 10).

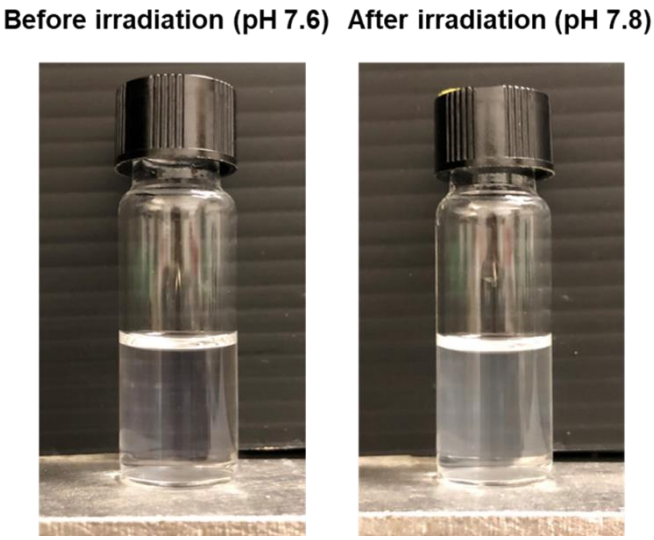

Figure 10: TPB and Thioxanthone solution before and after irradiation, in presence of $CaCl_2$ and $NaHCO_3$.

In absence of $CaCl_2$ and $NaHCO_3$, the TPB 2mM and THX 0.05 mM solution has a pH value which goes from 8 to 12 in 5 minutes of irradiation, thus the little increase of pH showed in Figure 10 is due to $CaCO_3$ precipitation. This sample was also observed at the optical microscope in order to better monitor the $CaCO_3$ formation. Dark sample was observed after having kept it in dark for one hour; irradiated samples were observed one hour after the 5 minute-irradiation (Figure 11).

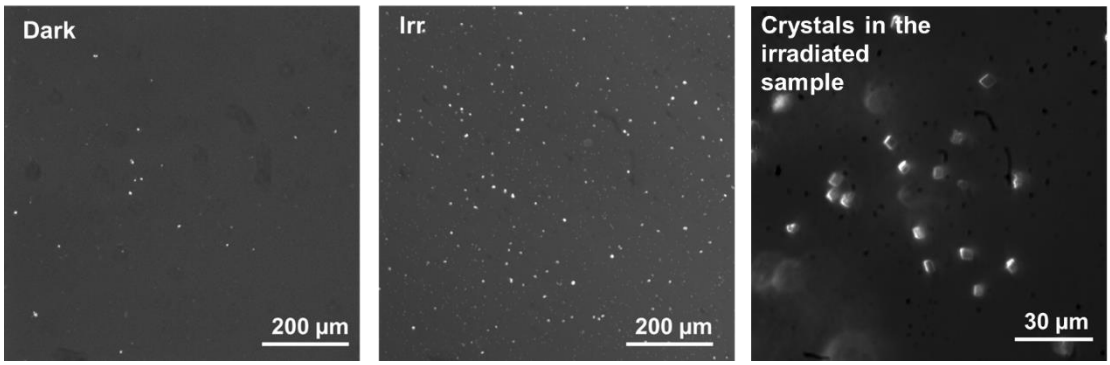

Figure 11: Photoinduced precipitation of $CaCO_3$ in presence of TPB and Thioxanthone. Sample left in dark ("dark") and irradiated ("Irr"). Detail of calcite crystals formed in the irradiated sample (right).

Many calcite-shape crystals appeared in the irradiated sample, while very few of them were observed in the dark sample, demonstrating again the photo-controlled precipitation of the crystals.

Irradiation of Sodium Tetraphenylborate sensitized by Thioxanthone allows to have a very fast jump in pH in very few minutes. Nevertheless, there is not a high quantity of $CaCO_3$ in these conditions and crystals start to appear not immediately after irradiation but after some time. This problem could be solved by having a higher concentration of precursor ions and/or a different medium, in order to more easily obtain a lower supersaturation limit at the pH that is reached with light.

2.3.3. Conclusions

As already mentioned in the previous sections, frescoes are very delicate artworks that can more easily have the necessity to be restored. For these reasons, it is important not to use too invasive methods that could lead to big damages. On the contrary, restoring frescoes by using its main component material, $CaCO_3$, is certainly a noticeable improvement. As $CaCO_3$ photoinduced dissolution can be used to clean frescoes, $CaCO_3$ photoinduced precipitation can be used for consolidation, by repairing fragile parts of the oeuvre with carbonate and avoiding polymers/resins.

Photobase generator have been used to induce a pH increase by light, in order to precipitate $CaCO_3$. Also in this case, the process is conducted in water based solutions, avoiding the use of organic solvents and it can be controlled locally, by using a not harmful irradiation light (365 nm). In particular, two photobase generators were exploited for this purpose: Ketoprofen and Sodium Tetraphenylborate. The former promotes $CaCO_3$ formation mainly by means of CO_2 release and the latter by means of a pH jump.

Furthermore, sensitization of Sodium Tetraphenylborate by Thioxanthone was investigated and the photoinduced precipitation can be achieved with just 5 minutes of irradiation by a 365 nm source. In order to make this method closer to the real application in artworks restoration it is necessary to precipitate a higher quantity of Calcium Carbonate. This can be achieved for example by tuning concentration of the reactants and pH conditions. Further studies will be performed with this aim and other photoactive molecules and sensitizer will be studied to improve the process in future. However, controlling the crystallization of a material with light can already be really interesting for other applications, such as lithography, and also to study in detail crystallization processes.

2.4. Photoinduced crystallization of Calcium Carbonate embedded in a gel

2.4.1. Materials

Irradiation sources

- LED (2.2 mmx2.2 mm light emitting surface) purchased by Mouser electronics with an irradiation wavelength of 365 nm with a radiant flux of 3.3 W (Forward current 700 mA) at 25°C. It has a viewing angle (the off-axis angle from the centreline where the radiometric power is the 50% of the peak value) of 110°
- Hg lamp (Sylvania F8T5/BLB – Camag) that emits at 366 nm and has 8W of power
- A pulsed Nd:YAG laser. The laser was used at 355 nm, irradiation was performed at 30 mJ, with 100 shots at 95 μs for each pulse.

Gel preparation

Agarose (20 mg/mL) is added to a sucrose (Sigma Aldrich) 60% w/v aqueous solution. The system is heated at 85°C to dissolve agarose. The hot solution is left cooling in between two glass slides to obtain a very smooth and uniform gel with a thickness of 1 mm. $CaCl_2$ has been embedded in the gel with two methods: the gel can be stored in a $CaCl_2$ aqueous solution 20 mM for 1 hour or $CaCl_2$ 20 mM can be added in the gel preparation solution. With the second method a better uniformity of the precipitated crystals is obtained. The irradiation performed by the UV lamp was performed by putting the lamp on top of a vial with the gel merged in 350 μL of Ketoprofen solution at 5 cm of distance. The irradiation lasted 10 minutes.

Photoprecipitation of Calcium carbonate embedded in a gel (lamp irradiation)

The irradiation with the lamp at 366 nm was performed on top of a vial with the gel ($CaCl_2$ 20 mM) merged in 350 μL of Ketoprofen 20 mM, 10 mM, 5 mM and 2 mM solution and lasted 10 minutes Crystals were observed with polarization microscopy (Zeiss Axioimager in reflected light mode) and SEM/EDX (Hitachi TM3000).

Photoprecipitation of Calcium carbonate embedded in a gel (laser irradiation)

The irradiation performed with the laser was performed on top of a vial with the gel ($CaCl_2$ 20 mM) merged in 350 μL of Ketoprofen 2 mM solution and lasted 10 seconds (100 shots, 95μs each

shot). Crystals were observed with polarization microscopy (Zeiss Axioimager in reflected light mode) and SEM/EDX (Hitachi TM3000).

Photoprecipitation of Calcium carbonate embedded in a gel (LED irradiation in the fluorescence microscope)

Irradiation and crystals observation were performed also with a fluorescence optical microscope (Olympus IX71) adapted for irradiation (Figure 1). The LED source at 365 nm was placed in correspondence to the light source of the fluorescence microscope and no filter in excitation was set up. Irradiation was performed with a 10x or a 20x objective. After irradiation, images were collected in backscattering by illuminating one side of the sample with a tungsten lamp, to see the calcite crystals, not clearly observable with the microscope transmission or fluorescence mode.

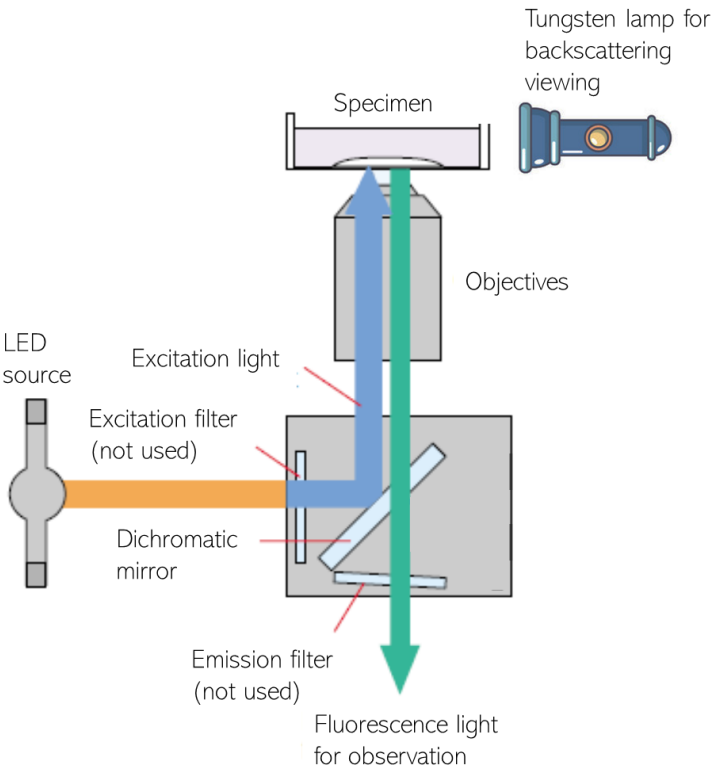

Figure 1: Irradiation setup in the fluorescence microscope (readapted from Olympus IX71 manual)

2.4.2. Results

Once it was verified that calcium carbonate could be precipitated by a light induced process in solution, there was the necessity to embed the precipitate on a support, to write fixed structures with light. An agarose hydrogel was chosen as the most proper matrix to fix the calcium carbonate

crystals since agarose is transparent to UV light and thus it does not interfere with the light-induced process. In addition, scattering effects due to agarose gel turbidity were avoided by adding sucrose (Figure 2) which reduces the degree of gel helix aggregation and leads to a matching of the refractive indexes[46].

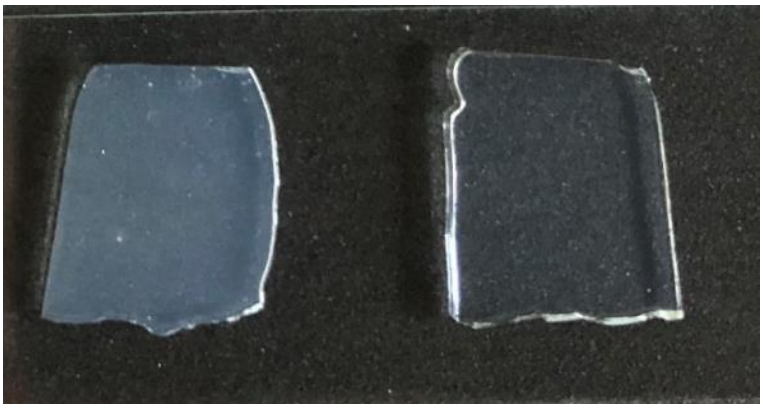

Figure 2: agarose gel (right) and agarose gel modified by sucrose (left). A very smooth and uniform gel is obtained. Modification of the gel with sucrose lead to a higher transparency.

Low thickness (1 mm) and high transparency of the gel are important features to obtain an efficient and uniform crystallization. Having a low thickness means reducing the optical path that, together with concentration, enhances the absorption intensity (according to Lambert-Beer law), thus Ketoprofen reactivity. These features allow to use a 365 nm light to excite ketoprofen with sufficient efficiency for the crystallization process, even if that wavelength overlaps just with the tail of the absorption band of Ketoprofen. The gel, in which $CaCl_2$ is previously embedded, is merged in an aqueous solution of Ketoprofen in alkaline pH and the whole system can be then irradiated at 365 nm (Figure 3).

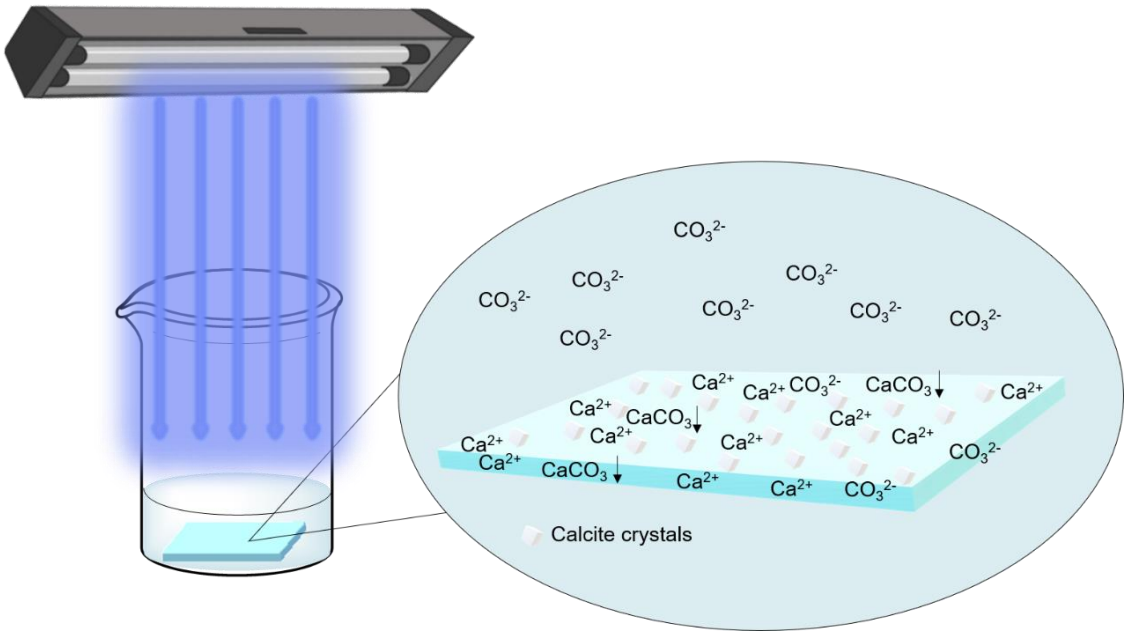

Figure 3: crystallization mechanism of calcium carbonate after UV light irradiation of agarose gel, in which Ca^{2+} ions are embedded, merged in aqueous solution of Ketoprofen at pH 10.3.

UV light irradiation induces ketoprofen decarboxylation (Scheme 1 in section 2.3.2), generating CO_2 that, in presence of alkaline pH, is converted to CO_3^{2-}. Carbonate ions can thus migrate on the surface and through the gel and, by encountering Ca^{2+} ions, trigger $CaCO_3$ precipitation. The pH value, which depends on $CaCl_2$ and Ketoprofen concentration and ranges from 10.3 to 10.6, allows to have the precipitation of calcium carbonate selectively under light irradiation and avoid precipitation in dark, which happens in the case of a higher pH, because of CO_2 in air. A lower pH does not allow enough precipitation under light irradiation. Having ketoprofen only in solution and Ca^{2+} ions in the gel helps crystallization process and uniform crystals distribution. Indeed, diffusion plays an important role in the $CaCO_3$ precipitation and if the whole process in carried on inside the gel matrix, the lack of diffusion leads to less precipitation. Furthermore, Ketoprofen byproduct precipitates inside the gel, further contrasting the crystallization process and leading to a lack of uniformity in crystals distribution. On the contrary, in a double system made by the gel and the solution, the decarboxylation reaction and the ketoprofen byproduct precipitation take place mostly in solution, enhancing the precipitation efficiency and uniformity by the higher diffusion and lack of organic byproduct in the gel. In addition, it is possible to easy clean the final gel from the organic byproducts without a real washing step but just removing the solution in which the gel is merged right after irradiation. After 10 minutes of irradiation, a lot of calcium carbonate crystals form through all the gel, while in dark almost no precipitation is noticed, as polarization microscopy and SEM show (Figure 4).

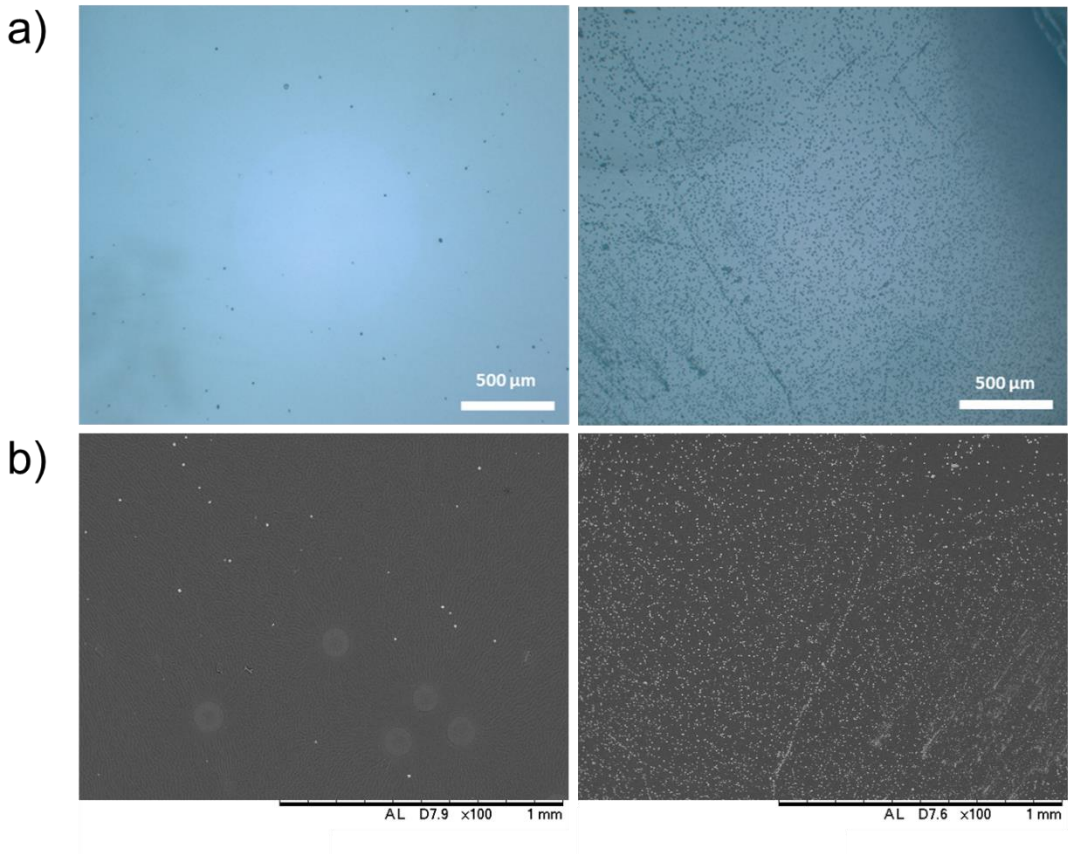

Figure 4: a) polarization microscopy images of agarose-sucrose gel, previously stored in $CaCl_2$ 20 mM, after having been covered with ketoprofen aqueous solution 20 mM at pH 10.6, left 10 minutes in dark (left) and under a UV Hg lamp (366 nm) irradiation (right). b) SEM images of the same gels, in dark (left) and irradiated (right).

Figure 4 shows the light-controlled precipitation of calcium carbonate on the surface of the gel. Polarization light microscopy shows also that crystals are present through all the gel thickness and thus confirms that the transparency of the gel allows the light to penetrate in all the volume of the solution and that the carboxylic moiety released from Ketoprofen manage to migrate inside the gel. SEM and EDX confirmed $CaCO_3$ crystallization after irradiation. Calcite crystals are usually obtained, even if in some cases also vaterite was noticed (Figure 5).

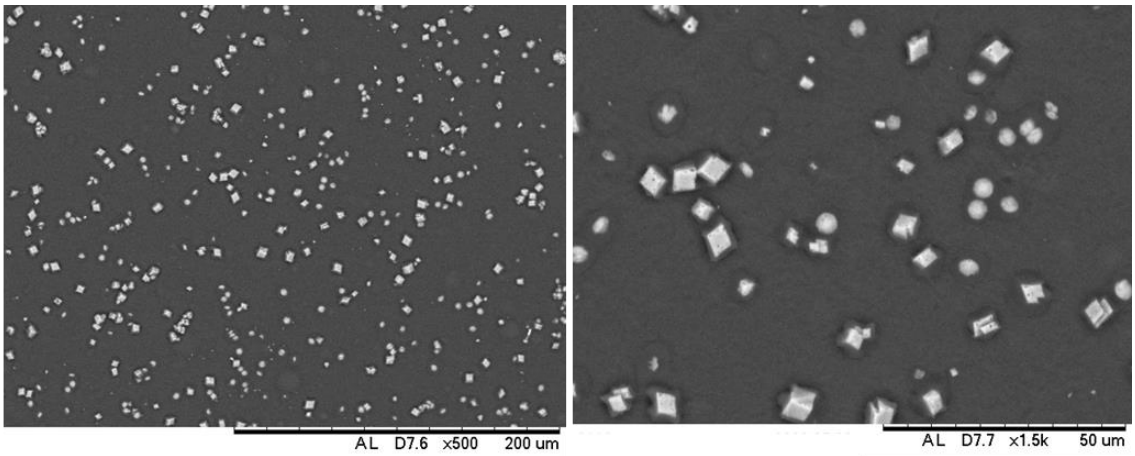

Figure 5: SEM image of calcium carbonate crystals obtained after 10 minutes of UV light irradiation of Ca^{2+}-agarose gel merged in ketoprofen aqueous solution.

Once having obtained light-controlled calcium carbonate crystallization and having fixed the crystals in a gel the aim was to localize the crystallization process, to write calcium carbonate structures with light. For this purpose, the gel system was irradiated with powerful and localized light sources, such as a focalized LED and a laser. With these sources it is possible to induce localized crystallization in few seconds to one minute, depending on the power of the source. In order to obtain more uniformity in crystals distribution in the gel, Ketoprofen concentration and $CaCl_2$ embedment method were changed. In particular, while at first agarose-sucrose gel was stored in $CaCl_2$ 20 mM solution before the irradiation process, then $CaCl_2$ was directly added during the gel preparation procedure to have a more homogeneous distribution of calcium ions inside the gel. Furthermore, because of the high power of the laser, a lot of Ketoprofen byproduct is precipitated along the light path in the solution and in the gel, even with very short time of irradiation. This causes a less effective irradiation inside the gel because of lack of transparency and a less effective $CaCO_3$ precipitation, caused by byproduct presence in the gel. Hence, in laser tests, Ketoprofen concentration was decreased from 20 mM to 2 mM. In particular, a Nd:YAG 355 nm pulsed laser was used as a source and a spot of crystals was generated in the gel, after 10 seconds of irradiation of the gel/solution system (Figure 6). Less ketoprofen byproduct formation was observed in solution and almost no byproduct formation was observed in the gel.

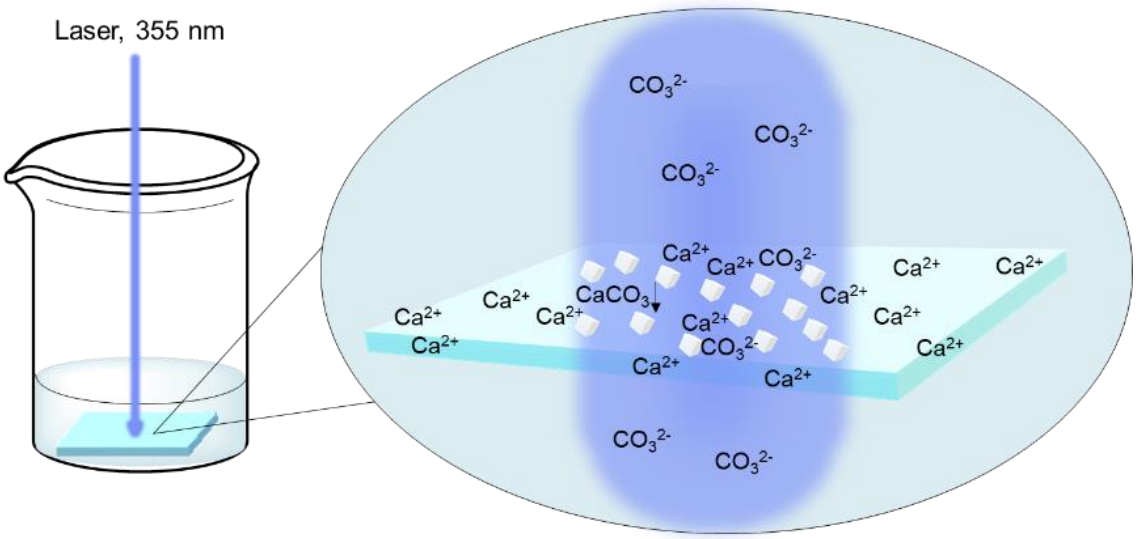

Figure 6: localized crystallization mechanism of calcium carbonate after laser irradiation at 355 nm of agarose gel, in which Ca^{2+} ions are embedded, merged in aqueous solution of Ketoprofen at pH 10.3.

After irradiation, the solution was promptly removed; no further steps of washing have been performed. Polarization microscopy shows calcite crystal spots that usually range from 1 mm to 1,5 mm of diameter (Figure 7).

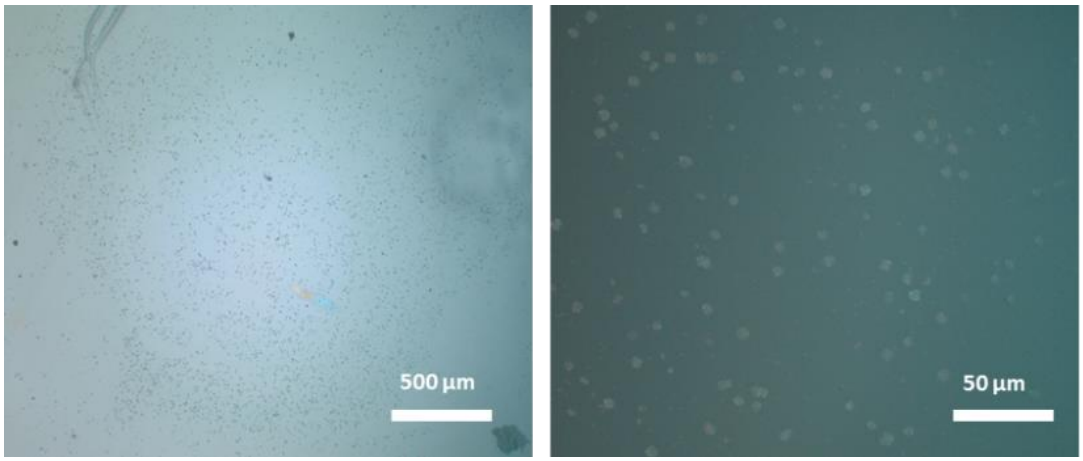

Figure 7: Polarization microscopy images of Ca^{2+}-agarose gel after having been covered with ketoprofen 2 mM aqueous solution at pH 10.3 and irradiated with laser at 355 nm: image of the crystals spot (left) and detail of crystals in the spot (right).

Localization of photoinduced precipitation of calcium carbonate was also performed by a focalized LED at 365 nm. The irradiation was performed by means of a fluorescence microscope modified for irradiation: the LED was focalized by the objective of the microscope and the sample

was irradiated from the bottom. The size of the beam could be considerably reduced by using objectives with higher magnifications. With this method, the irradiation lasts one minute and a white spot, probably corresponding to Ketoprofen byproduct and observed both with Ketoprofen 20 mM and Ketoprofen 2 mM, is generated in the gel, exactly where the light beam passes. Nevertheless, despite the byproduct formation in the gel, crystals are efficiently produced. This can happen because of the lower power with respect to the laser and the different irradiation setup, from the bottom of the sample, in which there is a thinner layer of solution between the light source and the gel. Furthermore, in the case of Ketoprofen 20 mM, also irradiation of 10 seconds has been tested and byproduct followed by crystals formation are still visible. The more focused spot and the use of a microscope as the irradiation setup allow to follow the formation of crystals in time. Indeed, right after irradiation and removal of the solution, the gel and the area in which the spot is formed can be monitored. In particular, crystals growth can be followed and are reported in Figure 8 for Ketoprofen 20 mM and an irradiation time of 10 seconds, using a 10x objective.

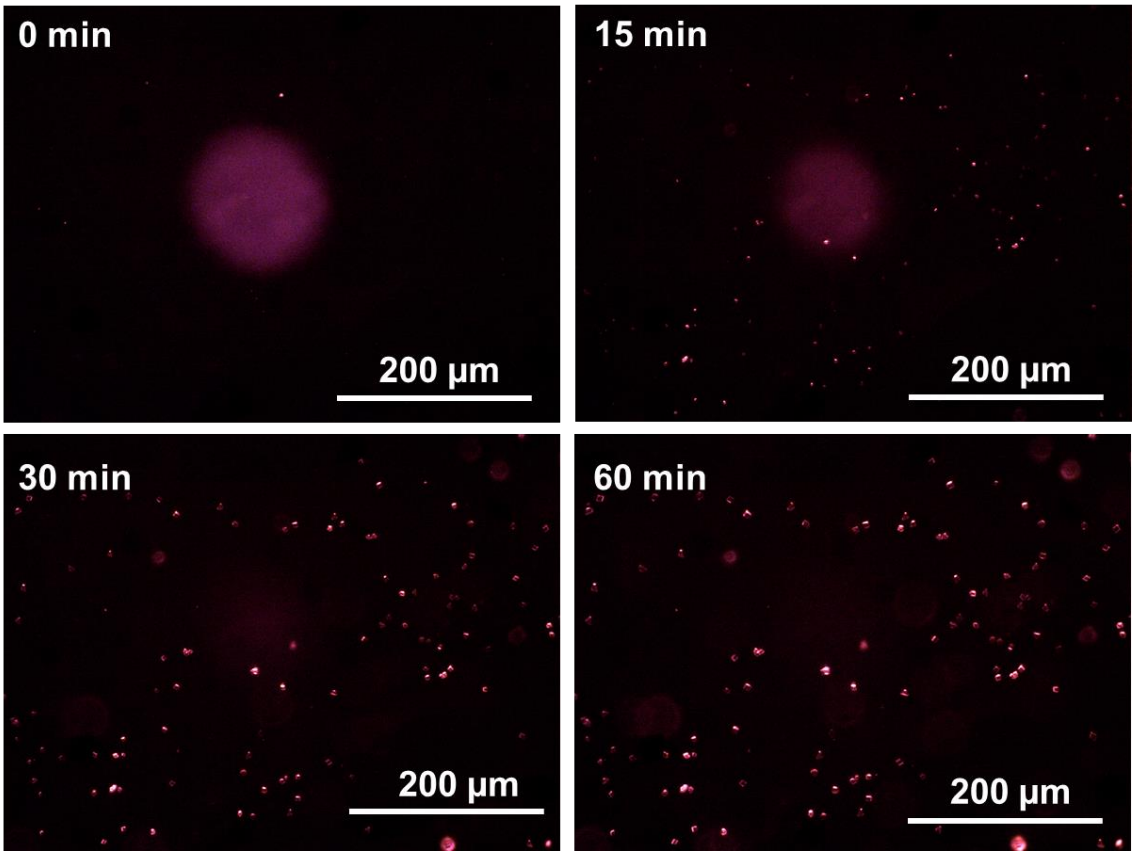

Figure 8: Crystals formation in the gel after irradiation. Crystals start to appear after 15 minutes from the end of irradiation.

Figure 8 shows what happens right after the irradiation process. The white spot in the image after irradiation correspond to the Ketoprofen organic byproduct that forms during irradiation. An interesting phenomenon is the gradual disappearance of this white spot, as if the byproduct starts to re-dissolve in the medium. This event was not observed before and the reason why it is visible in this case can be related to the fact that in all the experiments performed before a very high quantity of byproduct was formed, because of Ketoprofen concentration, irradiation time and type of source. At the contrary, with this setup and these times of irradiation, it was possible to precipitate less byproduct and observe its disappearance. Then, first crystals start to be visible after 15 minutes; at first their shape is not distinguishable but then calcite crystals growth is clearly visible. After almost 1 hour, crystals growth stops and a crystals spot of almost 1,5 mm of diameter is obtained. Thus, even with the irradiation of a smaller spot of the gel and the generation of less organic byproduct, it seems that the crystal formation is localized in the same scale. Thus, it surely is very important to deeper investigate the whole process, in order also to understand if there is a connection between the byproduct disappearance and the crystal growth and diffusion.

2.4.3. Conclusions

In this part of the work, we investigated the light-induced $CaCO_3$ precipitation process by means of Ketoprofen as a photo-generator of CO_2, that had been studied and verified only in solution, in a gel matrix. This was done in order to fix the calcium carbonate generated by light on a support. This could be a start point to develop a system in which $CaCO_3$ structures can be selectively written and developed by light for lithography or micropatterning application. The first step to achieve this purpose was to find a proper matrix and an agarose/sucrose gel was, among all the system tested, such as gelatin or alginate gels, the best support in which this kind of process could be undergone. Indeed, agarose/sucrose developed gel does not have any absorption in the irradiation range (350-365 nm) and scattering effect, is easy to prepare, stable in the proper humidity conditions, uniform and sufficiently thin. Since the main aim is to selectively induce precipitation by light, another challenge to overcome was precipitation in dark, which it was possible to avoid by adjusting $CaCl_2$ concentration and pH. In addition, our other purpose was to localize the process, in order to literally “write” with light. Both focused LEDs and lasers were used, and a certain localization was obtained. Nevertheless, more studies need to be done for this, in order to better control the localization and deal with diffusion that could not be totally avoided. Concluding, we developed a new promising system for photo-induced crystallization processes that were studied for calcium carbonate precipitation but could also be used to write structures based on other materials. Furthermore, this system in which crystals are formed and fixed can also lead to a deeper investigation on crystallization and diffusion phenomena.

2.5. Bibliography

1. Nunes, R. M. D.; Pineiro, M.; Arnaut, L. G., Photoacid for Extremely Long-Lived and Reversible pH-Jumps. *Journal of the American Chemical Society* **2009,** *131* (26), 9456-9462.
2. He, J.; Kimani, F. W.; Jewett, J. C., A Photobasic Functional Group. *Journal of the American Chemical Society* **2015,** *137* (31), 9764-9767.
3. Photochemical Reaction Mechanisms and Reaction Intermediates. In *Photochemistry of Organic Compounds*, Wiley, Ed. **2009**, 183-226.
4. Shi, Z.; Peng, P.; Strohecker, D.; Liao, Y., Long-Lived Photoacid Based upon a Photochromic Reaction. *Journal of the American Chemical Society* **2011,** *133* (37), 14699-14703.
5. Shirai, M.; Tsunooka, M., Photoacid and photobase generators: Chemistry and applications to polymeric materials. *Progress in Polymer Science* **1996,** *21* (1), 1-45.
6. Zivic, N.; Kuroishi, P. K.; Dumur, F.; Gigmes, D.; Dove, A. P.; Sardon, H., Recent Advances and Challenges in the Design of Organic Photoacid and Photobase Generators for Polymerizations. *Angewandte Chemie-International Edition* **2019,** *58* (31), 10410-10422.
7. Crivello, J. V.; Lam, J. H. V., Diaryliodonium Salts. A New Class of Photoinitiators for Cationic Polymerization. *Macromolecules* **1977,** *10* (6), 1307-1315.
8. Crivello, J. V.; Lam, J. H. W., Photoinitiated cationic polymerization with triarylsulfonium salts. *Journal of Polymer Science: Polymer Chemistry Edition* **1979,** *17* (4), 977-999.
9. Shirai, M.; Tsunooka, M., Photoacid and photobase generators: Prospects and their use in the development of polymeric photosensitive systems. *Bulletin of the Chemical Society of Japan* **1998,** *71* (11), 2483-2507.
10. Houlihan, F.; Shugard, A.; Gooden, R.; Reichmanis, E., Nitrobenzyl ester chemistry for polymer processes involving chemical amplification. *Macromolecules* **1988,** *21* (7), 2001-2006.
11. Ikbal, M.; Banerjee, R.; Atta, S.; Dhara, D.; Anoop, A.; Singh, N. D. P., Synthesis, Photophysical and Photochemical Properties of Photoacid Generators Based on N-Hydroxyanthracene-1,9-dicarboxyimide and Their Application toward Modification of Silicon Surfaces. *The Journal of Organic Chemistry* **2012,** *77* (23), 10557-10567.
12. Suyama, K.; Shirai, M., Photobase generators: Recent progress and application trend in polymer systems. *Progress in Polymer Science* **2009,** *34* (2), 194-209.
13. Asad, N.; Deodato, D.; Lan, X.; Widegren, M. B.; Phillips, D. L.; Du, L.; Dore, T. M., Photochemical Activation of Tertiary Amines for Applications in Studying Cell Physiology. *Journal of the American Chemical Society* **2017,** *139* (36), 12591-12600.
14. Fréchet, J. M. J., The photogeneration of acid and base within polymer coatings: Approaches to polymer curing and imaging. **1992,** *64* (9).

15. Bosca, F.; Miranda, M. A., Photosensitizing drugs containing the benzophenone chromophore. *Journal of Photochemistry and Photobiology B-Biology* **1998,** *43* (1), 1-26.
16. Sun, K. S.; Kumar, R.; Falvey, D. E.; Raghavan, S. R., Photogelling Colloidal Dispersions Based on Light-Activated Assembly of Nanoparticles. *Journal of the American Chemical Society* **2009,** *131* (20), 7135-7141.
17. Yucknovsky, A.; Mondal, S.; Burnstine-Townley, A.; Foqara, M.; Amdursky, N., Use of Photoacids and Photobases To Control Dynamic Self-Assembly of Gold Nanoparticles in Aqueous and Nonaqueous Solutions. *Nano Letters* **2019,** *19* (6), 3804-3810.
18. Bowitz, E.; Ibenholt, K., Economic impacts of cultural heritage - Research and perspectives. *Journal of Cultural Heritage* **2009,** *10* (1), 1-8.
19. Giorgi, R.; Baglioni, M.; Berti, D.; Baglioni, P., New Methodologies for the Conservation of Cultural Heritage: Micellar Solutions, Microemulsions, and Hydroxide Nanoparticles. *Accounts of Chemical Research* **2010,** *43* (6), 695-704.
20. https://www.iccrom.org/it/publication/causes-deterioration-mural-paintings.
21. Chelazzi, D.; Giorgi, R.; Baglioni, P., Microemulsions, Micelles, and Functional Gels: How Colloids and Soft Matter Preserve Works of Art. *Angewandte Chemie-International Edition* **2018,** *57* (25), 7296-7303.
22. Favaro, M.; Mendichi, R.; Ossola, F.; Simon, S.; Tomasin, P.; Vigato, P. A., Evaluation of polymers for conservation treatments of outdoor exposed stone monuments. Part II: Photo-oxidative and salt-induced weathering of acrylic-silicone mixtures. *Polymer Degradation and Stability* **2007,** *92* (3), 335-351.
23. Favaro, M.; Mendichi, R.; Ossola, F.; Russo, U.; Simon, S.; Tomasin, P.; Vigato, P. A., Evaluation of polymers for conservation treatments of outdoor exposed stone monuments. Part I: Photo-oxidative weathering. *Polymer Degradation and Stability* **2006,** *91* (12), 3083-3096.
24. Dietemann, P.; Higgitt, C.; Kalin, M.; Edelmann, M. J.; Knochenmuss, R.; Zenobi, R., Aging and yellowing of triterpenoid resin varnishes - Influence of aging conditions and resin composition. *Journal of Cultural Heritage* **2009,** *10* (1), 30-40.
25. Horgnies, M.; Darque-Ceretti, E.; Bayle, M.; Gueit, E.; Aucouturier, M., An exceptionally perennial surface artwork: fresco on lime or on cement. *Surface and Interface Analysis* **2014,** *46* (10-11), 791-795.
26. Chelazzi, D.; Poggi, G.; Jaidar, Y.; Toccafondi, N.; Giorgi, R.; Baglioni, P., Hydroxide nanoparticles for cultural heritage: Consolidation and protection of wall paintings and carbonate materials. *Journal of Colloid and Interface Science* **2013,** *392*, 42-49.
27. Piovesan, R.; Mazzoli, C.; Maritan, L.; Cornale, P., Fresco and lime-paint: an experimental study and objective criteria for distinguishing between these painting techniques. *Archaeometry* **2012,** *54*, 723-736.

28. Arnould, A.; Gaillard, C.; Fameau, A. L., pH-responsive fatty acid self-assembly transition induced by UV light. *Journal of Colloid and Interface Science* **2015,** *458*, 147-154.
29. Montalti, M.; Zhang, G.; Genovese, D.; Morales, J.; Kellermeier, M.; García-Ruiz, J. M., Local pH oscillations witness autocatalytic self-organization of biomorphic nanostructures. *Nature Communications* **2017,** *8* (1), 14427.
30. Brecevic, L.; Nielsen, A. E., Solubility of amorphous calcium-carbonate. *Journal of Crystal Growth* **1989,** *98* (3), 504-510.
31. Dektar, J. L.; Hacker, N. P., Photochemistry of diaryliodonium salts. *Journal of Organic Chemistry* **1990,** *55* (2), 639-647.
32. Crivello, J. V.; Lam, J. H. V., Diaryliodonium Salts. A New Class of Photoinitiators for Cationic Polymerization. *Macromolecules* **1977,** *10* (6), 1307-1315.
33. Pappas, S. P., Uv curing by radical, cationic and concurrent radical-cationic polymerization. *Radiation Physics and Chemistry* **1985,** *25* (4-6), 633-641.
34. Martin, C. J.; Rapenne, G.; Nakashima, T.; Kawai, T., Recent progress in development of photoacid generators. *Journal of Photochemistry and Photobiology C-Photochemistry Reviews* **2018,** *34*, 41-51.
35. Pence, W. H.; Baughcum, S. L.; Leone, S. R., Laser UV Photofragmentation of Halogenated Molecules. Selective Bond Dissociation and Wavelength-Specific Quantum Yields for Excited 1(2P1/2) and Br(2P1/2) Atoms. *Journal of Physical Chemistry*, **1981,** *85* (25), 3844-3851.
36. Morse, J. W.; Arvidson, R. S., The dissolution kinetics of major sedimentary carbonate minerals. *Earth-Science Reviews* **2002,** *58* (1-2), 51-84.
37. Goez, M.; Eckert, G.; Müller, U., Sensitized Photolysis of Iodonium Salts Studied by CIDNP. Solvent Dependence and Influence of Lipophilic Substituents. *Journal of Physical Chemistry A*, **1999,** *103* (29), 5714-5721.
38. Dadashi-Silab, S.; Aydogan, C.; Yagci, Y., Shining a light on an adaptable photoinitiator: advances in photopolymerizations initiated by thioxanthones. *Polymer Chemistry* **2015,** *6* (37), 6595-6615.
39. Karaca, N.; Ocal, N.; Arsu, N.; Jockusch, S., Chapter 1. Thioxanthone Photoinitiators with Heterocyclic Extended Chromophores. Royal Society of Chemistry: **2018**, 1-13.
40. Bignon, E.; Marazzi, M.; Besancenot, V.; Gattuso, H.; Drouot, G.; Morell, C.; Eriksson, L. A.; Grandemange, S.; Dumont, E.; Monari, A., Ibuprofen and ketoprofen potentiate UVA-induced cell death by a photosensitization process. *Scientific Reports* **2017,** *7* (1).
41. Monti, S.; Sortino, S., Photoprocesses of photosensitizing drugs within cyclodextrin cavities. *Chemical Society Reviews* **2002,** *31* (5), 287-300.

42. Bosca, F.; Miranda, M. A.; Carganico, G.; Mauleon, D., Photochemical and photobiological properties of ketoprofen associated with the benzophenone chromophore. *Photochemistry and Photobiology* **1994,** *60* (2), 96-101.
43. Riddlestone, I. M.; Kraft, A.; Schaefer, J.; Krossing, I., Taming the Cationic Beast: Novel Developments in the Synthesis and Application of Weakly Coordinating Anions. *Angewandte Chemie International Edition* **2018,** *57* (43), 13982-14024.
44. Trinh, T. K. H.; Morlet-Savary, F.; Pinaud, J.; Lacroix-Desmazes, P.; Reibel, C.; Joyeux, C.; Le Nouen, D.; Metivier, R.; Brosseau, A.; Heroguez, V.; Chemtob, A., Photoreduction of triplet thioxanthone derivative by azolium tetraphenylborate: a way to photogenerate N-heterocyclic carbenes. *Physical Chemistry Chemical Physics* **2019,** *21* (31), 17036-17046.
45. Pinaud, J.; Trinh, T. K. H.; Sauvanier, D.; Placet, E.; Songsee, S.; Lacroix-Desmazes, P.; Becht, J.-M.; Tarablsi, B.; Lalevée, J.; Pichavant, L.; Héroguez, V.; Chemtob, A., In Situ Generated Ruthenium-Arene Catalyst for Photoactivated Ring-Opening Metathesis Polymerization through Photolatent N-Heterocyclic Carbene Ligand. *Chemistry - A European Journal* **2018,** *24* (2), 337-341.
46. Normand, V.; Aymard, P.; Lootens, D. L.; Amici, E.; Plucknett, K. P.; Frith, W. J., Effect of sucrose on agarose gels mechanical behaviour. *Carbohydrate Polymers* **2003,** *54* (1), 83-95.

3. TiO_2 based materials as photocatalysts for water and air remediation

3.1. Introduction

Semiconductor photocatalysis is one of the biggest fields in photochemistry and Titanium Dioxide (TiO_2) surely represents the most known photocatalytic material. Indeed, its properties have been studied for almost one century[1] and in the last years a lot of common use applications are based on it, such as sunscreens, pigments and toothpastes[2]. Its growth of interest is due to its characteristics as a material and, more specifically as a photocatalyst. TiO_2 is a earth abundant, thus low cost and industrially scalable material, it is also chemically and thermically stable[3] and has a high photocatalytic efficiency with respect to other semiconductors.

TiO_2 polymorphs are rutile, anatase and brookite[1]. Rutile and brookite types have respectively a tetragonal crystalline structure with prismatic habit and an orthorhombic crystalline structure. Anatase has a tetragonal crystalline structure with a bipyramidal habit and it is the one with the major photocatalytic activity, because of high photostability, high specific area and a more negative conduction band edge potential that leads to a higher potential energy of the photogenerated electrons[4]. Since anatase TiO_2 bandgap is Eg ≈ 3.2 eV[5], it is activated by UV light. Once the exciton is generated, the electron and the holes could be trapped on TiO_2 surface and react with the nearest species. Photocatalytic mechanism of TiO_2 is reported in Figure 1.

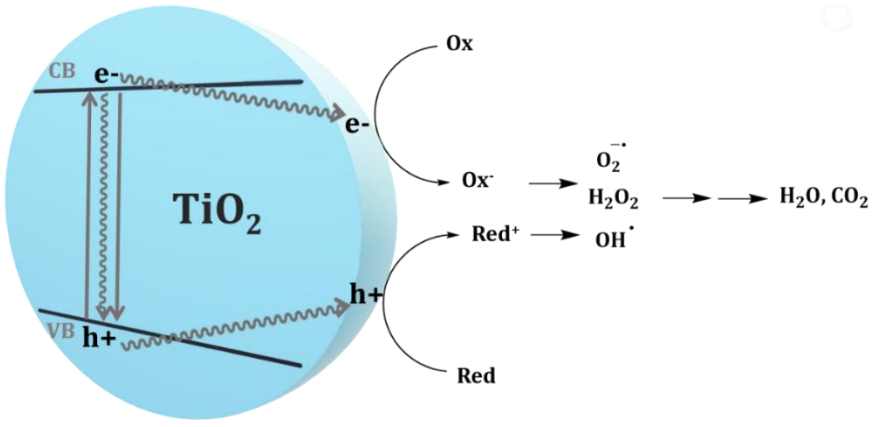

Figure 1: General photocatalytic behaviour of TiO_2.

Figure 1 shows the photocatalytic behaviour of TiO_2. Once the exciton is generated, it can give a charge recombination or a charge separation, in which the electron and the hole can migrate on the surface. Here redox processes start to happen with the molecules in the surroundings and/or with the molecules adsorbed on the surface. From redox processes in presence of oxygen and/or water, reactive oxygen species (ROS) are formed. Detailed mechanisms of ROS generation are still not totally understood but generally involve molecular oxygen reduction and water oxidation processes. Thus, the reactivity of TiO_2 with a molecule in the surroundings is given by two main processes. A photoinduced electron transfer can happen for a molecule adsorbed on TiO_2 surface, which directly undergoes oxidation or reduction; alternatively, the molecule is not directly transformed by TiO_2 excitation, but in a second moment by the generation of ROS. These two paths are at the basis of TiO_2 use as photocatalyst for environmental remediation. This has been one of the main issues worldwide for many years, since anthropic activities contaminate more and more water and air with toxic agents, threating environment and human health. Common sources of air pollution are household combustion devices, motor vehicles, industrial facilities and forest fires; the most important pollutants caused by these factors are carbon dioxide and monoxide, nitrogen dioxide and sulfur dioxide[6]. Water is usually contaminated by solvents, volatile organics, chlorinated volatile organics etc. that come mainly from industrial waste and groundwater represents one of the primary source of human contact with toxic agents[7].

TiO_2 use for pollutants degradation in water and air has been widely developed for many years but still represents a challenge. Besides the qualities that permit its use in various photocatalytic application, TiO_2 also presents some relevant drawbacks: a low absorption ability of visible light due to its high bandgap and a rapid electron-hole recombination[8], which lead to the loss of the 90% of irradiation light[9]; these drawbacks significatively decrease TiO_2 performances in environmental remediation. For example, TiO_2 for air remediation can only be exploited outdoor because of the UV component of solar light. Moreover, outdoor photocatalytic performances are also limited because of effects regardless of the nature of the photocatalyst, such as continuous refresh of the polluted air and sunlight intensity variations. Considering these issues, it is necessary to improve TiO_2 intrinsic photocatalytic performance. This can be achieved in mainly two ways. First, having TiO_2 nanomaterials, thus increasing the surface/volume ratio, favours surface-related processes rather than charge recombination. Second, TiO_2 can be modified with materials that enhance the mobility of the charges, such as graphene and other 2D materials (Figure 2).

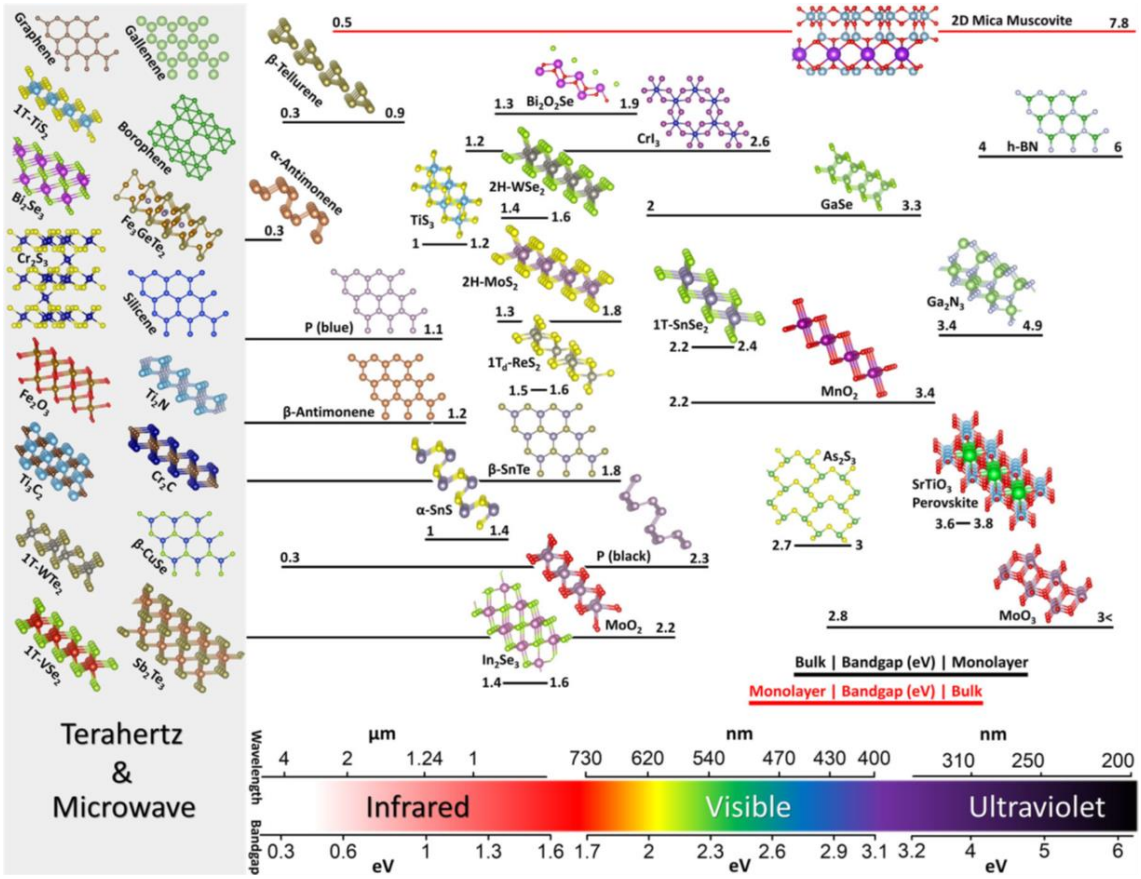

Figure 2: Main 2D materials and their bandgaps, in a wavelength/bandgap scale, reproduced from ref[10]

Graphene is one of the most investigated and used materials because of its 2D honeycomb structure[11] and its physical, chemical and electronic properties. It is a zero-bandgap semiconductor with a high thermal conductivity, good mechanical stability, large specific surface area and a superior electron conductivity and mobility[12, 13]. In particular, graphene and graphene related materials give to TiO_2 improvement of charge separation[12], increase of the surface-active sites[14] and also a bandgap tuning towards higher wavelengths, even if this mechanism is not clear yet[15]. Moreover, organic pollutants adsorption on the surface is increased by π-π stacking interactions with the 2D material layer (Figure 3).

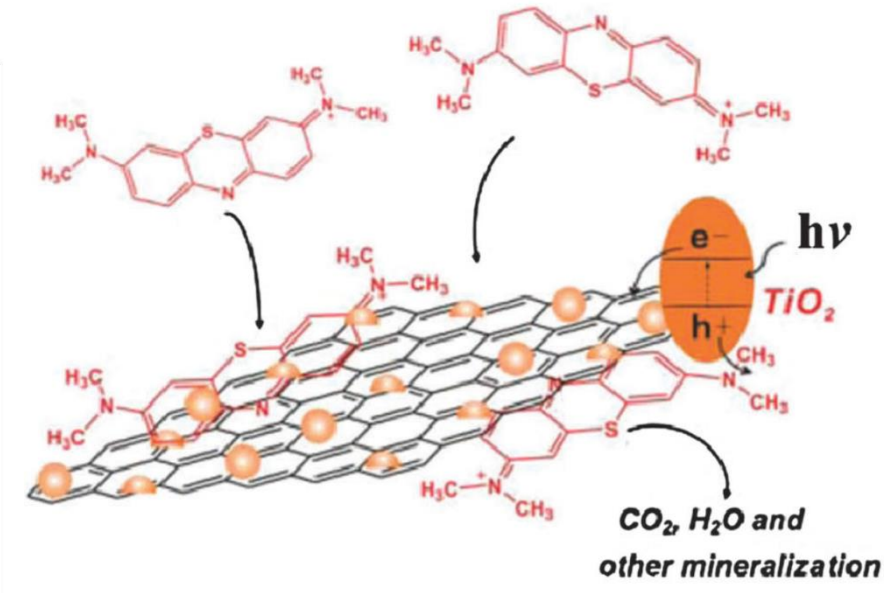

Figure 3: Role of graphene during the degradation of Methylene Blue by TiO_2 activation, reproduced from ref[16]

In this part of my PhD, TiO_2-based photocatalysts were studied for environmental remediation. TiO_2 nanoparticles were developed and studied for water remediation and photocatalytic cement coatings were studied for air pollutants degradation. In particular, inorganic and organic pollutants were represented by respectively NOx (NO_2 and NO) and Rhodamine B as models.

3.2. Transparent TiO_2 nano-systems as efficient photocatalysts for water remediation.

3.2.1. Materials

Synthesis of colloidal TiO_2 nanoparticles

Colloidal TiO_2 nanosystems synthesis was performed following the procedure reported in ref[17]. We performed several syntheses following the same procedure, but using TritonX-100 (Sigma Aldrich), Pluronic F-127(Sigma Aldrich), Sodium Cholate (Sigma Aldrich) and Hexadecyltrimethylammonium bromide (CTAB) (Sigma Aldrich) as surfactants. Surfactant (concentration 16 mM) and HCl 37% (1,4mL) were placed in a 500 mL round bottom flask with 250 mL H_2O. The solution was heated up at 50 °C and it was kept stirring for almost 30 minutes waiting for the surfactant to dissolve completely. Then, 17,4 mL of TIP (Titanium isopropyl oxide), corresponding to a concentration of 1,5% p/p, were added very rapidly. A white precipitate was immediately noticed. The reaction was left stirring at 50 °C overnight. The day after a slightly milky solution was obtained. In the case of Sodium Cholate, a white precipitate is also present, which is then separated by the milky top solution.

Nanoparticles characterization

Nanoparticles were characterized by Absorption spectroscopy (Perkin Elmer Lambda 650, DLS and HR-TEM. Absorption spectra (Perkin Elmer Lambda 750) were collected for 0.02 mg/ml dispersions of colloidal TiO_2 nanosystems and for commercial titania (AHP). For the analysis quartz cuvettes were used, and the absorpion range set up was 200-800 nm, with a scan speed of 414 nm/min. DLS (Malvern Zetasizer Nano-ZS) samples preparation was carried out by 1:100 diluition of 15 mg/mL TiO_2 nanoparticles solutions and filtration (PVDF filters, 450 nm) to avoid precipitates or any sort of impurities during analysis. HR-TEM were performed on samples deposited on a copper grid holey carbon and left drying at 50°C.

Rhodamine B degradation tests with TiO_2 photocatalysts

Rhodamine B (RhB) photodegradation tests were performed by irradiating TiO_2 photocatalysts aqueous solution (TiO_2 concentration 0.2 mg/mL) in presence of RhB 1μM with an Hg lamp at 313 nm in a quartz cuvette. Irradiation was performed for 15 minutes and absorption spectra were collected each 5 minutes.

Rhodamine B degradation tests for several irradiation cycles

Aqueous solution of TiO_2 photocatalysts and in presence of RhB $3x10^{-5}$M were prepared in disposable wells. They were left in dark for 40 minutes before irradiation. In each cycle, irradiation was performed by a solar simulator lamp (for 3 Mercury lamp Radium Sanolux HRC 300-280 E27) 30 minutes. After each cycle RhB was added to the solution in order to re-obtain a concentration of $3x10^{-5}$M.

Rhodamine B degradation test by real time fluorescence monitoring

Tests of RhB degradation by fluorescence monitoring were performed by irradiating the nanoparticles solutions at 0.2 mg/mL of TiO_2 in presence of RhB 1μM (absorbance of 0.1 in these conditions). The irradiation was performed in a spectrofluorimeter (Fluoromax Horiba). A 3mL glass vial filled with the solution was irradiated under stirring at 340 nm (excitation slit= 20). In the meantime, Rhodamine fluorescence spectra were continuously collected during the irradiation.

Synthesis of Graphene and MoS_2 doped colloidal TiO_2 nanoparticles

In a 20mL glass vial 15 mL aqueous dispersion was prepared with 9,4 mL of TiO_2 colloidal dispersion 15 mg/ mL and 15 mg of graphite/MoS_2. Dispersion was sonicated in the bath sonicator for 6 h at 40-50 °C, stirring manually for 1 minute every 30 minutes. Temperature was controlled by ice addition directly in the sonication bath. At this point the dispersion was centrifugated for 5 minutes at 9500 rpm. Finally, we collected the 65% of the top solution for analysis

3.2.2. Results

TiO_2 colloidal nanosystems: synthesis, characterization, and photocatalytic activity

TiO_2 nanoparticles (NP), have been widely used for ROS generation in the form of powder, film or solid dispersion but very rarely as stable water dispersed NPs, mostly for the difficulty of achieving a transparent suspension of monodispersed, small, photoactive NPs. Here we describe colloidal TiO_2 nanoparticles dispersions synthesized accordingly to a highly environmental friendly templated method[17] (no high temperature or pressures or solvent other than water are needed) that forms extremely transparent water dispersions stable for months.

TiO_2 NPs were syntheses as schematized in Figure 1 (a) using micelles as templating agents to control the growth of TiO_2 formed from the hydrolysis and condensation of the molecular precursor TIP. The reaction, carried on in mild condition (50 °C during stirring), was performed

to obtained TiO_2 nanoparticles with common non-ionic (Pluronic F-127 and Triton X-100) and ionic (Cethyltrimethylammonium bromide-CTAB and Sodium Cholate) surfactants (Figure 1-b).

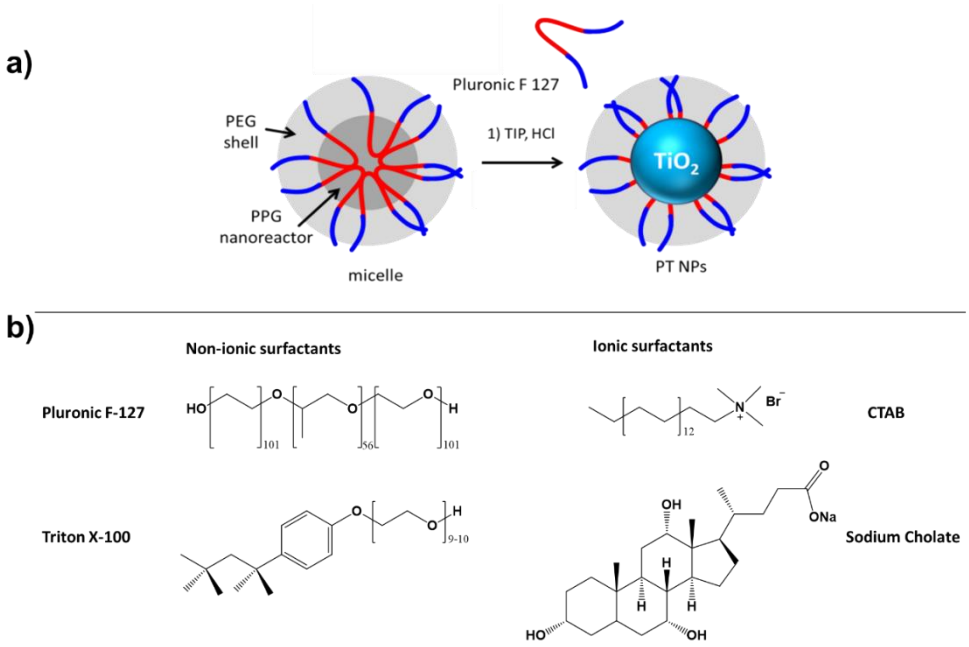

Figure 1: a) surfactant-assisted method for TiO_2 nanoparticles synthesis in the case of Pluronic-F127. b) Surfactants used to obtain different TiO_2 NPs.

Using all the surfactants (Figure 1- b), very stable and transparent TiO_2 nanoparticles are obtained. Using TiO_2 photocatalyst in this form can be really improving for water remediation (Figure 2).

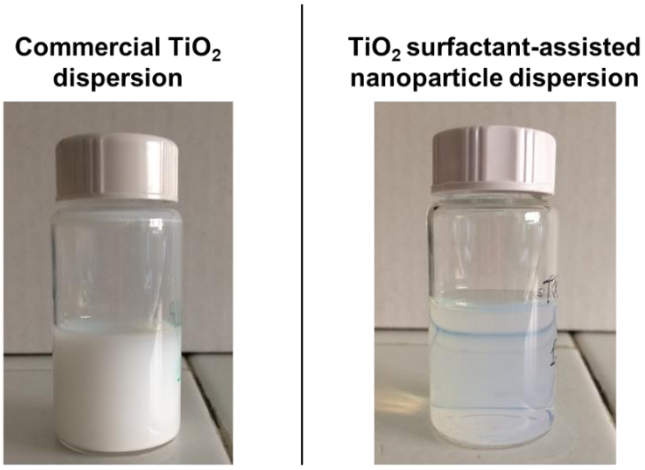

Figure 2: Comparison between a dispersion of commercial AHP TiO_2 in water obtained by sonication and a dispersion of TiO_2 colloidal nanoparticles.

Indeed, the main difficulties of commercial TiO_2 powders for water remediation are connected to the fact that nanoparticles, usually obtained by sonication, are not stable, thus they easily tend to aggregate, forming very turbid dispersions. This uncontrollable aggregation leads to a lower surface area, that does not promote the migration of the charges to the surface, enhancing the electron-hole pair recombination rate. Furthermore, the high turbidity makes TiO_2 activation by light less efficient and inhomogeneous because of relevant scattering effects due to particle size. All these aspects inevitably lower TiO_2 photocatalytic performance. Therefore, having a transparent, stable dispersion with small and homogeneously distributed nanoparticles is a great advantage for the TiO_2 reactivity.

The four nano-systems were previously characterized by absorption spectroscopy, reported in Figure 3.

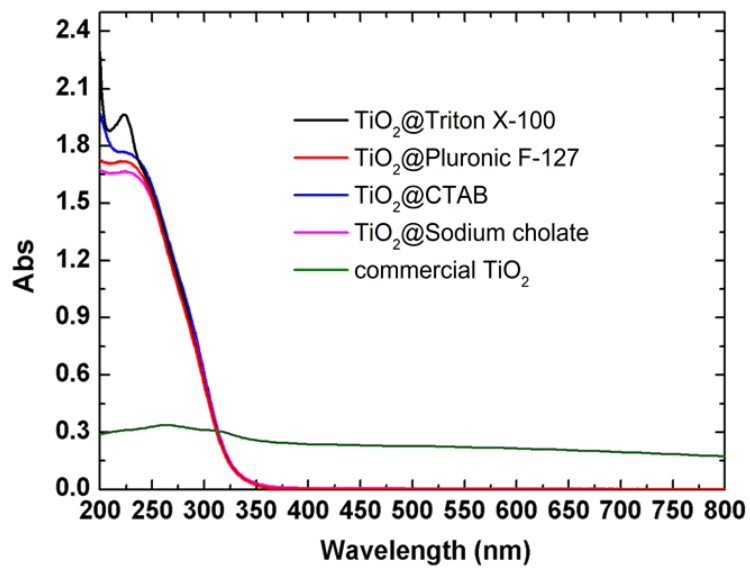

Figure 3: absorption spectra of all the synthesized TiO_2 colloidal nanoparticles and comparison with commercial TiO_2 AHP

In Figure 3 colloidal TiO_2 nanosystem absorption bands are showed and they are also compared with the absorption band of commercial TiO_2 powder (AHP) dispersed in water by sonication, prepared at the same TiO_2 concentration of the colloidal samples.

First, absorption spectra highlight the transparency of colloidal TiO_2 nano-dispersions with respect to commercial TiO_2, in which a scattering contribute to the absorption band is evident. Furthermore, the absorption band of TiO_2-colloidal systems is far more intense than the one of commercial TiO_2; this is another consequence of their transparency and their stability with

respect to commercial powder. Another interesting difference that must be noted stays in the absorbance wavelength of the two species. Indeed, colloidal systems absorb at a slightly lower wavelength. This can be related to a quantum confinement effect and thus to particles with a very small size. The four TiO_2 nanosystems have almost the same absorption band shape. Only in the case of TiO_2@Triton X-100 a peak corresponding to the absorption peak of the surfactant can be distinguished.

TiO_2 nanoparticles dimension was characterized by DLS (Table 1) and HR-TEM (Figure 4).

	Z-Average	PDI
TiO_2@Triton X-100	28	0.17
TiO_2@Pluronic F-127	23	0.18
TiO_2@CTAB	22	0.21
TiO_2@Sodium Cholate	28	0.17

Table 1: DLS of colloidal TiO_2 nanoparticles

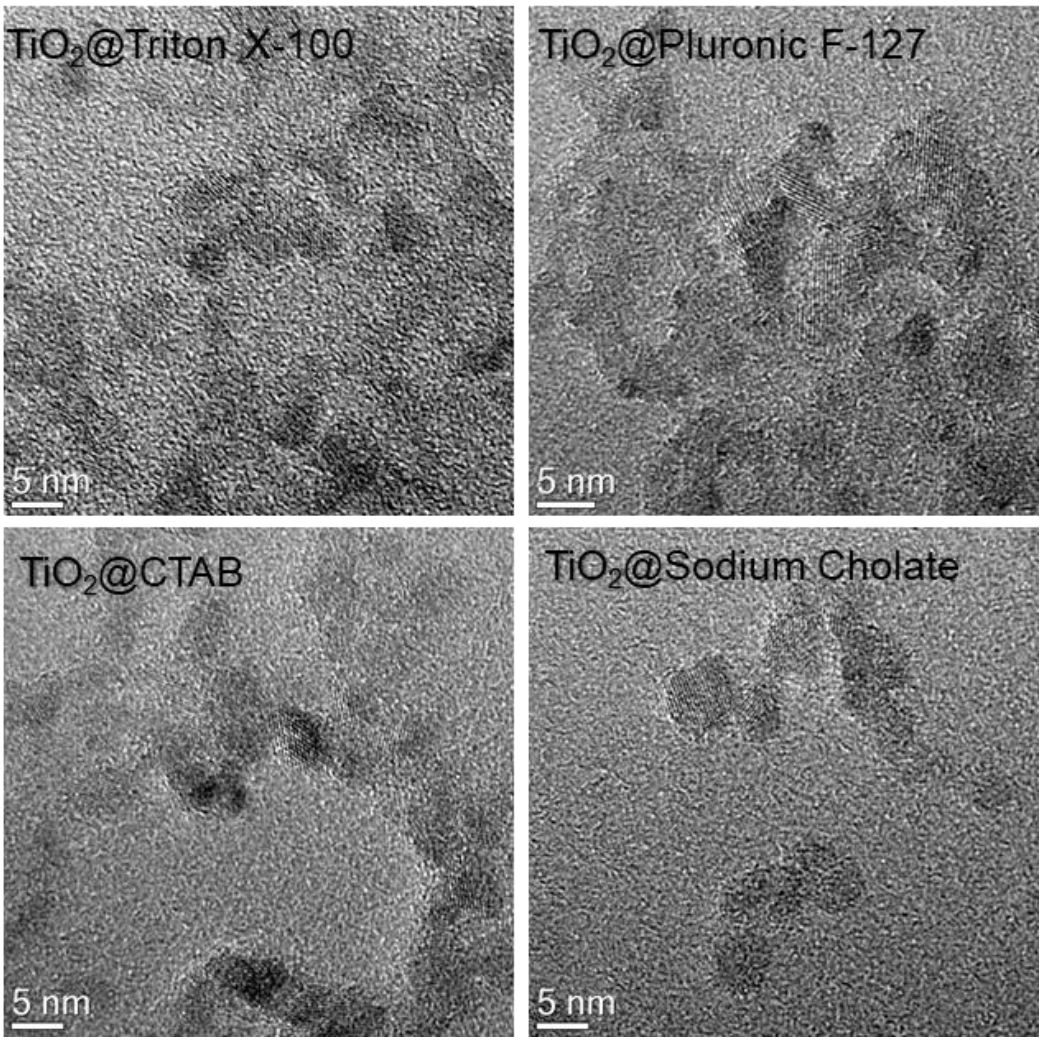

Figure 4: HR-TEM of TiO_2 colloidal nanoparticles.

As it can be noticed both in Table 1 and in Figure 4, the TiO_2 colloidal nanosystems size do not depend on the surfactant used but are all almost the same and they have a quite unform size distribution. However, DLS and HR-TEM report different sizes: from DLS an average size between 22 and 28 nm is observed, while the TEM shows smaller sizes, almost around 7-5 nm. The size observed from the TEM images represents the TiO_2 core, while probably the higher size in the DLS is due to the presence of a surfactant sphere. TiO_2 core is crystalline and EDX confirms that we have anatase polymorph that is the most active one for photocatalysis.

Photocatalytic performance in water remediation was evaluated by testing the degradation of a highly used model of organic pollutant, Rhodamine B (RhB), under the action of TiO_2 photocatalyst. The test was performed by observing the decrease of absorbance peak of RhB during irradiation at 313 nm, in presence of TiO_2 nanoparticles (Figure 5).

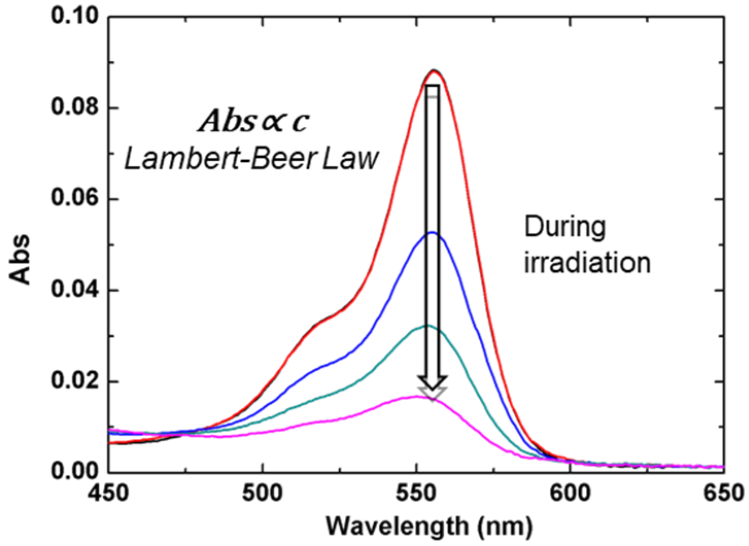

Figure 5: evaluation of RhB degradation under light irradiation in presence of TiO_2 photocatalysts by means of absorbance decrease.

The absorbance change of RhB can indeed be correlated to the change of its concentration by the Lambert-Beer law and thus to the degradation of the dye.

TiO_2 colloidal nanosystems were then compared by considering the intensity variation of RhB absorbance maximum during the irradiation time, as reported in Figure 6.

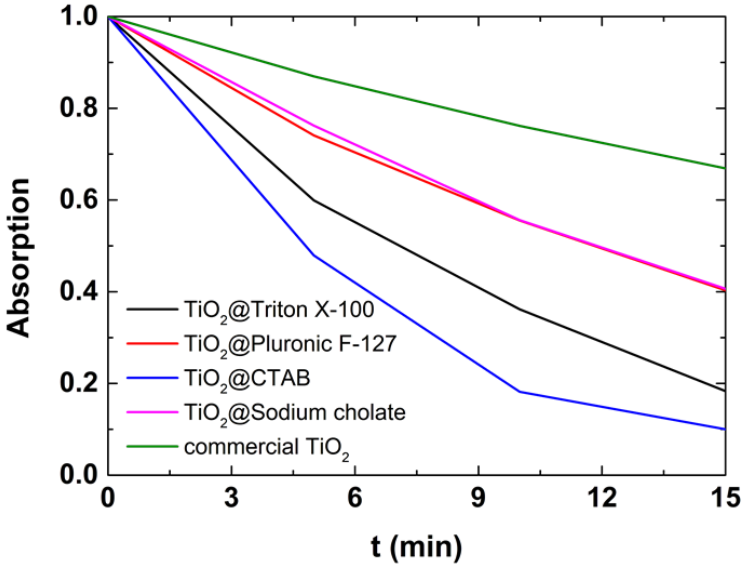

Figure 6: RhB absorption maximum (557 nm) decrease during irradiation at 313 nm, in presence of colloidal TiO_2 nanosystems and comparison wit commercial TiO_2 (AHP).

Based on these trends, the degradation percentage of the dye can be obtained as reported in the following equation.

$$RhB\ degrad.\% = 1 - \frac{Abs(\lambda_{max}, t)}{Abs(\lambda_{max}, t = 0)} \cdot 100 \qquad \text{Eq.1}$$

According to Eq.1, RhB degraded percentage can be calculated to compare the photocatalytic performances of the TiO_2 colloidal nanosystems and commercial TiO_2 powder dispersed in water (Table 2).

	RhB degraded after 15 minutes UV irradiation (%)
TiO_2@Triton X-100	82%
TiO_2@Pluronic F-127	60%
TiO_2@CTAB	90%
TiO_2@Sodium Cholate	59%
Commercial TiO_2	33%

Table 2: RhB degraded percentage in all the TiO_2 colloidal nanodispersion and in commercial TiO_2 dispersed in water after 15 minutes of irradiation at 313 nm.

Looking at Table 2, we can notice that the difference between the activity of the commercial powder dispersion and colloidal nanosystems is evident, indeed, commercial TiO_2 degrades only the 33% of RhB in 15 minutes of irradiation, while the other systems all degrade always more at least the 60% of the dye, so at least twice as the performance of the dispersed powder. Furthermore, TiO_2@Triton X-100 and TiO_2@CTAB show a very high activity: their performance is enhanced respectively of almost 160% and 200% compared to commercial TiO_2. These results thus confirm the advantages that colloidal nano dispersions bring to the photocatalytic activity of TiO_2.

After having verified the efficiency of TiO_2 colloidal nanosystems in Rhodamine B degradation, we tested the resistance of the photocatalyst in RhB degradation for several cycles of irradiation. In particular we performed these tests irradiating colloidal TiO_2 dispersions in water with RhB by means of a solar simulation lamp for 5 cycles of irradiation, monitoring the process with a camera and correlating the camera pixel intensity variation during the process with RhB degradation. After each cycle new dye was added in order to always start from the same concentration. Figure

7 shows the decrease of RhB absorption, correlated to pixel intensity, during irradiation in the five cycles.

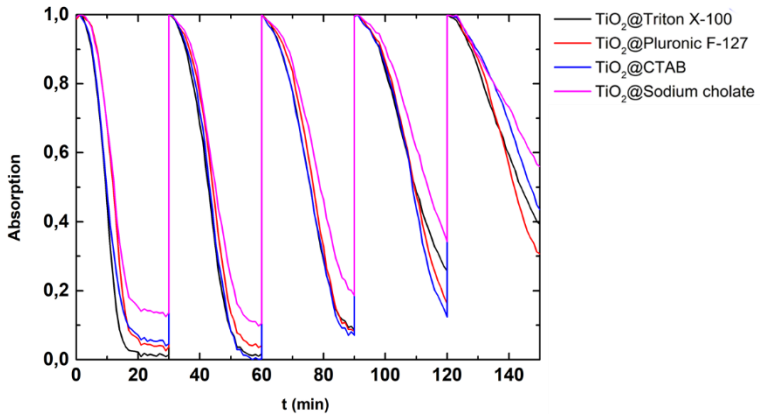

Figure 7: RhB absorbance variation during 5 irradiation cycles with colloidal TiO_2 nanoparticles

We can notice from Figure 7 that the photocatalytic activity remains very high for the first three cycles in every sample and has a decrease in the last two cycles. However, even at the fifth cycle, all the samples apart from TiO_2@Sodium Cholate, still degrade more than the 50% of RhB. These studies on photocatalytic performance under several cycles of irradiation highlight differences between the stability of TiO_2 photocatalysts based on the surfactant used. RhB degradation percentages for every cycle for all the samples are reported in Figure 8.

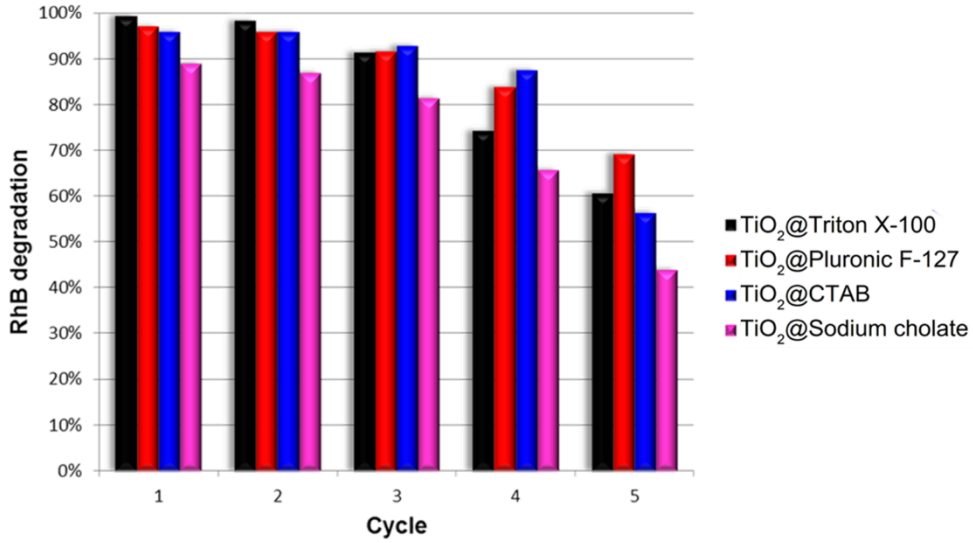

Figure 8: RhB degradation percentages for 5 cycles of irradiation

Figure 8 shows that there are some differences between the photocatalysts in the performance during different cycles of irradiation. As expected, for the first two cycles, TiO_2@Triton X-100 and TiO_2@CTAB show the best photocatalytic activity like it was observed in the first performance test (Figure 6). Instead, in the last three cycles TiO_2@CTAB and mainly TiO_2@Pluronic F-127 are the most stable ones under irradiation cycles.

Photocatalytic activity of TiO_2 colloidal nanoparticles in the degradation of Rhodamine B was also studied by means of another method: correlating the decrease in Rhodamine B fluorescence with degradation. With this method TiO_2 nanoparticle solutions are irradiated in a spectrofluorimeter at 340 nm. The use of this wavelength allows to activate the photocatalyst and observe Rhodamine B fluorescence, since RhB has an absorbance peak at that wavelength (Figure 9). Then, the fluorescence decrease can be correlated to a concentration decrease and thus to degradation. Indeed, emission intensity (I_{em})is directly proportional to the absorbed intensity (I_{ass}), and knowing the correlation between transmitted light intensity and absorbance (Eq.2) we can obtain the dependence of the emission intensity to absorbance (Eq3, 4).

$$I_t = I_0 \cdot 10^{-A} \qquad \text{Eq.2}$$

$$I_{ass} = I_0 - I_t = I_0(1 - 10^{-A}) \qquad \text{Eq.3}$$

$$I_{em} \propto I_0(1 - 10^{-A}) \qquad \text{Eq.4}$$

Here, I_t and I_0 stay respectively for transmitted light intensity and incident light intensity, while A represents absorbance.

In particular, for absorbance values below 0.1, the following equations can be written, according to Lambert-Beer law:

$$A \leq 0.1 \;\; ; \;\; 1 - 10^{-A} \approx Aln10 \qquad \text{Eq.5}$$

$$I_{em} \propto A \propto c \qquad \text{Eq.6}$$

Therefore, in these conditions of absorbance the emission intensity can be directly correlated to concentration (c) and thus to degradation. This method is advantageous with respect to the one that exploits absorbance signals (Figure 5) because irradiating and detecting with the same source permits to follow the degradation process in real time.

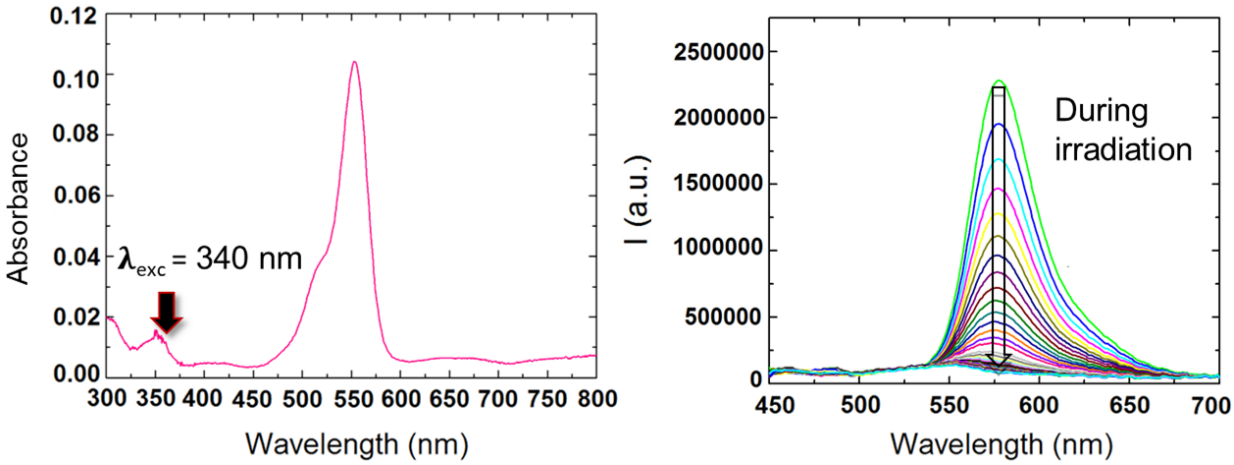

Figure 9: method of RhB degradation obtained by irradiation at 340 nm, in which also RhB can be excited (left) and monitored by Rhodamine decrease of fluorescence.

Therefore, this method allowed to better monitor the Rhodamine B degradation and to obtain information about the mechanism of degradation. Typical degradation mechanisms of Rhodamine B are reported in Figure 10.

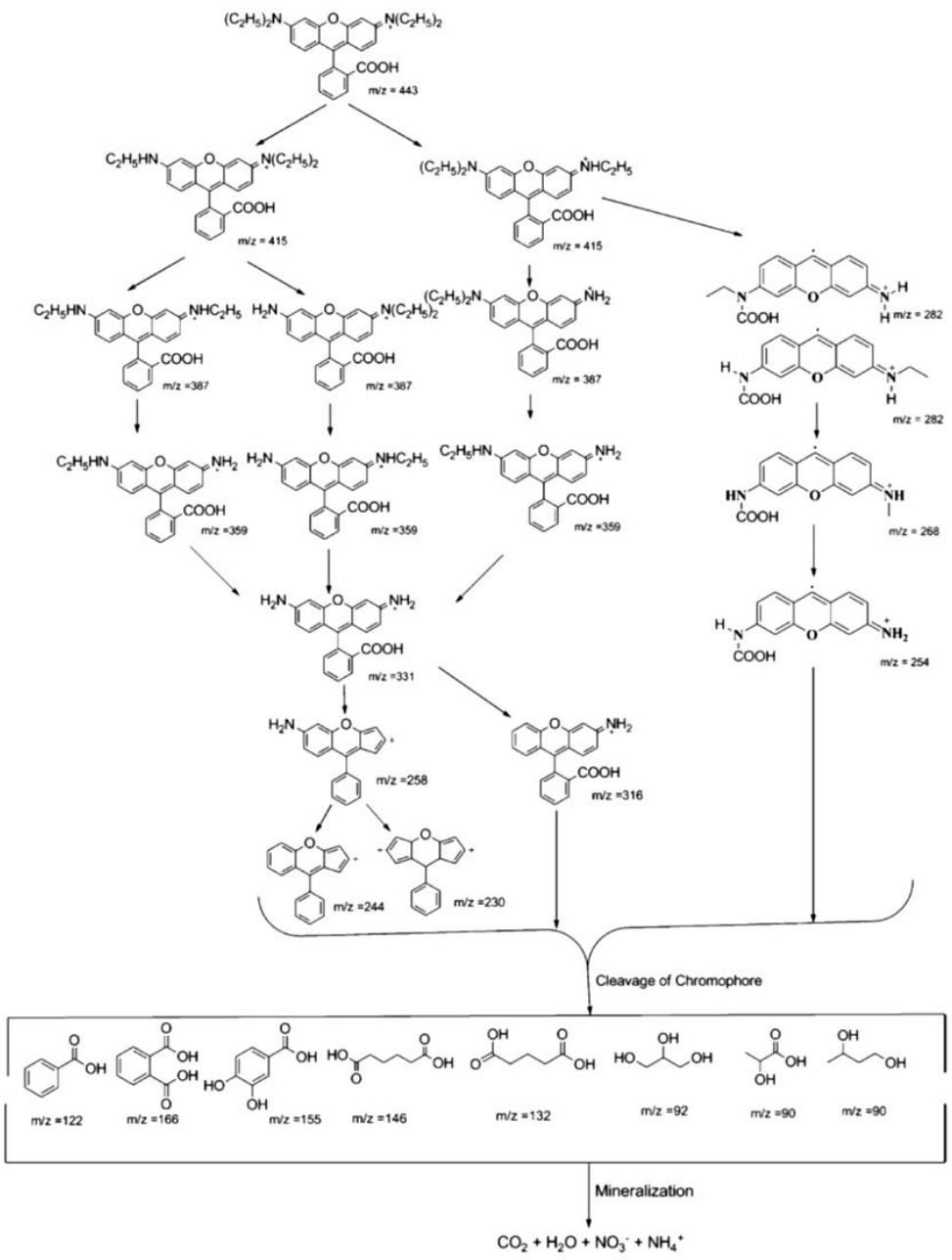

Figure 10: Possible Rhodamine B degradation pathways, reproduced with permission from ref[18]

From fluorescence spectroscopy it is possible to have some information about the Rhodamine B degradation mechanism. Indeed, in Rhodamine B fragmentation are often observed de-ethylation mechanisms. These processes always lead to a blue shift in the absorption and emission spectra [19]. Thus, a study of the emission of RhB during degradation can help to recognize these intermediates because of higher sensitivity of the fluorescence with respect to absorbance. Rhodamine B degradation monitoring by fluorescence spectroscopy was performed for all the TiO_2 colloidal nanosystems. What is usually observed is a decrease of emission intensity during irradiation, with trends like the one reported in Figure 9-right. This trend is common for all the

photocatalyst but TiO_2@CTAB for which, almost one minute after the beginning of the irradiation, a very intense emission peak starts to appear at 530 nm.

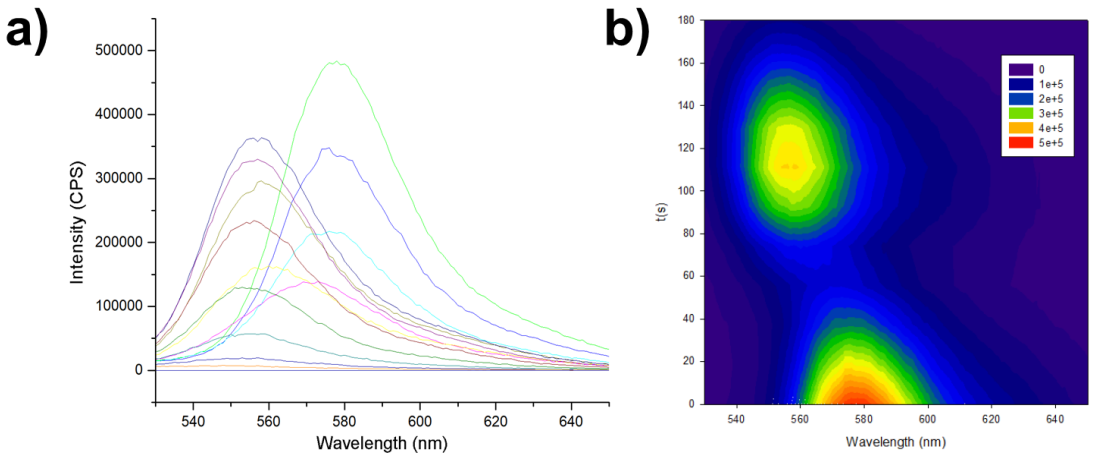

Figure 11: TiO_2@CTAB sample irradiated in presence of Rhodamine B at 340 nm. a) Observation of fluorescence spectroscopy: spectra are collected continuously during irradiation. Each spectrum is collected almost every 40 seconds. b) map of time resolved emission spectroscopy (TRES) of Rhodamine B degradation in presence of TiO_2@CTAB.

The emission peak at 530 nm could be attributed to the de-ethyled forms of Rhodamine B which usually absorbs between 510 and 540 nm[19]. From these data we could not distinguish which is the precise mechanism. We can say that a de-ethylation process probably occurred and mainly that TiO_2@CTAB nanosystem promotes a different RhB degradation mechanism with respect to the other colloidal nanoparticles. This means that the surfactant used can have an influence on the mechanism of degradation, probably having a role in contrasting or favouring the adsorption of the species on the photocatalyst surface. Further investigation needs to be performed to better understand these phenomena, but the emission monitoring is a significant technique to obtain more information on photocatalytic behaviour.

Modification of TiO_2 colloidal nanoparticles by means of Graphene and MoS_2

Modification of TiO_2@Triton X-100, TiO_2@CTAB and TiO_2@Sodium Cholate was performed by means of Graphene and MoS_2 to study the effect that these 2D could have had TiO_2 photocatalytic activity. Indeed, doping with these materials should contrast the electron-hole pair recombination favouring the photocatalytic performance. We performed a one pot exfoliation-doping reaction.

That means that 2D graphene related material is exfoliated by TiO_2 colloidal dispersions and thus dopes the photocatalyst directly during the exfoliation. In particular, TiO_2 colloidal nanoparticles dispersions in presence of Graphene or MoS_2 were prepared by a 6-hour sonication and centrifugation. The top solution was then collected and characterized (Figure 12).

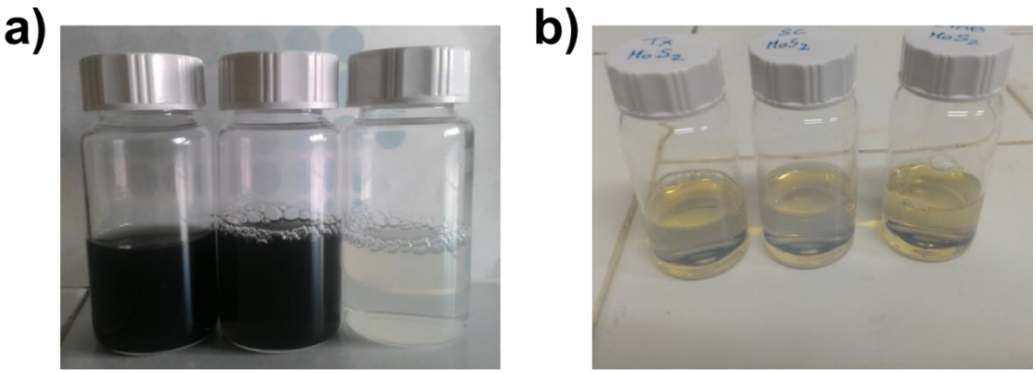

Figure 12: a) TiO_2@Sodium Cholate, TiO_2@CTAB and TiO_2@Triton X-100 doped with Graphene. b) TiO_2@Triton X-100, TiO_2@Sodium Cholate and TiO_2@CTAB doped with MoS_2

First, we could immediately notice that graphene and MoS_2 exfoliations have led to good results for both TiO_2@Sodium Cholate and TiO_2@CTAB cases. Indeed, solution has become dark grey in graphene-doped samples and pale yellow in MoS_2 ones. Doping seems successful in TiO_2@Triton X-100 for MoS_2, while no presence of Graphene is observed. Samples were characterized by absorption spectroscopy to better understand their properties.

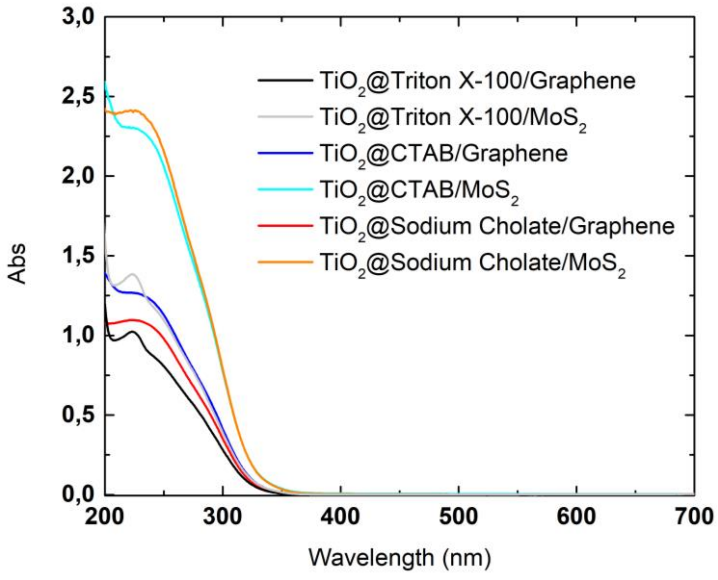

Figure 13: Absorption spectra of TiO_2 colloidal nanoparticles by graphene and MoS_2

Figure 13 shows how absorption spectra change after the exfoliation of TiO_2 colloidal nanosystems with Graphene and MoS_2. Indeed, it is clear that the surfactant influences the exfoliation effectiveness and the stability of TiO_2 with sonication. Indeed, in most samples, the exfoliation process obtained by sonication and centrifugation led to a TiO_2 nanoparticles aggregation, as absorbance decrease highlights. Indeed, probably part of TiO_2 colloidal nanoparticles aggregate and precipitate during the sonication/centrifugation and are then eliminated.

Photocatalytic activity was determined by monitoring RhB degradation by means of the decrease of its fluorescence intensity (Figure 9), irradiating at 340 nm (Figure 14-16).

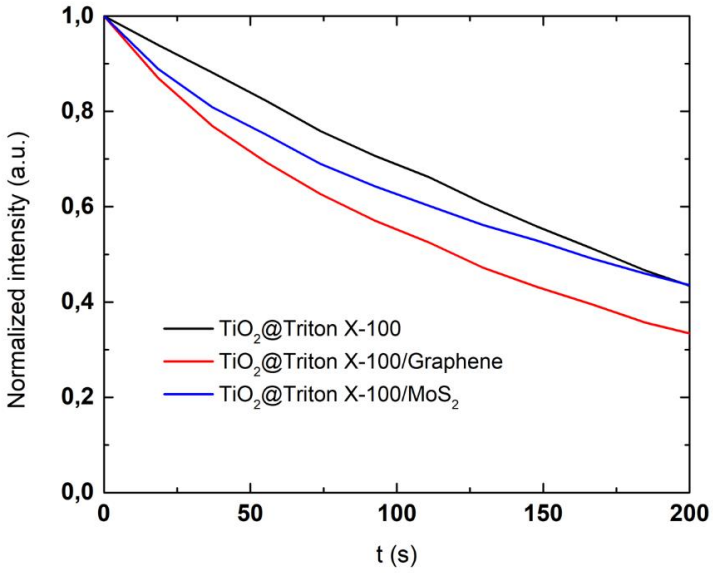

Figure 14: TiO_2@Triton X-100 RhB degradation trends, comparison between doping with Graphene and MoS_2

In TiO_2@Triton X-100 (Figure 14), modification with 2D materials bring enhance the photocatalytic efficiency, mainly in the case of Graphene doping. This is surprising, because, from the result of the exfoliation process, a very low quantity of graphene is present in the final dispersion and TiO_2 absorbance has a decrease. This effect must be further investigated, changing the ratios between graphene and TiO_2 concentration or graphene and surfactant concentration.

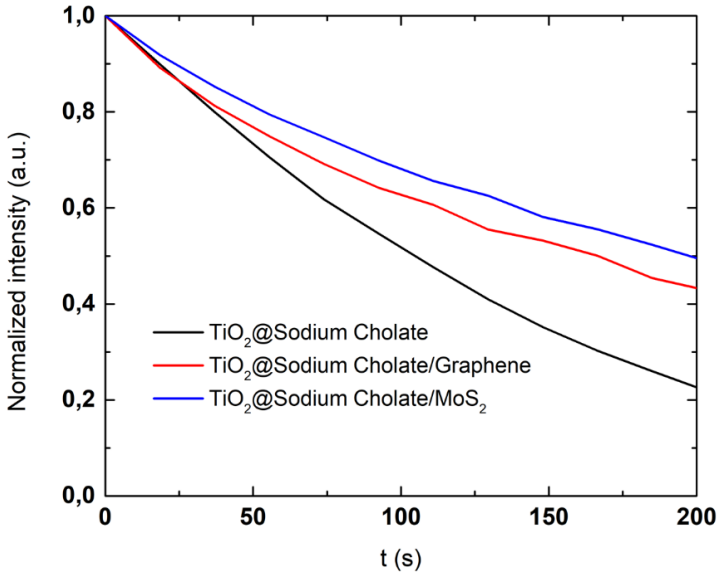

Figure 15: TiO_2@Sodium Cholate RhB degradation trends, comparison between doping with Graphene and MoS_2

In contrast to effect on Triton X-100 stabilized TiO_2 nanoparticles, TiO_2@Sodium Cholate nanoparticles are negatively affected by modification both with Graphene and MoS_2. Looking at the absorption spectra, decrease of the activity in presence of Graphene can be due to a decrease in TiO_2 concentration due to aggregation. Instead, MoS_2 does not compromise TiO_2 aggregation, thus the decrease in activity is due to another effect, that could be a hindrance of MoS_2 on TiO_2 surface that inhibits Rhodamine B adsorption; if this hypothesis is verified, it can give information on the degradation mechanism, which could happen mainly by adsorption.

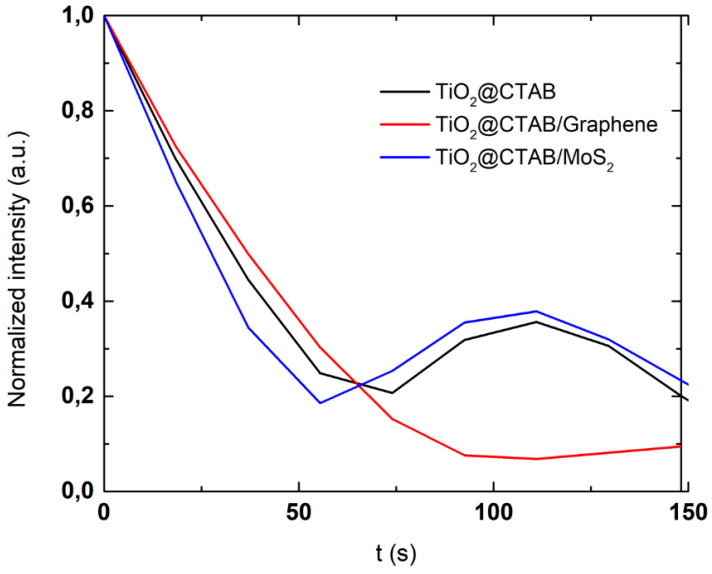

Figure 16: TiO_2@CTAB RhB degradation trends, comparison between doping with Graphene and MoS_2

As already mentioned, TiO_2@CTAB has a different mechanism with respect to the other TiO_2 photocatalysts, since in this system a byproduct formation (probably de-ethyled RhB) is observed during irradiation, if fluorescence is observed. This makes the photocatalytic activity evaluable only in the first 50 seconds of the reaction. The performances observed in the first 50 seconds are slightly lower for Graphene doping and slightly higher for MoS_2 doping, but a bigger difference is noticed in the mechanism. For graphene modification, no byproduct fluorescence appearance is noticed. Also in this case, this can be connected to a steric hindrance of graphene on TiO_2 surface, but this hypothesis needs further verifications and investigations.

3.2.3. Conclusions

Colloidal TiO_2 nanosystems were obtained by an easy surfactant assisted methods, using ionic and not ionic surfactants. Very small nanoparticles are obtained (5-6 nm of TiO_2 core) that confer a very high transparency and photocatalytic activity in water. Furthermore, they can also be stable for months. Photocatalytic activity for water decontamination was evaluated by considering Rhodamine B as a model of organic pollutant. These colloidal aqueous dispersions of nanoparticles show not only very good photocatalytic performances but also resistance to several irradiation cycles, maintaining their photocatalytic properties. A new method for photocatalytic activity evaluation was also developed. This method is based on correlation between Rhodamine B decrease of fluorescence and its degradation. This allows to perform a real time monitoring of Rhodamine B degradation, by using a spectrofluorimeter as the irradiation source, while observing the fluorescence of the dye. With this method is possible to obtain more information on the Rhodamine B degradation mechanism which depends on the surfactant used to stabilize TiO_2 nanoparticles. Doping of TiO_2 colloidal nanoparticles with Graphene and MoS_2 was also performed, in order to study an enhance in photocatalytic activity by the reducing of charge recombination process usually given by 2D materials. Surprising results came out from these modifications that highlight the complexity of these TiO_2 systems, which photocatalytic properties can deeply change based on the surfactant used in the synthesis of the nanoparticles and that surely needs more investigation.

3.3. Colloidal TiO_2 nanoparticles modified by melanin

3.3.1. Materials

PDA-TiO_2@Pluronic F-127 nanoparticles synthesis, drying processes and re-dissolution

A solution 1 mg/mL of L-Dopa and 1 mg/mL of Plu-TiO_2 was prepared, then NaOH was added to this solution, in order to obtain a pH almost 9 and let the L-Dopa polymerize to form melanin. As the base is added, the solution immediately become orange and after few hours of reaction it starts to assume a dark brown colour, typical of melanin. The solution was dried by heating or by lyophilization just after the addition of the base (orange solution) and after 24 hours from the beginning of the reaction (dark brown solution). Samples dried by heating were stored in an oven at 50°C for one day, while lyophilized samples were left in the freeze-drying until a powder was obtained. Powder were dissolved in water considering a concentration of 2 mg/mL.

Nanoparticles characterization by DLS and Absorption spectroscopy

DLS analysis were performed by means of Malvern Zetasizer Nano-ZS on aqueous solution of PDA-TiO_2@Pluronic F-127 nanoparticles with a concentration 0.2 mg/mL calculated on TiO_2 quantity. Absorption spectroscopy was performed on a Perkin Elmer Lambda 650 spectrophotometer on solution with TiO_2 concentration 0.2 mg/mL.

RhB photodegradation tests

RhB photodegradation test was performed by irradiating the TiO_2-Melanin solution in presence of RhB $1x10^{-6}$ M. A medium pressure Hg lamp at 365 nm (wavelength selected by a bandpass filter) was used. Absorption spectra were collected during the irradiation and the degradation was observed by monitoring the decrease of Rhodamine B maximum (555nm). Tests were performed also on samples without Rhodamine, to see if melanin would have been degraded.

3.3.2. Results

TiO_2 colloidal nanosystems developed and studied in section 3.2 are prepared and stable at acidic pH. Indeed, whether the pH increases aggregation of the system starts to occur. In particular, going gradually from acidic to neutral pH leads to visible aggregation and precipitation, while if the pH of the solution is directly brought from acidic to alkaline, there are no precipitation phenomena, but the size and the polydispersity of the nanoparticles increases. However, it would be very

useful for the real application to stabilize and study TiO_2 nanoparticles in other pH conditions. In this part of my PhD, we managed to stabilize TiO_2@Pluronic F-127 nanoparticles, the most stable ones among the previously described systems (1.2.1 "TiO_2 colloidal nanosystems: synthesis, characterization, and photocatalytic activity"), with melanin.

Melanins are pigments of diverse structure and origin that result from the enzymatic oxidation and polymerization either of tyrosine in animals or of phenolic derivatives in other organisms[20-22].Different kind of melanin are present in nature, such as eumelanin and pheomelanin. The synthetic analogue of eumelanin is usually obtained by Dopamine or L-Dopa and it is called Polydopamine (PDA). Even though the synthetic pathway of PDA differs from the one of natural melanin, PDA displays optical, electronic and magnetic properties identical to those of natural eumelanin being characterized also by excellent biocompatibility. Additionally, PDA owns many functional groups, such as catechol, amine, and imine, that can either covalently bind or non-covalently load through π-π stacking, hydrogen bonding, van der Waals forces, etc., and different active agents. With these benefits, PDA can be used for a wide range of application acting as coating material, as carrier or as the active component for bio-application[23].

L-Dopa oxidation and subsequent polymerization is favoured at alkaline pH[24] and exploits the oxygen present in the air. The polymerization pathway is reported in Figure 1.

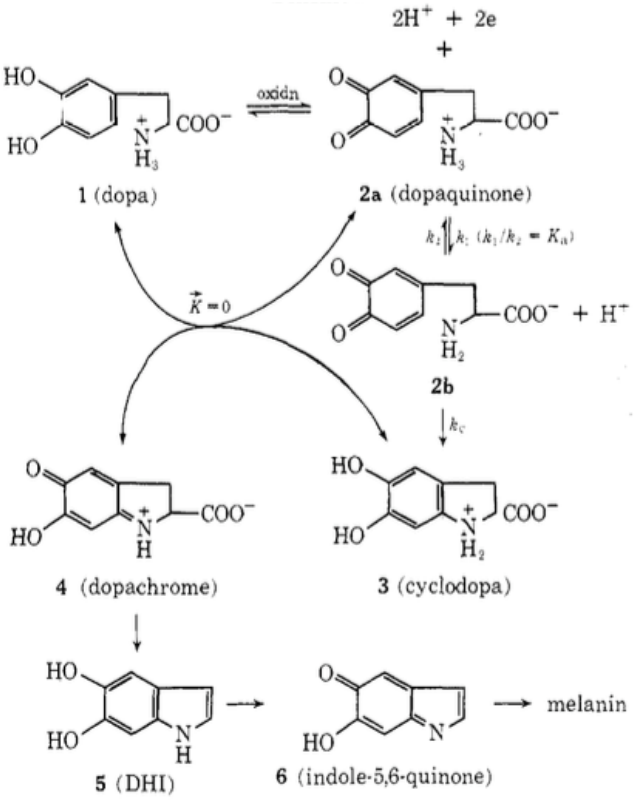

Figure 1: polymerization pathway of melanin formation from L-Dopa oxidation, reproduced from ref[25]

As Figure 1 shows, there are many intermediates during the oxidation-polymerization of eumelanin from L-DOPA. The first intermediated to be formed is Dopaquinone that, after a step of rearrangement and oxidation forms Dopachrome. Then, the building blocks of the polymerization are formed such as Dihydroxyindole (DHI) and Indolequinone. Their polymerization then leads to the formation of melanin.

Different polymerization mechanisms are suggested but so far, little experimental evidence has been reported. In general, it seems that PDA is composed by the coexistence of supramolecular structures in which unpolymerized dopamine is self-assembled with its main oxidative products and covalent-bonded oxidative polymerization products[26].

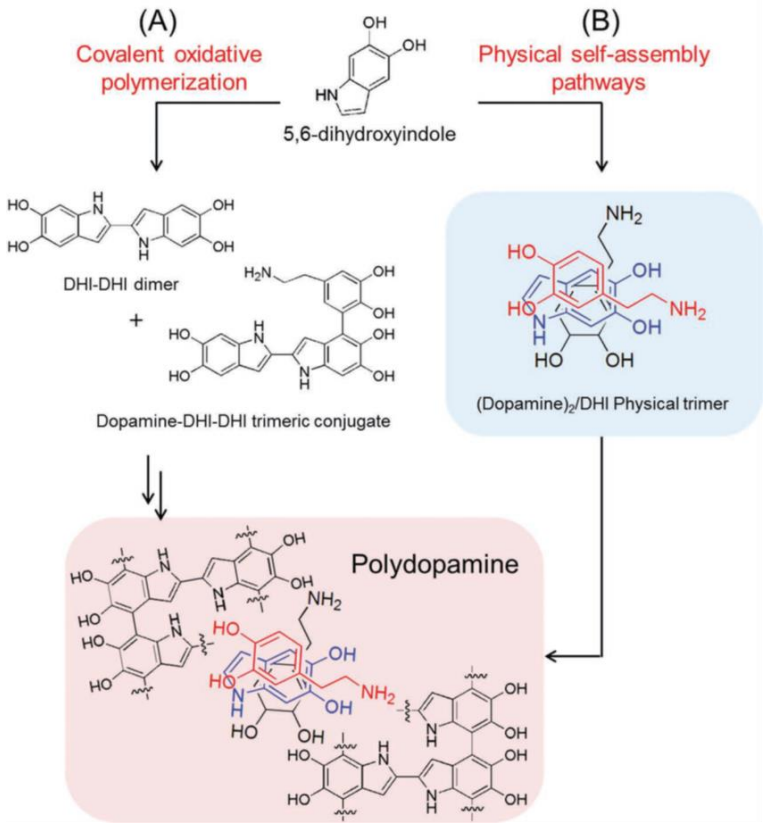

Figure 2: PDA possible polymerization mechanisms from dopamine oxidation, reproduced by ref[26].

In this work, L-Dopa oxidation and polymerization process was performed in presence of TiO_2@Pluronic F127. L-Dopa was added to the colloidal TiO_2 nanoparticles dispersion in acidic conditions (pH almost 3). Then, NaOH was added in order to achieve a pH value of almost 9 and thus induce the L-Dopa reaction. First, our interest was to understand if TiO_2 could be stabilized by melanin at alkaline pH and also if TiO_2 had a role in the oxidation mechanism of L-Dopa. Thus,

the PDA-TiO_2 system was characterized by DLS (Table 1) and Absorption spectroscopy (Figure 3) and it was compared to TiO_2@Pluronic F-127 at acidic and alkaline pH.

	Z-Average (nm)	PDI
PDA-TiO_2@Pluronic F-127 (pH 9.5)	38	0.228
TiO_2@Pluronic F-127 (pH 9.5)	100	0.425
TiO_2@Pluronic F-127 (pH 3)	23	0.175

Table 1: DLS measurements of PDA-TiO_2@Pluronic F-127, prepared at pH 9.5, compared with TiO_2@Pluronic F-127 at pH 3 and at pH 9.5.

DLS analysis highlights the difference between TiO_2 colloidal nanoparticles with and without PDA modification at alkaline pH. TiO_2@Pluronic F-127 aggregates at alkaline pH, going from a size of 23 nm to a size of 100 nm, and has a high polydispersity index that denotes a lack of stability. Modification with PDA lead to a stabilization of the TiO_2 nanoparticles in alkaline environment. Indeed, nanoparticles have a size of almost 40 nm and a good size distribution. The 40 nm size is still higher with respect to the one of TiO_2@Pluronic F-127 at acidic pH and it can be due both to a contribute of melanin to the size of the particle and to a partial aggregation that cannot be totally avoided.

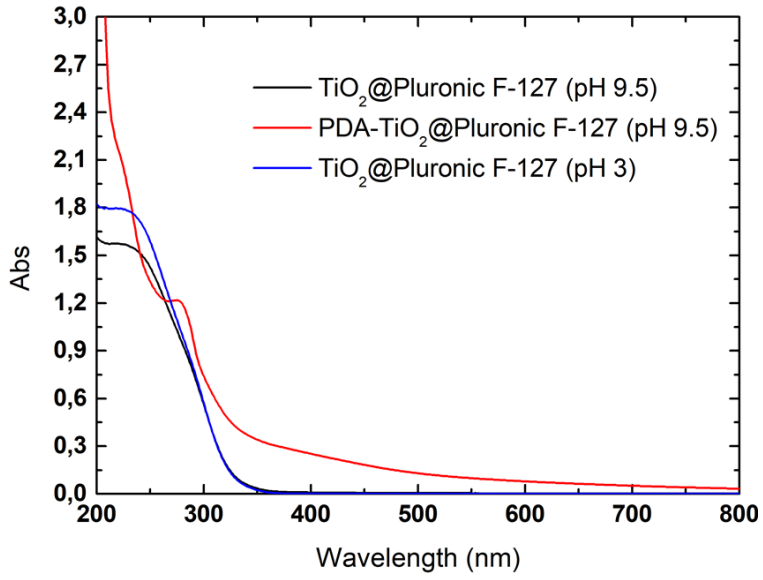

Figure 3: Absorption spectra of PDA-TiO_2@Pluronic F-127, prepared at pH 9.5, compared with TiO_2@Pluronic F-127 at pH 3 and at pH 9.5.

In the absorption spectra of Figure 3 TiO_2@Pluronic F-127 (pH 9.5) has a lower absorption intensity with respect to TiO_2@Pluronic F-127 (pH 3). This is expected because of TiO_2 aggregation visible also by DLS analysis. Unfortunately, given the high Dopa concentration, in PDA-TiO_2@Pluronic F-127 it is not possible to clearly observe TiO_2 peak that is under the polydopamine band. Observing the peaks and comparing them with the literature[27], the peak at almost 300 nm could belong to a polydopamine formation intermediate, for example Dopachrome that has a peak at 302 nm, or also to a polydopamine oligomer. In order to study TiO_2 effect on polydopamine polymerization absorption spectroscopy was performed on PDA- TiO_2@Pluronic F-127 each 5 minutes after the beginning of the L-Dopa oxidation (corresponding to the change of pH to 9.5) and compared to L-Dopa oxidation process in the same conditions but without TiO_2 nanoparticles in the solution (Figure 4).

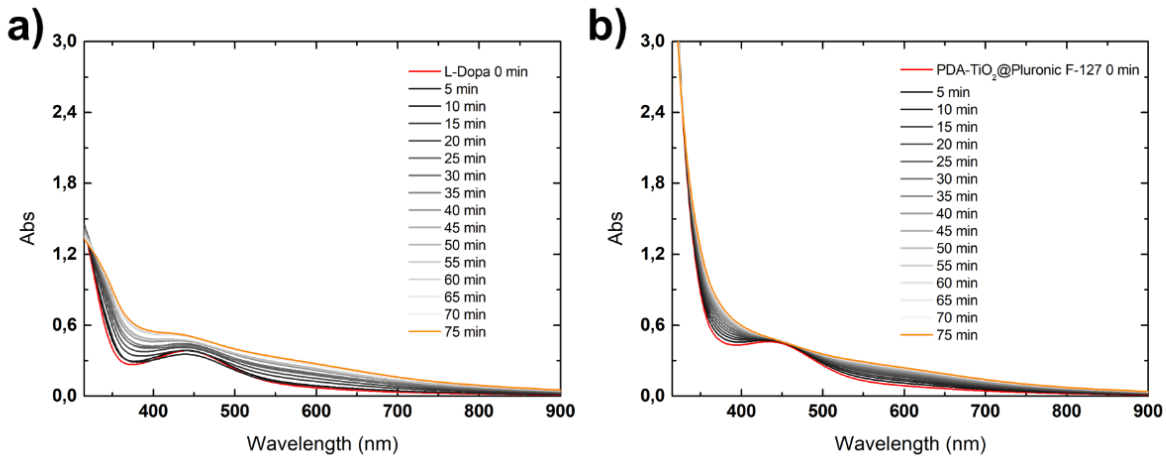

Figure 4: absorption spectra of L-Dopa aqueous solution at pH 9.5 (a) and PDA- TiO_2@Pluronic F-127 aqueous solution at pH 9.5 (b) collected every 5 minutes.

Absorption spectra in Figure 4 show the change in the absorption band during the formation of melanin typical broadband monotonic absorbance in all the UV-Visible up to near-infrared (NIR) range[28]. Recent investigation of the electronic properties of synthetic melanin based on ultrafast transient absorption (UF-TA) spectroscopy revealed that this broadband is given by the presence of a subset of chemically heterogeneous chromophores[29]. Indeed, this can be in accordance with the hypothesized structure of melanin that is made by aggregation of different oligomers. At the beginning of the reaction a peak at almost 440 nm is observed in both the samples. This peak can be attributed to an intermediate of melanin formation. In particular, this peak can be attributed to Dopachrome (usually having a peak at 434 nm in alkaline conditions[27] or a π conjugation in a Dihydroxiindole (DHI) polymer[30]. Both in the sample with and without TiO_2 nanoparticles the process of Melanin formation is analogous in terms of absorption band shape. Absorbance at 600

nm was considered, in order to be sure that no absorption of TiO_2 was present and that the increase was only due to melanin polymerization; absorbance variation at 600 nm was monitored in time, obtaining trends in Figure 5.

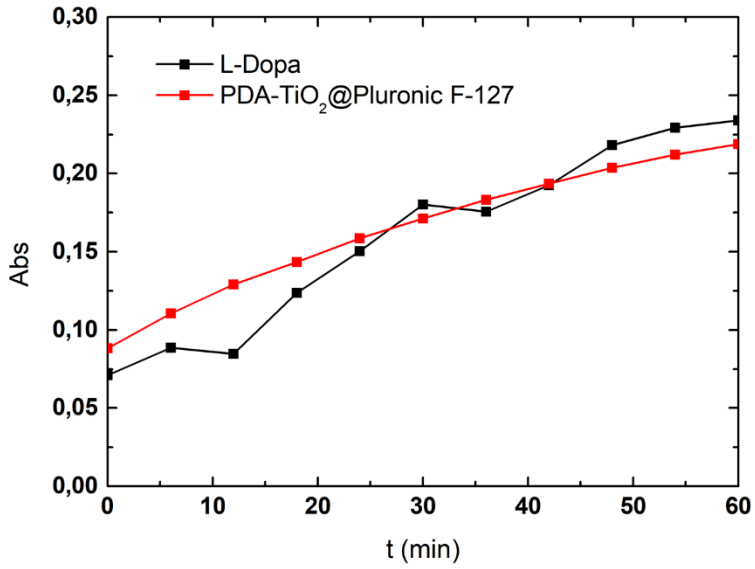

Figure 5: absorbance increase at 600 nm during L-Dopa polymerization reaction with (red) and without (black) TiO_2 nanoparticles in solution.

Figure 5 shows a change in the polymerization pathway of melanin in presence or not in presence of TiO_2 nanoparticles. In particular, even if the rate of absorbance increase is very similar between the two samples, it has to be noticed that the melanin absorbance increase of L-Dopa oxidation is more irregular with respect to the one of PDA-TiO_2@Pluronic F-127. This suggests that, in presence of TiO_2 there is an interaction between TiO_2 and L-Dopa and/or intermediates of PDA formation that lead to a certain control in the polymerization reaction. The interaction is observed also in DLS analysis (Table 1) but further investigation needs to be conducted on the precise influence of this interaction in melanin formation. The nature of this interaction can be due to the presence of the catechol group in L-Dopa that could bond with TiO_2 surface.

PDA-TiO_2@Pluronic F-127 solutions were left drying in different conditions, to obtain different pigments and check the stability of these powders after re-dissolution. During oxidation reactions, the L-Dopa solution goes from a light-yellow colour to orange and dark brown when the polymerization is complete (Figure 6).

Figure 6: Melanin formation steps in PDA-TiO_2@Pluronic F-127

Drying the solution at different steps of the polymerization reaction can lead to powders of different colours. PDA-TiO_2@Pluronic F-127 solutions were dried by heating (samples "Heat") or lyophilization (samples "Lyo"), right after the beginning of polymerization (addition of the base) and after 24 hours, when the polymerization was complete. The lyophilised samples, as expected, were dark brown and orange respectively for lyophilization at the beginning of the reaction (Lyo0) and lyophilization after 24 hours (Lyo24). For the samples heated the colour was dark brown/black for both the conditions (Heat0 and Heat24). This means that the process of drying does not stop the polymerization reaction that continues to occur, leading to the typical brown colour also in the case of heating after base addition. This kind of results can be obtained also treating L-Dopa solution without TiO_2 in the same way. However, in the case of PDA-TiO_2@Pluronic F-127 heated after 24 hours a surprising result come out. Indeed, while in the other cases a powder is obtained after the drying process, in Heat24 black fibres form (Figure 7).

Figure 7: sample Heat24, obtained by heating after 24 hours from the melanin formation reaction in sample PDA-TiO_2@Pluronic F-127.

The reason why these fibres are formed surely depends on TiO_2 nanoparticles interaction with melanin, but more investigation is needed to deeply understand the mechanism by which this process occurs. At this point the powders were dissolved in water, to understand if a stabilization of the TiO_2 nanoparticles is maintained even after a drying process. Indeed, it could be very advantageous to have a solid material that can be dispersed in water in form of nanoparticles and this could not be achieved simply with TiO_2 colloidal nanosystems, that were stable only in acidic solution. All the samples but Lyo0 dissolved after 5 hours of vigorous stirring. All the samples were then characterized by DLS (Table 2) and absorption spectroscopy (Figure 8).

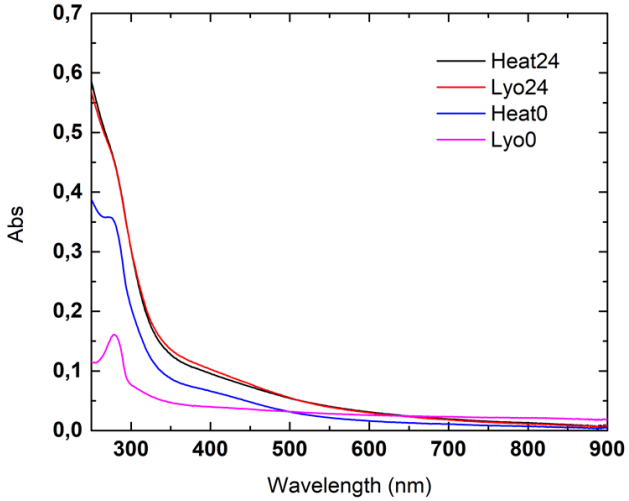

Figure 8: Absorption spectra of PDA-TiO_2@Pluronic F-127 dried in different conditions and re-dissolved in water.

	Z-Average	PDI
Heat24	42	0.4
Heat0	113	0.5
Lyo24	44	0.4
Lyo0	411	0.5

Table 2: DLS analysis of PDA-TiO_2@Pluronic F-127 dried in different conditions and re-dissolved in water.

Figure 8 shows that spectra shapes and absorbances are similar for Heat24 and Lyo24 which are respectively the samples dried by heating and lyophilization after 24 hours. In these samples, melanin and TiO_2 concentration is the same. This means that the processes by which they have been dried did not influence the melanin formation and the TiO_2 particles aggregation. This

hypothesis can be confirmed also by the DLS data, which show 40 nm nanoparticles in the case of Heat24 and Lyo24 while bigger aggregates are present in the sample treated at the beginning of the reaction. Instead, Heat0 and Lyo0, dried respectively by heating and lyophilization show different shapes and absorbances. The absorbance corresponding to the melanin band is not as intense as in Heat24 and Lyo24 and a peak at almost 270 nm is observed, that is attributed to L-Dopa or to melanin formation intermediates. This can be expected because both the solutions have been dried at the beginning of the reaction, in which the melanin did not form completely. The difference in the spectra of Heat0 and Lyo0 highlights that the heating process let the reaction proceed more than the lyophilization, since Lyo0 spectrum can be attributed to an earlier phase of the process than Heat0, because in the latter melanin typical band is more visible.

The absorbance corresponding to TiO_2 band (not clearly visible but part of the band below 300 nm) is also less intense in Heat0 and Lyo0 than Heat24 and Lyo24. This can mean that in the solutions dried at the beginning of the reaction lead TiO_2 to aggregate. This event seems not to happen in the case of Heat24 and Lyo24, in which DLS shows the presence of nanoparticles rather than bigger aggregates. This means that melanin, rather than reaction intermediates of melanin formation, contribute to the stabilization of TiO_2 and maintain it in form of nanoparticles even after drying and re-dissolution. DLS measurements on PDA-TiO_2@Pluronic F-127 nanoparticles re-dissolved in water were performed also one day and 6 days after the re-dissolution to check their stability (Table 3). Lyo0 was totally precipitated after one day and Heat0 was precipitated after 6 days, thus DLS monitoring for Heat24 and Lyo24 are reported (Table 3).

	After one day from dissolution		After six days from dissolution	
	Z-Average	PDI	Z-Average	PDI
Heat24	37	0.3	24	0.2
Lyo24	40	0.3	33	0.3

Table 3: DLS results of Heat24 and Lyo24 one day and six days after the re-dissolution

Samples dried after 24 hours from the beginning of the oxidation reaction of L-Dopa have a completely different behaviour with respect to samples dried before the complete polymerization of L-Dopa. Indeed, while the latter once re-dissolved in water are unstable in time, nanoparticles of Heat24 and Lyo24 increase their stability in time. Indeed, DLS shows that the nanoparticles dimension and the polydispersity index decrease. Therefore, by modifying TiO_2 colloidal nanoparticles with melanin, we managed to obtain nanoparticles stable in alkaline pH and that

can be dried and re-dissolved without a radical change in their aggregation properties. This can be very useful as a storage method for these photocatalyst. Having verified the nanoparticles stability, we tried to study them by changing the pH of the solution. In particular, we focused on the sample Heat24 which is the most stable and small sized one. The dissolution of Heat24 in water leads to a pH value of 8, thus we monitored their stability by bringing the pH at 7 and at 5. DLS analysis was performed in these conditions after one day, two days and six days (Table 4).

	pH 7		pH 5	
	Z-Average	PDI	Z-Average	PDI
As prepared	30	0.2	31	0.3
1 day after	30	0.2	32	0.3
2 days after	30	0.2	32	0.3
6 days after	30	0.2	32	0.3

Table 4: DLS analysis performed on Heat24 nanoparticles solution at pH 7 and at pH 5 after 1 day, 2 days and 6 days after the dissolution of the fibers of PDA-TiO_2@Pluronic F-127

DLS shows a very good stability of the Heat24 nanoparticles both at pH 7 and pH 5. Furthermore, at different pH values also the nanoparticles size is maintained with a good polydispersity index (PDI).

Photocatalytic activity of PDA-TiO_2@Pluronic F-127 nanoparticles (Heat24 samples) stabilized at pH 7 and pH 5 was also studied. Degradation of Rhodamine B was performed by monitoring its absorbance decrease during irradiation (as explained in section 3.2.2 – Figure 5). Rhodamine B degradation trend was also compared to irradiation of samples without Rhodamine, to monitor if irradiation led to melanin modifications (Figure 9).

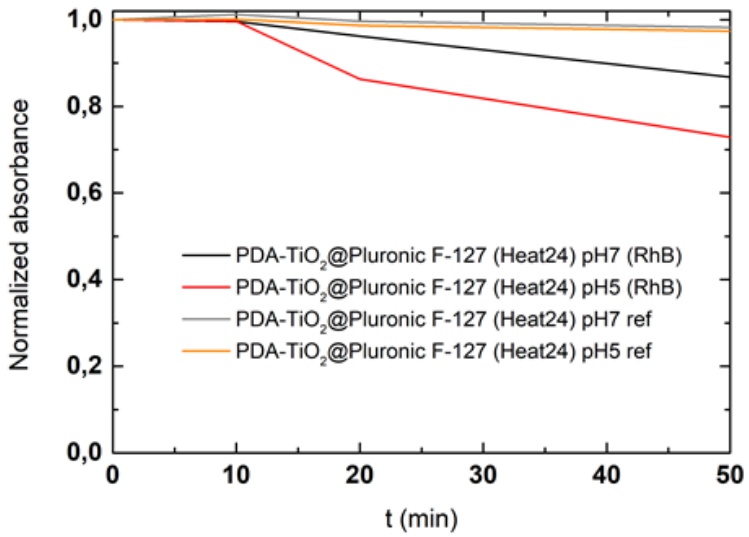

Figure 9: Rhodamine B degradation by PDA-TiO_2@Pluronic F-127 nanoparticles stabilized at pH 7 and pH 5, during irradiation at 365 nm. Comparison also with reference (ref) samples without Rhodamine B.

Figure 9 shows that pH conditions lead to a difference in TiO_2 reactivity. Indeed, while at pH 7 only almost the 10% of Rhodamine B is degraded, twice of it is degraded at pH 5. Irradiation of the nanoparticles without Rhodamine show that melanin, which also absorbs at 550 nm, the wavelength at which the absorbance of Rhodamine b is considered for the degradation (1.2.1 "TiO_2 colloidal nanosystems: synthesis, characterization, and photocatalytic activity"- Figure 5), does not display any modification with TiO_2 activation. Not a lot of quantity of Rhodamine B is degraded, but it has to be considered that, in this case, the irradiation wavelength was at 365 nm, in which TiO_2 does not have a high absorbance. Therefore, further investigation at other wavelengths need to be performed in order to confirm and observe a more significative result.

3.3.3. Conclusions

TiO_2 nanoparticles were modified with Melanin by the polymerization reaction of L-Dopa in presence of TiO_2@Pluronic F-127 (PDA-TiO_2@Pluronic F-127). Polydopamine (PDA) formation is controlled and stabilized by TiO_2 nanoparticles, that seem to act as templates. Indeed, because of the interaction between PDA and TiO_2, nanoparticles are stabilized also at alkaline pH, while TiO_2 colloidal dispersions are usually stable only at acidic pH (pH 3). Furthermore, it was possible to dry PDA-TiO_2@Pluronic F-127 obtaining either powder or fibres depending on the drying method. Here nanoparticles are preserved and re-obtained once the powder is dissolved in water. Furthermore, nanoparticles are stable in time and with pH change, so that it is possible to stabilize them both at alkaline, neutral, and slightly acidic pH. The PDA-modified TiO_2 nanoparticles also

show an interesting photocatalytic activity which varies with pH that deserves deeper investigation. Thus, melanin modification of TiO_2 photocatalyst allowed the development of a new interesting system stable at different pH values and that can maintain its properties also after drying and re-dissolving processes, offering also a good storage method for these photocatalysts that can in principle be removed from the solution and re-used more easily.

3.4. Cementitious photocatalytic coatings: study of aging effects

3.4.1. Materials

LAG10S photocatalyst preparation

LAG10S photocatalyst was prepared adding G2Nan paste purchased by Nanesa (4% dry graphene like matter) and TiO_2 powder (AHP200 from Sachtleben Chemie with average surface area of 160-240 m^2/g and anatase purity>90%) to water to produce an aqueous slurry, in the ratio TiO_2/G2Nan(w/w) dry matter 10:1. The slurry was then mixed in a laboratory blender at 11000 rpm for 40 minutes and was dried at 60°C. Then the obtained powder was sonicated for 4 hours in 2-propanol and subsequently dried at 60°C.

Mortar sample preparation

The fresh cementitious mixture is mortar prepared according to the procedure described in the standard UNI EN 196-1 and replacing part of the cement with the photocatalyst. All the photocatalytic compounds were incorporated in a binder matrix: white cement i.design Italbianco 52.5R. The following composition were used: 1 part of cement binder, 3 parts of sand, 0.5 parts of water, 0.36%w/w (with respect of the binder) of cellulose and the photocatalyst (1.5%w/w of TiO_2 content with respect of the binder). The fresh mortar was poured into the lid of a Petri capsule and maintained in a conditioned room at 20°C and 90% relative humidity (RH) for 7 days. Then the sample was left at 20°C and 60% of RH for all the time before the measurement.

NOx abatement method

The photocatalytic activity of TiO_2 photocatalyst in incorporated cement-based materials was evaluated by NOx abatement adopting the recirculation procedure. The gas flow method is compared using the apparatus reported in the Italian standard UNI 11247 that describes a method aimed at assessing the index of photocatalytic abatement due to the action of inorganic materials. The sample to be investigated was collocated inside a reaction chamber containing an irradiation system that provides an average irradiance (in UV-A band) of (20±1) W/m^2 on the specimen surface (64cm^2) during the test. The irradiation source is a Mercury lamp Radium Sanolux HRC 300-280 E27 UV-lamp, with an irradiance (I) both in UVA (280nm- 315nm; I=3W/m2 at 0.5m) and UVB (315nm- 400nm; I=13.6W/m^2 at 0.5m). In the UV (λ<400 nm) irradiance spectrum the main component is the 365 nm line signal brought by the presence of mercury inside of the lamp

(according the standard UNI 11247 irradiance integrated at λ <350 nm is forecast to be 10% lower than the irradiance integrated between 350 and 400 nm). In the standardized continuous flow procedure according to UNI 11247, the flow of polluted air containing 0.55ppm of NOx (of which NO_2=0.15ppm and NO=0.4ppm) was constant (1.5 litre/min). The first phase of the test was performed in dark conditions and it was necessary to equalize the adsorption processes and to achieve a constant gas flow and NOx concentration. During this first phase in dark conditions, the concentration of the gas entering and leaving the reactor is constantly measured. When the concentration of the outlet gas from the reactor is stable, the second phase of the test starts the lamp is switched on. At this stage, the system is allowed to balance for a certain time to reach an equilibrium gas concentration.

3.4.2. Results

This part of my PhD was performed in the European Project Graphene Flagship Core 2. The role of our group in the project was focused on the development of photocatalytic cementitious coatings for air remediation. The use of TiO_2 as photocatalyst in this field is already exploited[31] and our aim was to improve photocatalytic performance of TiO_2 in order to obtain a material that could efficiently work in the real conditions, thus with light and pollution variations, and that could be suitable for industrial applications. The increase of the photocatalytic behaviour of TiO_2 can be enhanced by its modification with 2D materials such as graphene and transition metal dichalcogenides. In the first part of the project (Core 1) several TiO_2 photocatalytic cementitious coatings modified by 2D materials were studied and tested for degradation of inorganic pollutants (NOx) and organic pollutants (Rhodamine B). At first, tests on powder or powder dispersions were always performed. The various photocatalysts were then implemented in several cementitious matrixes with different chemical compositions and physical properties. Testing all these materials in several matrixes allowed to choose the best TiO_2-based photocatalyst in term of efficiency, costs, and industrial scalability. Among all the studied materials, a TiO_2:Graphene 10:1 material (called LAG10S) was chosen as the best photocatalytic coating for cement matrixes in outdoor applications. In the second part of the project (Graphene Flagship Core 2) aging of this photocatalyst during several irradiation cycles was investigated.

LAG10S photocatalysts is prepared by an easy, low cost and scalable procedure in which first an aqueous slurry with TiO_2 and pre-exfoliated graphite is mixed in a blender for 40 minutes. After drying at 60°C, the obtained powder is further sonicated in 2-propanol for 4 hours and dried again at 60°C. Mixing in the blender allows to exfoliate graphite by means of shear forces and a following step of sonication further enhances TiO_2-Graphene interaction. After the characterization of the LAG10S powder by XRD, UV-Vis spectroscopy and SEM, it was embedded in cement matrix, by

replacing a part of the mortar prepared cementitious mixture by the photocatalyst (standard UNI EN 196-1) (Figure 1).

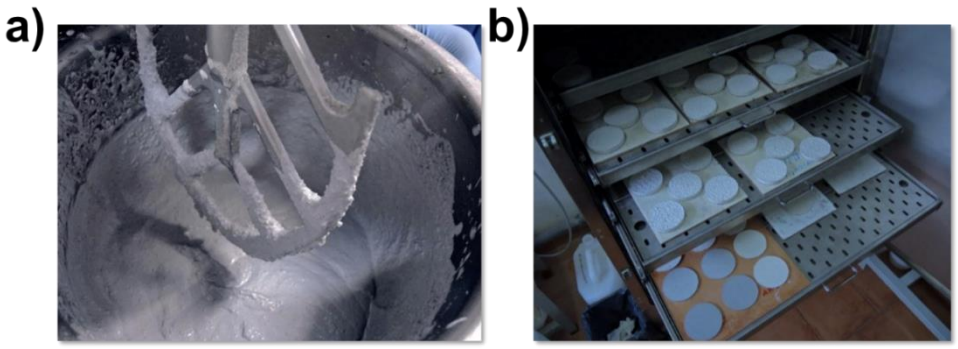

Figure 1: a) preparation of cementitious mixture in presence of the photocatalyst by mortar. b) deposition of the cementitious mixture in petri dishes, where it is left drying for 7 days at 20°C and 90% of relative humidity and then at 20°C and 60% of relative humidity.

Aging effect of LAG10S embedded in cement matrix was investigated by performing several irradiation cycles for NOx abatement as model of inorganic pollutants in air. Evaluation of NOx abatement was performed using a NOx reaction chamber. The sample (cement dish – Figure 1-b) is irradiated by a solar simulator lamp with an irradiance both in UVA and UVB. A constant flux of polluted air (NOx) flows inside the chamber in order to reproduce the real condition of pollutants refreshing.

Aging effects on LAG10S were tested by 30 cycles of irradiation of the cement sample. Each cycle was characterized by 40 minutes in dark (lamp switched off) and 40 minutes in irradiation (lamp switched on). Photocatalytic activity was evaluated by detecting the NOx flux variations during all the process (Figure 2).

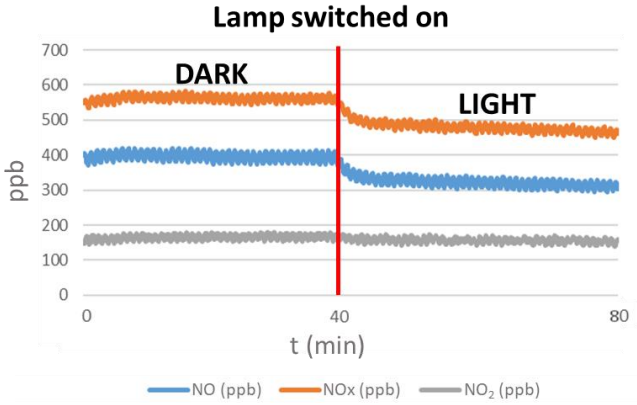

Figure 2: NOx flux variation during 1 cycle of irradiation (40 minutes of dark followed by 40 minutes of irradiation).

Monitoring the NOx flux, the abatement percentage of NOx for each cycle can be calculated, considering the flux variation between the dark and the irradiation parts of the cycle, as written in Eq.1.

$$Abatement\ \% = \frac{X(dark) - X(light)}{X(dark)} \cdot 100 \qquad \text{Eq.1}$$

Where X(dark) and X(light) are respectively the average value of NO, NO_2 or total NOx concentration during the dark and during the irradiation parts of the cycle. Based on the abatement percentage calculated for each cycle it is possible to obtain a trend of NOx degradation during all the cycles. First, the photocatalytic activity was monitored for 30 cycles of irradiation (Figure 3) in samples with 1% and 3% of photocatalyst, calculated on cement quantity.

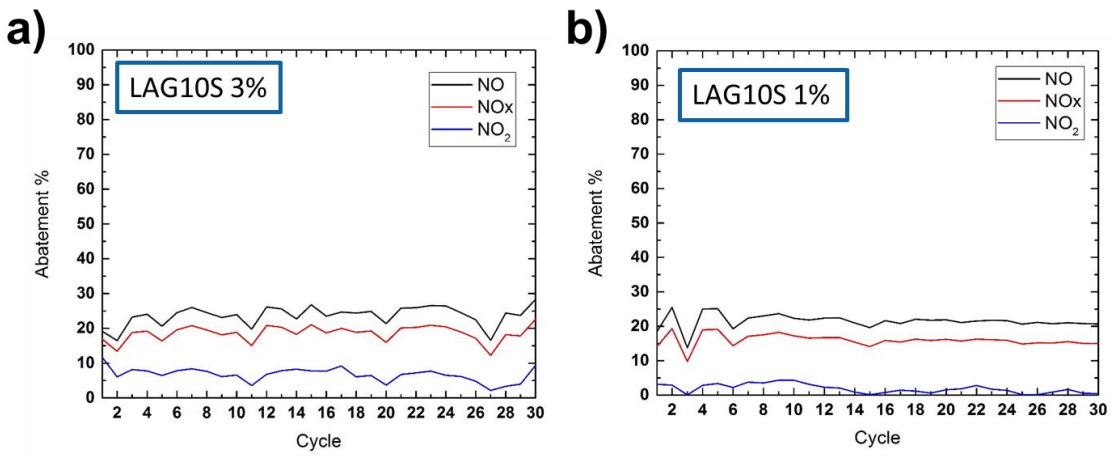

Figure 3: trend of photocatalytic NOx abatement by LAG10S embedded in cement matrix at 3% (a) and at 1% (b).

As Figure 3 reports, there is not a significative decrease in NOx degradation during the 30 cycles of irradiation. Thus, the photocatalyst is resistant to aging for both the 1% and the 3% dosages. The abatement percentage mediated on all the 30 cycles were calculated and reported in Table 1.

	Average abatement % during 30 cycles of irradiation for LAG10S 3%	Average abatement % during 30 cycles of irradiation for LAG10S 1%
NO	(24±2)%	(21±1)%
NO_2	(7±2)%	(2±1)%
NOx	**(19±2)%**	**(16±1)%**

Table 1: total NOx abatement percentage calculated on 30 cycles for LAG10S 3% and LAG10S 1%

LAG10S 3% photocatalytic activity was also tested for 60 cycles of irradiation and also in this case there is not a significative variation of photocatalytic performance in NOx degradation (Figure 4).

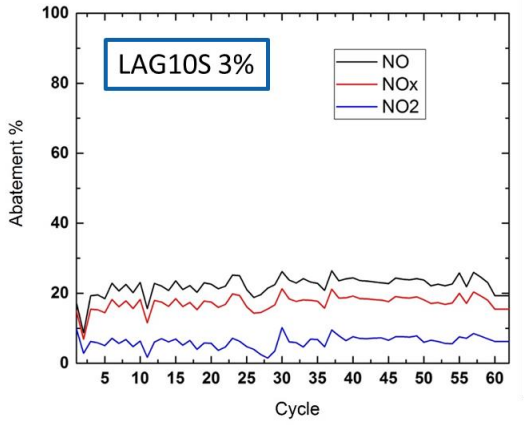

Figure 4: trend of photocatalytic NOx abatement by LAG10S embedded in cement matrix at 3% during 60 cycles of irradiation

	Average abatement % during 60 cycles of irradiation for LAG10S 3%
NO	(23±2)%
NO_2	(6±2)%
NOx	**(17±2)%**

Table 2: total NOx abatement percentage calculated on 60 cycles for LAG10S 3%

As expected, Table 2 shows almost the same average abatement percentage of NOx abatement in the previous cases. Therefore, LAG10S photocatalyst embedded in a cement matrix denotes a very

high resistance to aging effects due to prolonged and periodic light irradiation and continuous refresh of the pollutants on the photocatalytic surface.

3.4.3. Conclusions

TiO_2 based photocatalytic cementitious coatings were studied for air remediation, by irradiation in presence of NOx gases or by staining Rhodamine B on the cement surface respectively models for inorganic and organic pollutants. In order to enhance TiO_2 photocatalytic performances, already studied for application in cementitious coatings, modification with Graphene and Graphene related materials were developed. Among the various photocatalysts studied, a coating with TiO_2:Graphene 10:1, called LAG10S was chosen as the most performing one. Indeed, this photocatalyst gave very good results and it represent a suitable candidate for application in cement industry because its preparation involves low-cost materials and is easily scalable. Aging effect of this photocatalyst embedded in cement matrix was evaluated for inorganic pollutants degradation. In particular, the performances of these photocatalytic cements were monitored during several irradiation cycles and by a continuous refresh of NOx gases on the surface. LAG10S embedded in cement showed unchanged photocatalytic performances after 30 and 60 irradiation cycles, denoting a great resistance.

3.5. Bibliography

1. Fujishima, A.; Zhang, X. T.; Tryk, D. A., TiO2 photocatalysis and related surface phenomena. *Surface Science Reports* **2008,** *63* (12), 515-582.

2. Chen, X.; Mao, S. S., Titanium dioxide nanomaterials: Synthesis, properties, modifications, and applications. *Chemical Reviews* **2007,** *107* (7), 2891-2959.

3. Pan, X. Y.; Yang, M. Q.; Fu, X. Z.; Zhang, N.; Xu, Y. J., Defective TiO2 with oxygen vacancies: synthesis, properties and photocatalytic applications. *Nanoscale* **2013,** *5* (9), 3601-3614.

4. Macwan, D. P.; Dave, P. N.; Chaturvedi, S., A review on nano-TiO2 sol-gel type syntheses and its applications. *Journal of Materials Science* **2011,** *46* (11), 3669-3686.

5. Salinaro, A.; Emeline, A. V.; Zhao, J. C.; Hidaka, H.; Ryabchuk, V. K.; Serpone, N., Terminology, relative photonic efficiencies and quantum yields in heterogeneous photocatalysis. Part II: Experimental determination of quantum yields (technical report). *Pure and Applied Chemistry* **1999,** *71* (2), 321-335.

6. https://www.who.int/airpollution/en/. https://www.who.int/airpollution/en/.

7. Hoffmann, M. R.; Martin, S. T.; Choi, W. Y.; Bahnemann, D. W., Environmental applications of semiconductor photocatalysis. *Chemical Reviews* **1995,** *95* (1), 69-96.

8. Liang, Y. Y.; Wang, H. L.; Casalongue, H. S.; Chen, Z.; Dai, H. J., TiO_2 Nanocrystals Grown on Graphene as Advanced Photocatalytic Hybrid Materials. *Nano Research* **2010,** *3* (10), 701-705.

9. Serpone, N.; Lawless, D.; Khairutdinov, R., Size effects on the photophysical properties of colloidal anatase TiO_2 particles - size quantization or direct transitions in this indirect semiconductor. *Journal of Physical Chemistry* **1995,** *99* (45), 16646-16654.

10. Chaves, A.; Azadani, J. G.; Alsalman, H.; Da Costa, D. R.; Frisenda, R.; Chaves, A. J.; Song, S. H.; Kim, Y. D.; He, D.; Zhou, J.; Castellanos-Gomez, A.; Peeters, F. M.; Liu, Z.; Hinkle, C. L.; Oh, S.-H.; Ye, P. D.; Koester, S. J.; Lee, Y. H.; Avouris, P.; Wang, X.; Low, T., Bandgap engineering of two-dimensional semiconductor materials. *npj 2D Materials and Applications* **2020,** *4* (1).

11. Wang, H. X.; Wang, Q.; Zhou, K. G.; Zhang, H. L., Graphene in Light: Design, Synthesis and Applications of Photo-active Graphene and Graphene-Like Materials. *Small* **2013,** *9* (8), 1266-1283.

12. Han, L.; Wang, P.; Dong, S. J., Progress in graphene-based photoactive nanocomposites as a promising class of photocatalyst. *Nanoscale* **2012,** *4* (19), 5814-5825.

13. Zhang, N.; Zhang, Y. H.; Xu, Y. J., Recent progress on graphene-based photocatalysts: current status and future perspectives. *Nanoscale* **2012,** *4* (19), 5792-5813.

14. Tu, W. G.; Zhou, Y.; Zou, Z. G., Versatile Graphene-Promoting Photocatalytic Performance of Semiconductors: Basic Principles, Synthesis, Solar Energy Conversion, and Environmental Applications. *Advanced Functional Materials* **2013,** *23* (40), 4996-5008.

15. Leary, R.; Westwood, A., Carbonaceous nanomaterials for the enhancement of TiO_2 photocatalysis. *Carbon* **2011,** *49* (3), 741-772.

16. Xiang, Q. J.; Yu, J. G.; Jaroniec, M., Graphene-based semiconductor photocatalysts. *Chemical Society Reviews* **2012,** *41* (2), 782-796.

17. Baldi, G.; Bitossi, M.; Barzanti, A. Method for the preparation of aqueous dispersions of TiO_2 in the form of nanoparticles, and dispersions obtainable with this method. US8431621B2, **2013**.

18. Natarajan, T. S.; Thomas, M.; Natarajan, K.; Bajaj, H. C.; Tayade, R. J., Study on UV-LED/TiO_2 process for degradation of Rhodamine B dye. *Chemical Engineering Journal* **2011,** *169* (1-3), 126-134.

19. Wu, T. X.; Liu, G. M.; Zhao, J. C.; Hidaka, H.; Serpone, N., Photoassisted degradation of dye pollutants. V. Self-photosensitized oxidative transformation of Rhodamine B under visible light irradiation in aqueous TiO_2 dispersions. *Journal of Physical Chemistry B* **1998,** *102* (30), 5845-5851.

20. d'Ischia, M.; Wakamatsu, K.; Cicoira, F.; Di Mauro, E.; Garcia-Borron, J. C.; Commo, S.; Galvan, I.; Ghanem, G.; Kenzo, K.; Meredith, P.; Pezzella, A.; Santato, C.; Sarna, T.; Simon, J. D.; Zecca, L.; Zucca, F. A.; Napolitano, A.; Ito, S., Melanins and melanogenesis: from pigment cells to human health and technological applications. *Pigment Cell & Melanoma Research* **2015,** *28* (5), 520-544.

21. Hurbain, I.; Geerts, W. J. C.; Boudier, T.; Marco, S.; Verkleij, A. J.; Marks, M. S.; Raposo, G., Electron tomography of early melanosomes: Implications for melanogenesis and the generation of fibrillar amyloid sheets. *Proceedings of the National Academy of Sciences of the United States of America* **2008,** *105* (50), 19726-19731.

22. Wasmeier, C.; Hume, A. N.; Bolasco, G.; Seabra, M. C., Melanosomes at a glance. *Journal of Cell Science* **2008,** *121* (24), 3995-3999.

23. Liu, Y. L.; Ai, K. L.; Lu, L. H., Polydopamine and Its Derivative Materials: Synthesis and Promising Applications in Energy, Environmental, and Biomedical Fields. *Chemical Reviews* **2014,** *114* (9), 5057-5115.

24. Zhou, Y. Z.; Alany, R. G.; Chuang, V.; Wen, J. Y., Studies of the Rate Constant of L-DOPA Oxidation and Decarboxylation by HPLC. *Chromatographia* **2012,** *75* (11-12), 597-606.

25. Young, T. E.; Griswold, J. R.; Hulbert, R. H., Melanin. I. Kinetics of the Oxidative Cyclization of Dopa to Dopachrome. *J.Org.Chem* **1974,** *39* (13), 1980-1982.

26. Hong, S.; Na, Y. S.; Choi, S.; Song, I. T.; Kim, W. Y.; Lee, H., Non-Covalent Self-Assembly and Covalent Polymerization Co-Contribute to Polydopamine Formation. *Advanced Functional Materials* **2012,** *22* (22), 4711-4717.

27. DG, G.; PW, J., The role of 2,4,5,-trihydroxyphenylalanine in melanin biosynthesis. *J.Biol.Chem.* **1977,** *252* (16), 5729-5734.

28. Capozzi, V.; Perna, G.; Carmone, P.; Gallone, A.; Lastella, M.; Mezzenga, E.; Quartucci, G.; Ambrico, M.; Augelli, V.; Biagi, P. F.; Ligonzo, T.; Minafra, A.; Schiavulli, L.; Pallara, M.; Cicero, R., Optical and photoelectronic properties of melanin. *Thin Solid Films* **2006,** *511*, 362-366.

29. Kohl, F. R.; Grieco, C.; Kohler, B., Ultrafast spectral hole burning reveals the distinct chromophores in eumelanin and their common photoresponse. *Chemical Science* **2020,** *11* (5), 1248-1259.

30. Sutter, J. U.; Birch, D. J. S., Metal ion influence on eumelanin fluorescence and structure. *Methods and Applications in Fluorescence* **2014,** *2* (2).

31. Ruot, B.; Plassais, A.; Olive, F.; Guillot, L.; Bonafous, L., TiO2-containing cement pastes and mortars: Measurements of the photocatalytic efficiency using a rhodamine B-based colourimetric test. *Solar Energy* **2009,** *83* (10), 1794-1801.

4. Conclusions

My PhD work has been focused on two main projects: Photoinduced precipitation and dissolution of calcium carbonate by means of photoacid and photobase generators and development of TiO_2 photocatalysts for water and air remediation.

For the first project, I investigated the mechanism behind the behaviour of photoacid and photobase generators in order to develop a system for local pH control. This feature can be very useful to induce the precipitation or the dissolution of materials by light. The processes in which my work focused are precipitation and dissolution of calcium carbonate. This kind of process can be very useful for frescoes restoration. Indeed, since their main component is calcium carbonate, a restoring method that involves the controlled precipitation and dissolution of the same material of which the artwork is made represents a great advantage, because the use of other materials like polymers or resins that can potentially damage the artwork is avoided. The photoinduced dissolution process of calcium carbonate was successfully obtained by using Diphenyiodonium hexafluorophosphate. The process was first developed in solution to study its mechanism and improve it. Then, it was adapted to the cleaning of a surface in order to be closer to the real application, obtaining a localized dissolution of calcium carbonate with an easy method and in mild conditions. The photoprecipitation process of calcium carbonate was studied by using two photoacid generators: Ketoprofen and Sodium tetraphenyl borate. These molecules correspond to two different photoprecipitation mechanism. Indeed, while the main mechanism inducing $CaCO_3$ precipitation using Sodium tetraphenyl borate is the pH jump, using Ketoprofen $CaCO_3$ precipitation is mainly induced by CO_2 generation rather than pH increase, thus leading to a more complex mechanism. However, in both cases is possible to obtain a controlled precipitation of $CaCO_3$ in a water-based solution. In both photodissolution and photoprecipitation processes it was possible to couple a sensitizer to the active molecules, which led to the use of light sources at 350-400 nm, thus in the Near-UV- Vis range. Furthermore, photoinduced precipitation of $CaCO_3$ by Ketoprofen was also studied for application in lithography and patterning. Indeed, with this system it is possible to literally write $CaCO_3$ structures with light. In particular, a gel system was implemented to locally precipitate calcium carbonate, contemporary fixing $CaCO_3$ crystals in a matrix. Irradiation was performed both with a laser and a LED focalized source and it was also possible to study localized crystal growth in the gel.

In the other part of my PhD my work focused on TiO_2 as photocatalytic semiconductor for environmental remediation. In particular, TiO_2 nanomaterials were developed both for water and

air remediation. Very small (5-7 nm) TiO_2 colloidal nanoparticles were synthesized by a surfactant-assisted method, using 4 different surfactants (Pluronic F-127, Triton X-100, CTAB and Sodium Cholate), for water cleaning. Very transparent and stable dispersions were obtained. Their photocatalytic activity was tested for degradation of organic pollutants using Rhodamine B as a model. All the systems are efficient photocatalysts with respect to commercial TiO_2 powder dispersions and are also resistant to different irradiation cycles. Rhodamine B degradation was also evaluated by monitoring its fluorescence decay during the time of irradiation, performed in a spectrofluorimeter. This method allows to follow the degradation process in real-time and to obtain information on the degradation mechanism. Modification with Graphene and MoS_2 were also performed for TiO_2 colloidal nanoparticles with an easy one pot exfoliation in which TiO_2 nanoparticles act in the graphite and MoS_2 exfoliation. These modifications lead to an increase or a decrease of the photocatalytic activity depending on the surfactant used for nanoparticles synthesis. TiO_2 colloidal nanoparticles obtained with Pluronic F-127 surfactant were also modified by polydopamine, by carrying on the L-Dopa oxidation and polymerization reaction in presence of TiO_2 nanoparticles. with this method it has been possible to obtain nanoparticles modified by polydopamine that can be dried and re-dissolved without losing their nanoparticles nature and that can be stable at different pH values. Therefore, it was also possible to evaluate differences in photocatalytic activity based on the pH of the medium. Finally, photocatalytic activity for inorganic pollutants degradation for air remediation was also investigated. A TiO_2/Graphene photocatalyst was embedded in cement matrix and its photocatalytic activity was studied. In particular, I focused on aging tests, evaluating photocatalytic behaviour with several cycles of irradiation and continuous refreshing of NOx gases, used as models of inorganic contaminants.

5. Technical features and theoretical background

Absorption spectroscopy

The acquisition of absorption spectra was carried out by a Perkin Elmer Lambda 650 spectrophotometer that has a wavelength range of 900-190 nm and a precision on the wavelength values of ± 1 nm.

The UV-Vis absorption spectrum derives from electronic transitions occurring when a molecule in the ground state absorbs a photon, going to an excited state. So, the absorption spectrum is characteristic of each molecule and that is why it is one of the first experiments carried on investigating a sample[1]. The extent of absorption, with the same instrumental factors, depends on cell size, absorption coefficient and concentration, provided by Lambert-Beer law. Beer's law is known as:

$$I_t = I_0 10^{-\varepsilon c l} \qquad \text{Eq.1}$$

Where:

- I_t: intensity of the transmitted light
- I_0: intensity of the incident light
- l: length of the optical path (cm)
- c: concentration
- ε molar extinction coefficient [M^{-1} cm^{-1}].

Since absorbance is defined as $A = -\log (I_t / I_0)$, Lambert-Beer Law can be also written as:

$$A = \varepsilon c l \qquad \text{Eq.2}$$

A spectrophotometer is composed by a polychromatic light source, followed by a monochromator that selects the excitation wavelength, a cell holder, and a detector. The spectrophotometer used in this work is a double beam instrument (Figure 1). Here, after the monochromator, the light beam is split and follows two paths, passing through the sample and the blank at the same time. This method is useful to minimize fluctuation of the light source and drift in the detection system.

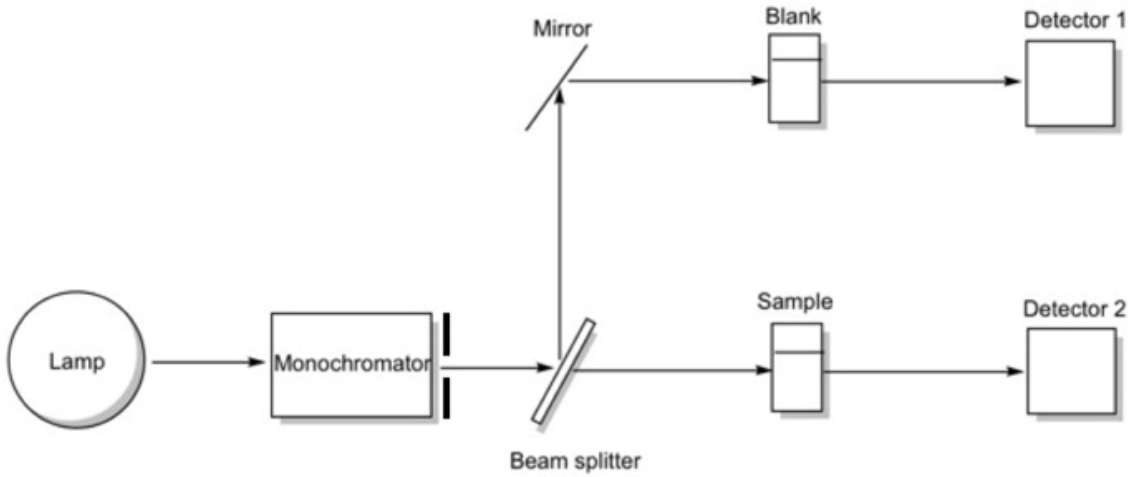

Figure 1: Block diagram of a double beam spectrophotometer

Fluorescence spectroscopy

Emission spectra were obtained with a Horiba Fluoromax-4 spectrofluorimeter.

Lots of information on the nature of the emitting excited state can be provided by luminescence. Indeed, luminescence spectroscopy is a very sensitive technique for the detection of chemical species in solution. Steady state luminescence measurements are carried on with a spectrofluorimeter.

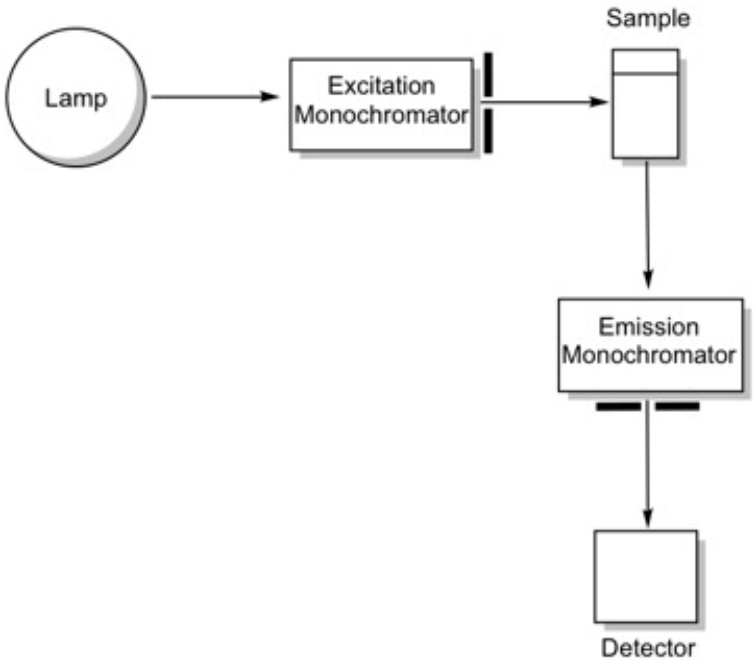

Figure 2: Block diagram of a spectrofluorimeter

The instrumentation is composed by a radiation source in the UV and visible spectrum (Xenon lamp), an emission and an excitation monochromator, a sample holder and a detection system composed by a reference photomultiplier to correct the emission spectrum of the lamp and a photomultiplier used to detect the emission signal of the sample.
When an emission spectrum is recorded, the sample is excited at a certain wavelength, typically corresponding to the maximum of the absorption peak of the fluorophore of interest. The excitation wavelength is selected by positioning the excitation monochromator, and, in the meanwhile, a scan (through wavelengths higher than the excitation one) is performed with the emission monochromator, generating the emission spectrum of the molecule. As it is showed in Figure 2, emission light is usually collected from the center of the cell with an angle of 90° with respect to the excitation beam, to minimize the contribution of transmitted excitation light[1].

Dynamic light scattering

Dynamic light scattering is a technique that permits to obtain information about the size of the objects present in solution exploiting the scattering of the light, according to the law of scattering of Rayleigh.
Rayleigh scattering is the elastic scattering of light or other electromagnetic radiation by particles much smaller than the wavelength of the light. This phenomenon can be measured, and its intensity gives information on microscopic parameters, as reported in the following equation:

$$I_{scatt} = I_0 \frac{V^2(1 + cos^2\theta)}{\lambda^4 R^2} Nf(n_1, n_2) \qquad \text{Eq.3}$$

Where I_0 is the intensity of the analysis beam, λ is incident laser wavelength, V is the volume of the scattering spherical object (related to the third power of the radius, and so to the third power of the diameter), R is observation distance (from the particle), θ is the scattering angle, N is the number of particles, and the last term takes into account the refractive indices of the particle(n_1) and the media(n_2). For the purposes of discussion it is sufficient to remember that the scattering intensity(I_{scatt}) is directly proportional to the sixth power of the diameter (from the above mentioned relation to the volume) and inversely proportional to the fourth power of the wavelength of the light analyzing and observation distance:

$$I_{scatt} \alpha \frac{d(h)^6}{\lambda^4 R^2} \qquad \text{Eq.4}$$

The scattering intensity fluctuates over time because it depends on two factors:

- Rayleight law, then the diameter of the particles at the same analysis conditions.
- Destructive / constructive scattering interference due to Brownian motion.

Small molecules in solutions are undergoing Brownian motion, so the distance R between the scatterers in the solution is constantly changing with time. This scattered light then undergoes either constructive or destructive interference by the surrounding particles, and within this intensity fluctuation, information is contained about the time scale of movement of the scatterers. The instrument thus uses an algorithm to determine the signal source despite fluctuations: the correlation function. The correlator, which builds the correlogram, measure the degree of similarity between two signals I, or one signal with itself, at varying time intervals t and t+τ . The digital correlator analyses the fluctuations in the scattered light. Signals correlation as a function of time gives the correlation function G(τ) (or correlogram):

$$G(\tau) = \int_0^\infty I(t) \cdot I(t+\tau) dt \qquad \text{Eq.5}$$

As the time delays become longer, the correlation decays exponentially and if the sample is monodispersed, the decay is simply a single exponential. G(τ) can be written as:

$$G(\tau) = e^{-Dq\tau} \qquad \text{Eq.6}$$

Where τ is the delay time, q is a parameter dependent from: λ (incident laser wavelength), the refractive index of the sample and θ (angle at which the detector is located). D is the translational diffusion coefficient and can be calculated by exploiting the Brownian motion in Einstein-Smoluchowski relation. The parameters of the analysis depend on the Einstein-Smoluchowski relation on diffusion:

$$D = k_B T / 6\pi\eta r \qquad \text{Eq.7}$$

used by the instrument in this form:

$$d(H) = k_B T / 3\pi\eta D \qquad \text{Eq.8}$$

where d(H) is the hydrodynamic diameter, T is the absolute temperature, k_B is Boltzmann's constant (linked to the Avogadro number N_A and to the gas constant R: $k_B = R / N_A$), η(eta) is the

dispersant viscosity, D is the diffusion coefficient. The factor 6 in the definition of D is conventional because it considers 3 dimensions (in one dimension it would be 2 instead of 6), but here we found a factor 3 because we consider a diameter analysis (radius (r)= 1/2 d(H)). As mentioned before, d(H) is the diameter of a sphere with the same diffusion coefficient as the particles, which is dependent from the charge of the particle, and the number of solvent molecules required to stabilize the particle. If the sample is monodispersed, the decay G(τ) is simply a single exponential. If, within the sample, there are two or more species of particles, the variations in intensity of the analysis scattering light will be of two different types; it will be obtained diffusion coefficients consistent to the particle diameter which generate different dynamic scattering. The difference in the correlogram between large and small particles is that for the former the correlation will persist for a long time (slow particles motion) and the signal will be changing slowly, for the latter the correlation will disappear more rapidly (fast particles motion) and the signal will be changing quickly. So, sample preparation either by filtration or centrifugation is critical to remove dust and artifacts from the solution.

Fluorescence microscopy

Measurements were performed by the fluorescence microscope Olympus IX71.
Fluorescence microscopy is an optical microscopy used to observe fluorescence of samples. Indeed, the specimen is excited with an excitation wavelength that causes the emission of the fluorophore/fluorophores present. Thus, fluorescence is exploited to produce a contrast in intensity with the background.

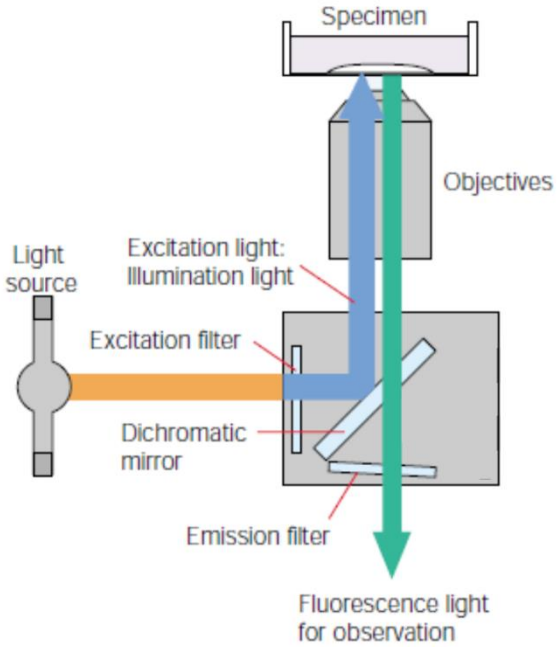

Figure 3: scheme of a fluorescence microscope

In this instrument, the light source is normally a Xenon lamp with excitation filters or a laser. Furthermore, emission filters are necessary to separate the emission light from the excitation light. This analysis brings many advantages, for instance it makes possible to observe objects in solution, analyze the motions and get the size and state of aggregation.

Sonochemistry

Most of the samples in the part of my PhD related to TiO_2 photocatalysis were treated with sonication, using a sonication bath ELMA transonic T460/H-35kHzin, order to have a homogeneous aqueous dispersion of the material in some cases and to exfoliate compounds in other cases.

Indeed, when a soundwave is emitted into a liquid, it creates micro-cavity bubbles due to the compression caused by the sinusoidal wave's oscillations[2]. Then, this bubbles collapse, generating a spot with very high temperature and pressure. This phenomenon could produce active radicals (chemical activation) or shear stresses and shock waves (physical or mechanical effects)[3].

To have the sonication effect of interest, it is important to control some relevant parameters[3]:

- Acoustic parameters (power density, power intensity etc.)
- Geometrical parameters (geometry and size of the reactor, liquid filling etc.)
- Standard operation parameters (temperature and pressure)
- Investigated system properties

In particular, it was demonstrated that high frequencies (> 100 kHz) are efficient for radical chemistry, while low frequencies (< 100 kHz) for mechanical and physical effects[4].

Transmission electron microscopy (TEM)

High resolution transmission electron microscopy (HR-TEM) was performed with a FEI Tecnai F20T HR-TEM instrument.

Transmission electron microscopy (TEM) is a technique where an electron beam (20-1000 KeV) goes through a thin layer of sample. The interaction with the sample affects the electron beam, generating an image that is focused on a fluorescent screen or a CCD. The resolution of TEM images reaches the Angstrom scale by the very low wavelength of the electron beam.

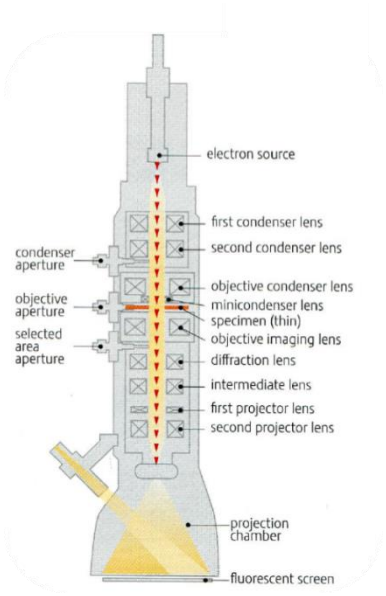

Figure 4: TEM instrument scheme

The typical TEM instruments is composed by an electron gun, a sample holder, a set of lens and magnifiers and a detector. The electron gun is based on a thermoionic emission of a tungsten wire of LaB6 that generates an electron beam, accelerated by an electric field. The electron gun has also condenser lens that align the electron beam on a small region of the sample. The electron beam hit the sample and is diffracted by the crystal reticulum of it, creating the images and the diffraction patterns. The image produced by the objective lens is then magnified from several lenses. Three imaging methods have been developed: Bright field, Dark field and High resolution.

Bright field imaging is based on the inelastic scattering phenomena that occur when the electron beam passes through the sample. The contrast is given by the weakening of the electron beam after passing trough the sample. Dark field is based on elastic scattering undergone by crystalline samples with the interaction of the electron beam. Beams diffracted from the sample generate the image. High resolution imaging is obtained by the interference of the diffracted beam with the direct beam obtained by the interaction with the sample. This can be obtained with a larger objective aperture and permits to observe lattice images[5].

Scanning electron microscopy (SEM)

Scanning electron microscopy (SEM) was performed with a tabletop Hitachi TM3000.
In SEM technique, an electron beam is focused on the sample surface (spot of almost 1 nm of diameter) and scanned over the sample in a rectangular raster. The image is created by the interaction between the electron beam and the sample and the signal gives information about the surface features of the specimen. Indeed, the voltage of the electron beam (50-30000 V) is lower than the one of the TEM because it is not necessary to penetrate the sample.

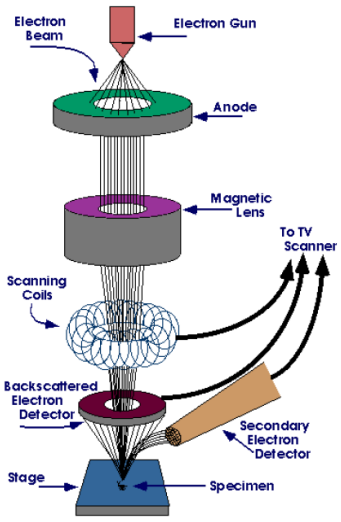

Figure 5: SEM general scheme

Imaging of the surface is given by secondary electrons and backscattered electrons. When one of the electrons of the electron beam collides with a conduction or valence band electron of the specimen, the latter is knocked out of its shell and is called “secondary electron”. In correspondence to a depression or hole of the samples, less secondary electrons can escape the surface and the image is darker, thus a topography of the surface can be obtained with secondary electrons. When the incident beam collides with the nucleus of an atom, the incident electron bounces back out of the sample and is called backscattered electrons. Heavier atoms are stronger

scatterer; thus, the image contrast is given by the atomic number. SEM (or TEM as well) can be coupled with Energy dispersive X-Ray spectroscopy (EDX). The emission of a secondary electron results in a vacancy which is filled with an electron of a higher shell. These processes emit X-rays, which are used to characterize the elemental composition of the sample[6].

Mass spectrometry (GC-MS)

Characterization of organic byproducts during my PhD was performed by GC-Mass spectrometry (Agilent technologies 6890N). Gas Chromatography (GC) coupled with Mass spectrometry (MS) is one of the most used techniques to characterize organic molecules. This technique is composed by a gas chromatograph (capillary column) in which the molecules of the analyzed mixture, that must be volatile above 350°C, are separated and the mass spectrometer.

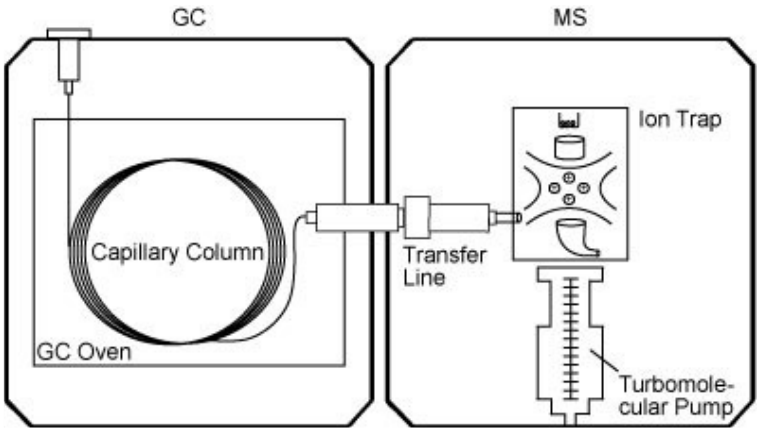

Figure 6: GC- MS scheme

When the mass is coupled with the GC an electron impact (EI) technique is used to detect the mass of the species. Here, a high energy (almost 70 eV) electron beam hits the molecule of interest "M" and leads to the removal of an outer electron, forming the ion radical M^+. The energy level of M^+ is sufficiently high to generate a series of fragmentations via unimolecular dissociation processes. The fragments that are usually neutral and ion radical species, are subjected to electric potential variations that push the charged species into the mass analyzer. Here, they are separated by electromagnetic forces, depending on their mass-charge ratio (m/z), and the mass spectrum is thus obtained. The molecular mass of the molecule M is thus obtained by the fragments observed in the spectrum[7].

5.1. Bibliography

1. Balzani, V.; Ceroni, P.; Juris, A., Photochemistry and Photophysics: concepts, research, applications. Wiley, **2014**.
2. Suslick, K. S.; Flannigan, D. J., Inside a collapsing bubble: sonoluminescence and the conditions during cavitation. *Anni. Rev. Rhys. Chem.* **2008,** *9* (59), 659-683.
3. Delmas, H.; Le, N. T.; Barthe, L.; Julcour-Lebigue, C., Optimization of hydrostatic pressure at varied sonication conditions - power density, intensity, very low frequency - for isothermal ultrasonic sludge treatment. *Ultrasonics Sonochemistry* **2015,** *25*, 51-59.
4. Mason, T. J.; Cobley, A. J.; Graves, J. E.; Morgan, D., New evidence for the inverse dependence of mechanical and chemical effects on the frequency of ultrasound. *Ultrasonics Sonochemistry* **2011,** *18* (1), 226-230.
5. Williams, D. B.; Carter, C. B., Transmission electron microscopy. Springer **2009**.
6. Zhou, W.; Wang, Z. L., Scanning microscopy for nanotechnology.Springer **2007**.
7. Hoffmann, E.; Stroobant, V., Mass spectrometry: principles and applications. Wiley **2007**.

Acknowledgements

I thank Professor Marco Montalti, the supervisor of my Ph.D. project and all the members of Photochemistry Laboratory of the Chemistry department “G. Ciamician” of the University of Bologna.

I thank Professor Helmut Cölfen and all the members of his research group of the Chemistry Department of University of Konstanz (Germany).

I thank Professor Juan Manuel García-Ruiz and the members of Laboratorio de Estudios Cristatlograficos (LEC) in Granada (Spain).

I thank Dr. Marco Goisis from Italcementi (Heidelberg cement group).

I thank all the members of the ERC Project “Lacrys” and of “Graphene Flagship” European project.